METHODS FOR PROBING NEW PHYSICS AT HIGH ENERGIES

by

PETER B. DENTON

Dissertation

Submitted to the Faculty of the

Graduate School of Vanderbilt University

in partial fulfillment of the requirements

for the degree of

DOCTOR OF PHILOSOPHY

in

Physics

August, 2016

Nashville, Tennessee

Approved:

Thomas J. Weiler, Ph.D.

Robert J. Scherrer, Ph.D.

Thomas W. Kephart, Ph.D.

Andreas A. Berlind, Ph.D.

M. Shane Hutson, Ph.D.

Preface

This dissertation covers two broad topics. The title, "*Methods for Probing New Physics at High Energies*," hopefully encompasses both of them. The first topic is located in part I of this work and is about integral dispersion relations. This is a technique to probe for new physics at energy scales near to the machine energy of a collider. For example, a hadron collider taking data at a given energy is typically only sensitive to new physics occurring at energy scales about a factor of five to ten beneath the actual machine energy due to parton distribution functions. This technique is sensitive to physics happening directly beneath the machine energy in addition to the even more interesting case: directly *above*. Precisely where this technique is sensitive is one of the main topics of this area of research.

The other topic is located in part II and is about cosmic ray anisotropy at the highest energies. The unanswered questions about cosmic rays at the highest energies are numerous and interconnected in complicated ways. What may be the first piece of the puzzle to fall into place is determining their sources. This work looks to determine if and when the use of spherical harmonics becomes sensitive enough to determine these sources.

The completed papers for this work can be found online. For part I on integral dispersion relations see reference [1] published in Physical Review D. For part II on cosmic ray anisotropy, there are conference proceedings [2] published in the Journal of Physics: Conference Series. The analysis of the location of an experiment on anisotropy reconstruction is [3], and the comparison of different experiments' abilities to reconstruct anisotropies is [4] published in The Astrophysical Journal and the Journal of High Energy Astrophysics respectively.

While this dissertation is focused on three papers completed with Tom Weiler at Vanderbilt University, other papers were completed at the same time. The first was with Nicusor Arsene, Lauretiu Caramete, and Octavian Micu in Romania on the detectability of quantum black holes in extensive air showers [5]. The next was with Luis Anchordoqui, Haim Goldberg, Thomas Paul, Luiz da Silva, Brian Vlcek, and Tom Weiler on placing limits on Weinberg's Higgs portal, originally written to explain anomalous N_{eff} values, from direct detection and collider experiments [6] which was published in Physical Review D. The final was completed at Fermilab with Stephen Parke and Hisakazu Minakata on a perturbative description of neutrino oscillations in matter [7] which was published in the Journal of High Energy Physics, and the code behind this paper is publicly available [8].

Table of Contents

List of Tables

List of Figures

Part I

Integral Dispersion Relations

Chapter 1

Introduction and Motivation

1.1 Introduction

This part of the thesis is focused on integral dispersion relations (IDRs). IDRs were widely used to study the nonperturbative aspects of the strong interaction, but are still a useful tool to relate core principles such as unitarity and analyticity to physical observables. An article containing this work can be found at reference [1]. In the remainder of this chapter we will outline the path of this part and motivate using IDRs to probe new physics. In chapter 2 we derive the IDRs from analyticity arguments and the optical theorem. A brief history of IDRs is also included. Chapter 3 contains a discussion of analytic solutions in simplifying cases as well as some numerical results for comparison to the nonsimplified, full equations. We also discuss several of the commonly proposed solutions to this evidence. In chapter 4 we will present the current status of $pp, p\bar{p}$ total cross section measurements. We also will discuss the experiments and how they measure the parameter ρ without the use of IDRs. In chapter 5 we turn some of these new physics models into modifications of the total pp cross section. In chapter 6 we compile all the results from the various models. Finally, in chapter 7 the conclusions are discussed.

1.2 Motivation

There is a host of evidence that the standard model (SM) of particle physics is not the entire picture. To this end many experiments have been looking for new physics at various energy scales.

IDRs make use of analyticity to probe energies above (and below) the machine energy at a collider experiment such as the Large Hadron Collider (LHC). Since IDRs relate the scattering amplitude at one energy to that at *every* energy up to infinity, they are sensitive to the gross features of the scattering amplitude at all energies, although they are the most sensitive to changes near the machine energy. Previously strong neutrino interactions at high energy have been discussed in the context of cosmic rays beyond the GZK limit (see part II for more on the GZK limit) [13]. This part will focus on hadronic processes only, specifically pp and $p\bar{p}$ interactions and generalized deviations from SM physics. This work describes several possible deviations (chapter 5) from the canonical cross section (§2.4.1) and how big of an effect they might have.

Chapter 2

Review of Integral Dispersion Relations

2.1 Historical

The history of the development of IDRs stretches back nearly 75 years. The initial steps towards their derivation started even earlier. In 1926 Kronig [14] and in 1927 Kramers [15] each derived what is known as the Kramers-Kronig relations in the context of measuring the index of refraction. For a given complex valued function $\chi(\omega) = \chi_1(\omega) + i\chi_2(\omega)$ where $\chi_{1,2} \in \mathbb{R}$, they showed,

$$\begin{aligned} \chi_1(\omega) &= \frac{1}{\pi}\mathcal{P}\int_{-\infty}^{\infty} \frac{\chi_2(\omega')}{\omega' - \omega} d\omega' \,, \\ \chi_2(\omega) &= -\frac{1}{\pi}\mathcal{P}\int_{-\infty}^{\infty} \frac{\chi_1(\omega')}{\omega' - \omega} d\omega' \,, \end{aligned} \tag{2.1}$$

where $\mathcal{P}\int$ is the principal value. These relations are known to mathematicians as Hilbert Transforms. They contain some of the key mathematical ideas that IDRs exploit. That is, they relate the real part of χ to an integral over the imaginary part of χ, which is physically related to the total cross section by the optical theorem.

The first example of IDRs used with rigor comparable to that used today was in 1954 by M. Gell-Mann, M. L. Goldberg, and W. E. Thirring [16] who helped put IDRs on a sound footing. It was more difficult at the time because the Pomeranchuk theorem lacked the sound experimental evidence it has since gained at the Tevatron and the LHC (see §2.4.2). The first use of IDRs with pp scattering was in 1964 by P. Söding [17]. Finally, the main reference used in this chapter is from 1985 by M. M. Block and R. N. Cahn [18], which covers a broad collection of high energy hadronic scattering topics.

2.2 Mathematics

IDRs are an extension of Cauchy's integral formula which states that

$$f(a) = \frac{1}{2\pi i}\oint_{\partial A} \frac{f(z)}{z - a} dz \,, \tag{2.2}$$

where A is a region in $\mathbb{C}$, complex space, and ∂A is its boundary and $a \in A$. We also require that f is analytic everywhere in A. Analyticity of a function can be understood simply as being locally "sufficiently smooth." More precisely, a function $f(z)$ is analytic in region A if f is complex differentiable everywhere in A. $f(z)$ is complex differentiable on a region if its first derivative calculated in the usual fashion is continuous and it satisfies the Cauchy-Riemann equations. We write $f(z) = u(x, y) + iv(x, y)$ and $z = x + iy$ with $u, v, x, y \in \mathbb{R}$. Then the Cauchy-Riemann equations are,

$$\begin{aligned} \frac{\partial u}{\partial x} &= \frac{\partial v}{\partial y} \,, \\ \frac{\partial u}{\partial y} &= -\frac{\partial v}{\partial x} \,. \end{aligned} \tag{2.3}$$

2.3 Scattering Kinematics

The scattering discussion will be presented in two reference frames. The first is the center of mass (momentum) (COM) that is commonly used today. The second is the so called "lab-frame" in which one of the particles is considered to be at rest with the necessary boost applied to the other particle. Here we will be considering the high energy collisions of particles with equal mass such as pp or $p\bar{p}$ collisions probed by the Tevatron [19], the Large Hadron Collider (LHC) [20], and extensive air showers (EAS) measured at experiments like Fly's Eye (the precursor to the modern Telescope Array) [21], the Akeno Giant Air Shower Array [22], and the Pierre Auger Observatory [23] through the Glauber model [24].

This lab frame approach follows that of Martin M. Block among others and its gained simplicity can be seen in the symmetry of fig. 2.1 [18]. For an example of what IDRs look like using the center of mass frame see [25].

Throughout this part we will use the so called "natural units" where $\hbar = c = 1$.

2.3.1 Mandelstam Variables

This discussion of scattering and the derivation of IDRs in section 2.4 generally follow from [18]. First, in the COM frame we consider the general $2 \to 2$ scattering process, where two initial protons approaching each other at high energy with 4-momenta p_1, p_2, elastically scattering $(p+p \to p+p)$ to final states with momenta p_3, p_4. Then the CM energy squared is

$$s = (p_1 + p_2)^2 = (p_3 + p_4)^2 = 4(k^2 + m^2)\,, \tag{2.4}$$

where k is the COM momentum, m is the proton mass, and s is the typical Mandelstam variable [26][1].

We can similarly define the transfer energy squared as the next Mandelstam variable t

$$t = (p_1 - p_3)^2 = (p_2 - p_4)^2 = -4k^2 \sin^2\left(\frac{\theta}{2}\right)\,, \tag{2.5}$$

where θ is the scattering angle in the COM frame. The final Mandelstam variable is the square of the transfer energy plus a switch,

$$u = (p_1 - p_4)^2 = (p_2 - p_3)^2 = -4k^2 \cos^2\left(\frac{\theta}{2}\right)\,, \tag{2.6}$$

which gives rise to the useful relation

$$s + t + u = 4m^2\,. \tag{2.7}$$

We note that while $s \geq 0$, both $t, u \leq 0$.

In the lab frame,

$$s = 2(m^2 + mE)\,, \tag{2.8}$$

where the momentum of the moving particle p and the energy E are related by the usual relation $E = \sqrt{p^2 + m^2}$. For forward elastic scattering, $t = 0$, so combining eqs. 2.7 and 2.8 allows us to write

$$E = \frac{s - u}{4m^2}\,, \tag{2.9}$$

which has the nice property that interchanging $pp \leftrightarrow p\bar{p}$ corresponds to the sign change $E \leftrightarrow -E$ since the first interchange is the same as interchanging $p_2 \leftrightarrow -p_4$. This fact is the justification for working in the lab frame.

---

[1] Interestingly, these commonly used variables were initially introduced in the context of IDRs.

2.3.2 Cross Sections

Next we look to relate scattering amplitudes to differential cross sections. Back in the COM frame we have

$$\frac{d\sigma}{d\Omega_{\text{COM}}} = |f_{\text{COM}}|^2 \,, \tag{2.10}$$

or

$$\frac{d\sigma}{dt} = \frac{\pi}{k^2}|f_{\text{COM}}|^2 \,. \tag{2.11}$$

In the lab frame these formulas look very similar.

$$\frac{d\sigma}{d\Omega_{\text{lab}}} = |f|^2 \,, \tag{2.12}$$

or

$$\frac{d\sigma}{dt} = \frac{\pi}{p^2}|f|^2 \,, \tag{2.13}$$

where for simplicity we define the lab frame scattering amplitude just f.

Next we write down the crucial optical theorem in both reference frames.

$$\sigma_{\text{tot}} = \frac{4\pi}{k}\Im f_{\text{COM}}(\theta = 0) \,, \tag{2.14}$$

and

$$\sigma_{\text{tot}} = \frac{4\pi}{p}\Im f(\theta_L = 0) \,, \tag{2.15}$$

where θ_L is the lab frame scattering angle. Note that $\theta = 0 \Rightarrow \theta_L = 0$. For several derivations of the optical theorem, see [27].

2.4 Derivation of IDRs

We write the scattering amplitude f as the limit of an analytic complex valued function $\mathscr{F}$ at $t = 0$ by

$$f_{pp,p\bar{p}}(E) = \lim_{\epsilon \to 0^+} \mathscr{F}(\pm E \pm i\epsilon) \,, \tag{2.16}$$

using the interchange property of E mentioned after eq. 2.9. That is, the argument of $\mathscr{F}$ is a complex variable.

From the optical theorem, $\Im f$ is related to the cross section which describes physical processes, so $\Im\mathscr{F} = 0$ on, and near, the real axis when there is no physical process at the given energy, and is analytic there. Everywhere else along the real axis, pp or $p\bar{p}$ can interact and $\Im\mathscr{F}$ flips sign from above to below the real axis. This leads to a branch cut[2] for $|\Re E| > m_p$ as shown by the dashed lines in fig. 2.1.

Since only the imaginary part of $\mathscr{F}$ is discontinuous in the imaginary direction and it changes sign across the branch cuts while the real part remains the same, we can write

$$\begin{aligned} \Im\mathscr{F}(E' + i\epsilon) &= -\Im\mathscr{F}(E' - i\epsilon) \,, \\ \Re\mathscr{F}(E' + i\epsilon) &= \Re\mathscr{F}(E' - i\epsilon) \,, \end{aligned} \tag{2.17}$$

---

[2] There are additional singularities at lower energies where the protons can interact via pion states, but the contribution to the IDR from these low energy considerations is negligible, as will be shown in chapter 3.

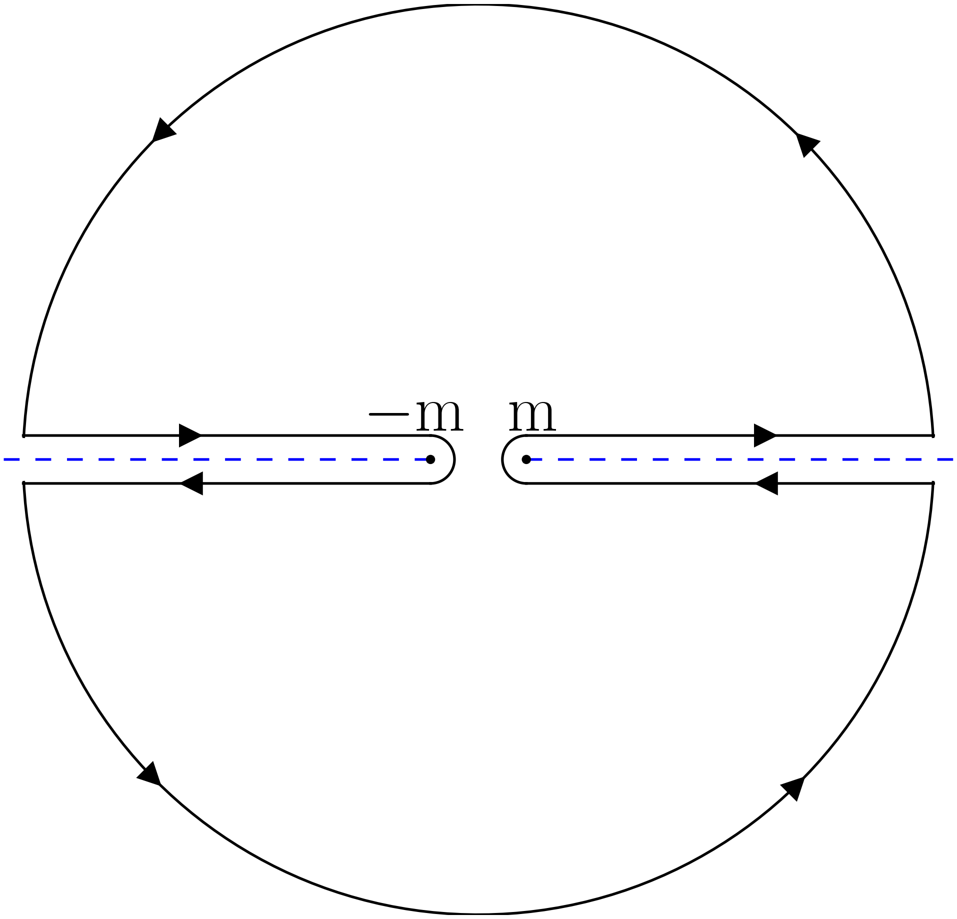

Figure 2.1: In the complex E plane there are two branch cuts as shown by the blue dashed lines from $\pm m$ to $\pm\infty$ respectively. The contour shown is that over which the line integral is taken.

$$\begin{aligned}\mathscr{F}(E'+i\epsilon)-\mathscr{F}(E'-i\epsilon)&=2i\Im\mathscr{F}(E'+i\epsilon)\,,\\ \mathscr{F}(E'+i\epsilon)-\mathscr{F}(E'-i\epsilon)&=-2i\Im\mathscr{F}(E'-i\epsilon)\,.\end{aligned}\tag{2.18}$$

We then integrate around a loop where $\mathscr{F}$ is analytic. A sketch of this contour is shown in fig. 2.1 where the outer curves are taken to the limit $|E|\to\infty$. For the moment we will assume that the contribution to the integral from the outer curves is zero. From eq. 2.2 we have that

$$\mathscr{F}(E)=\frac{1}{2\pi i}\left[\int_{m_p}^{\infty}dE'\frac{\mathscr{F}(E'+i\epsilon)-\mathscr{F}(E'-i\epsilon)}{E'-E}+\int_{-\infty}^{-m_p}dE'\frac{\mathscr{F}(E'+i\epsilon)-\mathscr{F}(E'-i\epsilon)}{E'-E}\right]\,,\tag{2.19}$$

where the four contributions come from the four straight sections along each side of the two cuts and the small inner curves are negligibly small as $\epsilon\to0$.

Using eq. 2.18, eq. 2.19 becomes

$$\mathscr{F}(E)=\frac{1}{\pi}\left[\int_{m_p}^{\infty}dE'\frac{\Im\mathscr{F}(E'+i\epsilon)}{E'-E}+\int_{m_p}^{\infty}dE'\frac{\Im\mathscr{F}(-E'-i\epsilon)}{E'+E}\right]\,.\tag{2.20}$$

We consider that $\mathscr{F}$ may be even or odd in its argument, denoted $\mathscr{F}_+$ or $\mathscr{F}_-$ respectively. Then,

$$\mathscr{F}_\pm(E)=\frac{1}{\pi}\int_{m_p}^{\infty}dE'\Im\mathscr{F}_\pm(E'+i\epsilon)\left(\frac{1}{E'-E}\pm\frac{1}{E'+E}\right)\,.\tag{2.21}$$

or

$$\begin{aligned}\mathscr{F}_+(E)&=\frac{1}{\pi}\int_{m_p}^{\infty}dE'\Im\mathscr{F}_+(E'+i\epsilon)\frac{2E'}{E'^2-E^2}\,,\\ \mathscr{F}_-(E)&=\frac{1}{\pi}\int_{m_p}^{\infty}dE'\Im\mathscr{F}_-(E'+i\epsilon)\frac{2E}{E'^2-E^2}\,.\end{aligned}\tag{2.22}$$

We write the $pp,p\bar{p}$ scattering amplitudes in terms of their even and odd (under $E\leftrightarrow -E$ interchange) components,

$$f_{p\bar{p},pp}=f_+\pm f_-\,,\quad\text{where}\quad f_\pm=\frac{1}{2}(f_{p\bar{p}}\pm f_{pp})\,.\tag{2.23}$$

We define the principal value integral in the traditional sense,

$$\mathcal{P}\int_a^c f(x)dx=\lim_{\epsilon\to0^+}\left[\int_a^{b-\epsilon}f(x)dx+\int_{b+\epsilon}^{c}f(x)dx\right]\,,\tag{2.24}$$

for $a<b<c$ under the conditions that

$$\begin{aligned}\int_a^b f(x)dx&=\pm\infty\qquad\forall a<b\text{ and}\\ \int_b^c f(x)dx&=\mp\infty\qquad\forall c>b\,,\end{aligned}\tag{2.25}$$

as is the case, for example, for a simple pole, $f(x)=g(x)/(x-b)$ for $g(x)$ continuous. More generally we have that

$$\lim_{\epsilon\to0^+}\int_a^c\frac{g(x)}{x-b\pm i\epsilon}dx=\mathcal{P}\int_a^c\frac{g(x)}{x-b}dx\mp i\pi g(b)\,,\tag{2.26}$$

the Sokhotski-Plemelj theorem, which makes use of Cauchy's integral formula, eq. 2.2, for the final term. We use the version with the lower signs and substitute $x = E' + i\epsilon$ on the LHS to get

$$\lim_{\epsilon\to 0^+} \int_a^c \frac{g(E'+i\epsilon)}{E'-b} dE' = \mathcal{P}\int_a^c \frac{g(x)}{x-b} dx + i\pi g(b)\,. \tag{2.27}$$

The LHS is eq. 2.22 after the substitution $g \to 2E'\Im\mathscr{F}_+/(E'+E)$, $2E\Im\mathscr{F}_-/(E'+E)$ and $a \to m_p, b \to E, c \to \infty$. Then,

$$\begin{aligned} \mathscr{F}_+(E) &= \frac{1}{\pi}\mathcal{P}\int_{m_p}^{\infty} dE'\Im\mathscr{F}_+(E')\frac{2E'}{E'^2-E^2} + i\Im\mathscr{F}_+(E)\,,\\ \mathscr{F}_-(E) &= \frac{1}{\pi}\mathcal{P}\int_{m_p}^{\infty} dE'\Im\mathscr{F}_-(E')\frac{2E}{E'^2-E^2} + i\Im\mathscr{F}_-(E)\,, \end{aligned} \tag{2.28}$$

$$\begin{aligned} \Re\mathscr{F}_+(E) &= \frac{1}{\pi}\mathcal{P}\int_{m_p}^{\infty} dE'\Im\mathscr{F}_+(E')\frac{2E'}{E'^2-E^2}\,,\\ \Re\mathscr{F}_-(E) &= \frac{1}{\pi}\mathcal{P}\int_{m_p}^{\infty} dE'\Im\mathscr{F}_-(E')\frac{2E}{E'^2-E^2}\,, \end{aligned} \tag{2.29}$$

which is the simplest version of the IDRs. We pause to note, at this point, the similarity of eqs. 2.1 and 2.29.

We now use some forward thinking and admit that we know the shape of $\Im\mathscr{F}$ as $E' \to \infty$. By the optical theorem (eq. 2.15), $\Im f_+ \propto p\sigma_{\text{tot}}$, and as $E' \to \infty$, the integrand of the even integral scales like σ_{tot} which, from the Froissart bound (§2.4.1) and experiments (§4.2), scales like $\sigma_{\text{tot}} \propto \log^2 E'$. This integral does not converge at infinity, so we must perform a subtraction to gain convergence. In the odd integral we consider a new function $\mathscr{G}_-(E) = \mathscr{F}_+(E)/E$. The odd function from eq. 2.29 is,

$$\Re\mathscr{F}_+(E) = \Re\mathscr{F}_+(0) + \frac{1}{\pi}\mathcal{P}\int_{m_p}^{\infty} dE'\Im\mathscr{F}_+(E')\frac{2E^2}{E'(E'^2-E^2)}\,. \tag{2.30}$$

This new form has several important features. The first is that the integrand is $\log^2 E'/E'^2$ as $E' \to \infty$ which goes to zero faster than $1/E'$ so the integral converges. The next is that there is an additional $\mathscr{F}_+(E=0)$ term which comes from the pole at $E = 0$.

On the other hand, $\Im f_- \propto p\Delta\sigma_{\text{tot}}$, where $\Delta\sigma_{\text{tot}}$ is the difference between the pp and $p\bar{p}$ scattering amplitudes. The Pomeranchuk theorem (§2.4.2) says that $\Delta\sigma_{\text{tot}} \to 0$ as $E' \to \infty$ so the resulting integrand goes to zero faster than $1/E'$ and needs no additional subtraction term.

We now take the $\epsilon \to 0$ limit and recover the physical amplitude f from the analytic extension $\mathscr{F}$ we have been using. The odd dispersion relation from eq. 2.29 and the singly subtracted IDR, eq. 2.30 are,

$$\begin{aligned} \Re f_-(E) &= \frac{1}{\pi}\mathcal{P}\int_{m_p}^{\infty} dE'\Im f_-(E')\frac{2E}{E'^2-E^2}\,,\\ \Re f_+(E) &= \Re f_+(0) + \frac{1}{\pi}\mathcal{P}\int_{m_p}^{\infty} dE'\Im f_+(E')\frac{2E^2}{E'(E'^2-E^2)}\,. \end{aligned} \tag{2.31}$$

We can now combine eqs. 2.15, 2.23, 2.31, and the fact that $f_{pp}(0) = f_{p\bar{p}}(0)$ as described at eq. 2.9

to write the useful singly subtracted IDRs:

$$
\begin{aligned}
\Re f_{pp}(E) &= \Re f_{pp}(0) + \frac{E}{4\pi^2}\mathcal{P}\int_{m_p}^{\infty} dE'\,\frac{p'}{E'}\left[\frac{\sigma_{pp}(E')}{E'-E} - \frac{\sigma_{p\bar{p}}(E')}{E'+E}\right] , \\
\Re f_{p\bar{p}}(E) &= \Re f_{p\bar{p}}(0) + \frac{E}{4\pi^2}\mathcal{P}\int_{m_p}^{\infty} dE'\,\frac{p'}{E'}\left[\frac{\sigma_{p\bar{p}}(E')}{E'-E} - \frac{\sigma_{pp}(E')}{E'+E}\right] .
\end{aligned}
\tag{2.32}
$$

Before continuing, a few features of these integral dispersion relations should be noted. The first is that the scattering amplitude at one energy E (typically referred to as the "machine" energy throughout this part) is dependent on the behavior of the scattering amplitude and thus the cross section at *all* energies. It is this fact that we make particular use of in this part. The next is the pole. Both integrals have a pole at $E' = E$. So it is at $E' = E$ where the value of σ_{tot} contributes the most to the integral. Moreover, this pole only occurs for the same process as on the LHS (pp or $p\bar{p}$). We also note that the total cross section for the other process is always scaled down since $E' + E > E' - E$. Finally there is the addition of a new subtraction term, $\Re f(0)$ which can only be determined experimentally.

We also note the existence of doubly subtracted IDRs where the replacement $\mathscr{G}_- = \mathscr{F}_-/E^2$ is also made. These may be necessary in certain cases for convergence, but do not seem to be required by experimental data. That is, if the Pomeranchuk theorem isn't valid ($\Delta\sigma \not\to 0$ as $E \to \infty$) or if the total cross section grows like E^α for $\alpha \geq 1$ or faster, an additional subtraction (or more) may be necessary to guarantee convergence.

We define the ratio,

$$
\rho_{pp,p\bar{p}}(E) = \frac{\Re f_{pp,p\bar{p}}(E, t=0)}{\Im f_{pp,p\bar{p}}(E, t=0)} , \tag{2.33}
$$

which allows us to rewrite eq. 2.32 as,

$$
\begin{aligned}
\rho_{pp}(E)\sigma_{pp}(E) &= \frac{4\pi}{p}\Re f_{pp}(0) + \frac{E}{p\pi}\mathcal{P}\int_{m_p}^{\infty} dE'\,\frac{p'}{E'}\left[\frac{\sigma_{pp}(E')}{E'-E} - \frac{\sigma_{p\bar{p}}(E')}{E'+E}\right] , \\
\rho_{p\bar{p}}(E)\sigma_{p\bar{p}}(E) &= \frac{4\pi}{p}\Re f_{p\bar{p}}(0) + \frac{E}{p\pi}\mathcal{P}\int_{m_p}^{\infty} dE'\,\frac{p'}{E'}\left[\frac{\sigma_{p\bar{p}}(E')}{E'-E} - \frac{\sigma_{pp}(E')}{E'+E}\right] .
\end{aligned}
\tag{2.34}
$$

This equation presents the IDRs in the form to be used throughout the remainder of this part.

2.4.1 Froissart Bound

The Froissart bound states that the total hadronic cross section is $\sigma \leq C\log^2(E/E_0)$ for some coefficients C, E_0 as $E \to \infty$ [28]. Various proofs of this exist in the literature, and the nature of the constants C, E_0 have been and still are vigorously debated. Values of C are typically about two orders of magnitude above those from present experimental reaches [29–31]. This point is important in that it puts no limits on increasing the cross section so long as it asymptotically ($E \to \infty$) grows no faster than $\log^2 E$.

2.4.2 Pomeranchuk Theorem

The Pomeranchuk theorem states that at high energies $\Delta\sigma \equiv \sigma_{pp} - \sigma_{p\bar{p}} \to 0$ [32]. Moreover, the difference grows no more quickly than $\log s$ [33, 34]. This fact has been well established by collider experiments, where $\Delta\sigma \propto\!\!\!\sim s^{-0.5}$ [35].

With an understanding of the underlying theory of quantum chromodynamics (QCD), the Pomeranchuk theorem can be more simply understood as a statement that at sufficiently high energies baryons are composed of sea quarks and gluons while the valence quarks barely contribute to their composition. As such, $p+p$ scattering looks identical to $p+\bar{p}$ scattering for sufficiently high energies.

Chapter 3

A Simplified Integral Dispersion Relation to Set Expectations

In this chapter we make three assumptions to reduce the IDRs in eq. 2.34 to a form that can be integrated analytically to get a feel for the reach and nature of the IDRs. While none of the assumptions are strictly valid, they are useful to reveal the gross features of the dispersion integral. The first assumption is to set m_p to zero. Besides replacing the lower limit of integration with zero, this assumption also sets p'/E' equal to one. The second assumption is to set σ_{pp} and $\sigma_{p\bar{p}}$ equal to each other, and to a constant which we call σ_0. The final assumption is to set $f(0) = 0$, a fact that is moderately supported by the data (§4.2). With these assumptions, both dispersion integrals become

$$\rho\sigma_0 = \frac{2\sigma_0}{\pi}\mathcal{P}\int_0^\infty \frac{dx}{x^2-1}\,, \tag{3.1}$$

which can then be integrated to

$$\rho = \frac{2}{\pi}\log\left[\frac{|1-x|}{1+x}\right]_0^\infty\,, \tag{3.2}$$

where $x \equiv E'/E$ and we note that the integral is singular at $x = 1$. Blind evaluation of the definite integral over the range $[0,\infty]$ then gives zero. That this is correct can also be seen in the following way: by definition of a principal value integral, the definite integral from eq. 3.1 is

$$\lim_{\epsilon\to 0}\left[\int_0^{1-\epsilon}\frac{dx}{x^2-1} + \int_{1+\epsilon}^{\infty}\frac{dx}{x^2-1}\right]\,. \tag{3.3}$$

Replacing x by $u \equiv \frac{1}{x}$ in either integral, maps the integration region into that of the other integral (for ϵ small), and reveals that the two integrals are equal but with opposite sign. Thus the total integral vanishes. In particular, the singularity in the integrand vanishes in the principal value.

In fig. 3.1, we plot the integrand $(x^2-1)^{-1}$ of our simplified dispersion integral. As the lower limit of integration x_{min} is moved up from zero, the cancellation above and below the singularity is no longer complete. However, the vanishing of the total integral when integrated from from zero to infinity allows us replace the integration across the singularity with a simple, manifestly nonsingular integral as follows:

$$\mathcal{I}(x_{\mathrm{min}}) \equiv \int_{x_{\mathrm{min}}}^{\infty}\frac{dx}{x^2-1} = \int_0^{x_{\mathrm{min}}}\frac{dx}{1-x^2}\,. \tag{3.4}$$

For $x_{\mathrm{min}} = 1$, the cancellation is maximally incomplete and the integral is infinite. We plot $\mathcal{I}(x_{\mathrm{min}})$ in fig. 3.2. As expected, the integral is everywhere positive, and diverges at $x_{\mathrm{min}} = 1$. The divergence seems unphysical in that it corresponds to either $\Im f = 0 \Rightarrow \sigma_{\mathrm{tot}} = 0$ by the optical theorem which shouldn't be the case or that $\Re f \to \infty \Rightarrow \sigma_{\mathrm{tot}} \to \infty$ which is also unphysical. In reality, a step function increase in the integrand is unphysical as the phase space alone requires a continuous rise in the cross section which then keeps the integral finite.

We may ask how the singularity is approached, from the two cases: above or below. Writing $x_{\mathrm{min}} = 1-\Delta$ and $1+\Delta$, we have the two integrals $\int_{1-\Delta}^{\infty}\frac{dx}{x^2-1}$ and $\int_{1+\Delta}^{\infty}\frac{dx}{x^2-1}$. We restrict ourselves to $0 < \Delta < 1$. The first integral crosses the singularity and according to eq. 3.4 is equal to the clearly finite integral $\int_0^{1-\Delta}\frac{dx}{1-x^2}$. With the replacement $x \to 1/x$, the second integral becomes $\int_0^{\frac{1}{1+\Delta}}\frac{dx}{1-x^2}$. Thus, the two integrations differ only in the upper limit of integration. At first order

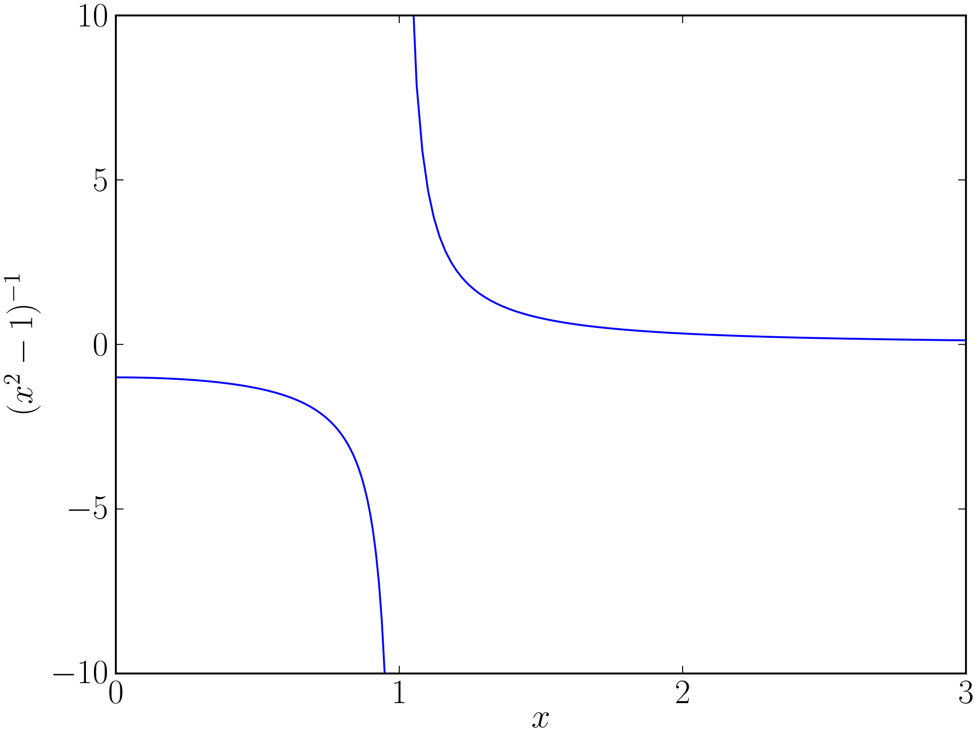

Figure 3.1: The integrand of the IDRs with the σ = constant and $m_p \to 0$ limits taken.

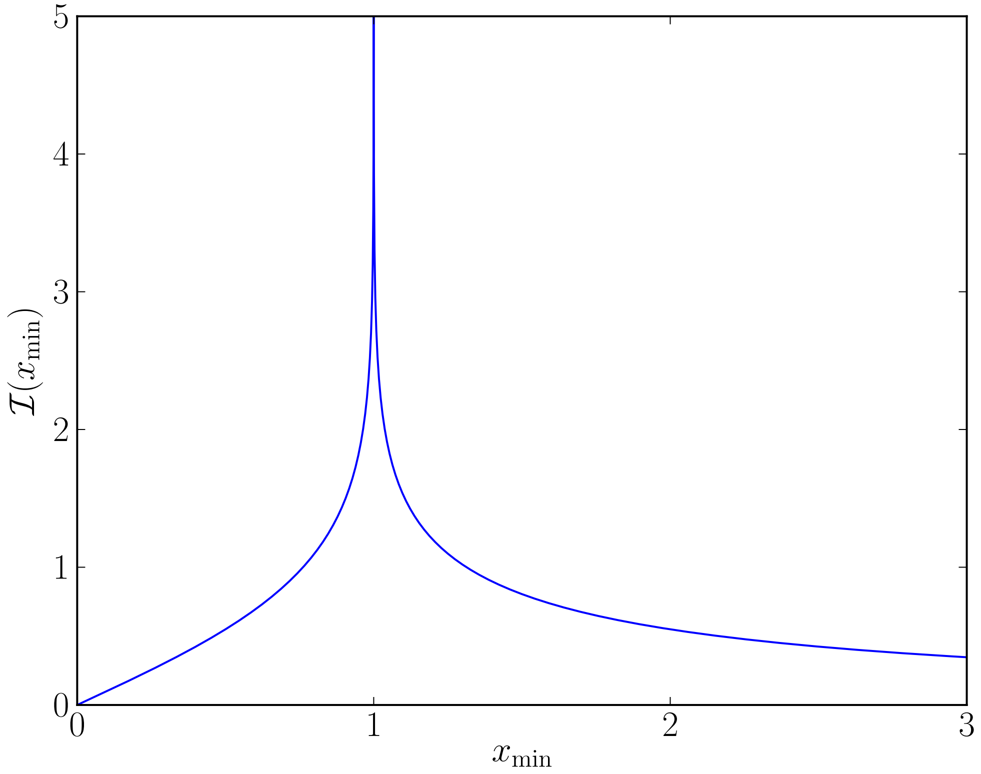

Figure 3.2: The integral of the IDRs with the σ = constant, $m_p \to 0$, and $f(0) = 0$ limits taken. We see the expected singularity at $x_{\rm min} = 1$. For the new physics contribution, $x_{\rm min} = E_{\rm tr}/E$.

in Δ they are identical, as they must be to give a finite principal value integral. At higher order in Δ, the second integral exceeds the first integral. So we expect $\mathcal{I}(x_{\text{min}})$ to show symmetry about the singular value $x_{\text{min}} = 1$ for small deviations, but a larger value above $x_{\text{min}} = 1$ than below for larger deviations. This expectation is visible in fig. 3.2.

The simplest (and as such perhaps most informative) model of new physics discussed here that of a simple step function described in §5.2. In that model we have the standard cross section (considered here as σ_0) that then increases by a factor of D at a threshold E_{tr} and then continues in the same fashion in E. In the context of these approximations, the part of the cross section that does not change does not contribute to the observable, ρ, but the increase does. When new physics enters at a threshold energy E_{tr}, the contribution of the new physics to the dispersion integral begins at $x_{\text{min}} = \frac{E_{\text{tr}}}{E}$, where E is the energy of the accelerator. Thus, fig. 3.2 gives the shape of the new physics contribution as a function of the new physics threshold. In what follows, our much more realistic parametrizations of new physics will present curves that qualitative have the form given by the simplistic model discussed in this chapter.

We may summarize this chapter by saying that the SM cross section is expected to give a modest contribution to the dispersion integral (zero in our simplistic model of constant and equal pp and $p\bar{p}$ cross sections with vanishing proton mass). On the other hand, new physics enters at a nonzero threshold which implies an incomplete cancellation in the dispersion integral, and thus a possibly significant contribution to the dispersion integral. Therefore, the ratio of new physics to total physics as revealed in the IDR potentially offers an observable window to new physics even with threshold energy above the direct reach of the LHC. As we will see in §4.2, it is the non-uniform and non-identical assumption of $\sigma_{pp}, \sigma_{p\bar{p}}$ rather than the non-zero mass of the proton assumption that accounts for the difference between this simplifying case and the complete description.

Chapter 4

Experimental Overview

4.1 New Physics in the ρ Parameter

4.1.1 Approach

While eq. 2.34 and the other versions of the IDRs relate the total cross section, σ_{tot}, at one energy to that at all other energies, this alone does not allow for the discovery of new physics. If the cross section has a measurable change at the machine's energy from IDRs due to new physics at higher energy scales, the presence of new physics can already be inferred via direct production of the new states without the additional use of IDRs. On the other hand, if the new physics cannot yet be produced directly, IDRs can infer the presence of new physics near the machine energy without any change in the cross section. A separate measurement must be made that makes proper use of the power of IDRs, and that is where the ρ parameter, defined in eq. 2.33, comes in.

The general strategy that we will use to explore new physics is to first use the IDR to calculate ρ at a particular energy (an LHC energy) without the inclusion of new physics by assuming that the cross section continues to rise in the expected fashion. Then we calculate ρ at the same energy with the inclusion of the new physics cross section. Since ρ can be calculated at experiments without IDRs in a model-independent fashion, as described in §4.1.2, enhancements of the cross section can be either identified or ruled out by comparing theoretical and experimental values of $\rho(E)$.

4.1.2 IDR Independent Calculation of ρ

To extract a value for ρ in an IDR independent fashion, one invokes the optical theorem and extrapolates $d\sigma/dt$ to $t = 0$, as shown below. The cross section is related to the scattering amplitude by a simple exponential at low $|t|$. Recall from eq. 2.11 that the differential cross section in the COM is

$$\frac{d\sigma}{dt} = \frac{\pi}{k^2}|f|^2 \,. \tag{4.1}$$

At $t = 0$ one has

$$\begin{aligned} \left.\frac{d\sigma}{dt}\right|_{t=0} &= \frac{\pi}{k^2}|\Re f(t=0) + i\Im f(t=0)|^2 \\ &= \frac{\pi}{k^2}|(\rho + i)\Im f(t=0)|^2 \,. \end{aligned} \tag{4.2}$$

Making use of the optical theorem, $\sigma_{\text{tot}} = (4\pi/k)\Im f(t=0)$, one arrives at

$$16\pi \left.\frac{d\sigma}{dt}\right|_{t=0} = (\rho^2 + 1)\sigma_{\text{tot}}^2 \,. \tag{4.3}$$

From [18], the pp differential cross section in the low t limit is well approximated by

$$\frac{d\sigma}{dt} \propto e^{Bt} \,, \tag{4.4}$$

where B is the "slope parameter," assumed and measured to be very nearly constant. Thus, a measurement or estimate of σ_{tot} and an extrapolation of $d\sigma/dt$ to $t = 0$ via the measured slope

Table 4.1: Fit parameters to eq. 4.5 from [9] with various analyticity constraints.

c_0(mb)	36.95
c_1(mb)	-1.350
c_2(mb)	0.2782
c_3(mb)	37.17
c_4(mb)	-24.42
α	0.453

parameter are sufficient to determine ρ independently from the IDRs. While σ_{tot} is often evaluated in the "luminosity-independent" sense which includes an estimation of ρ, it can also be evaluated (although, less precisely) using a luminosity calculated through particle counting or beam sweeping techniques.

We also note that since the determination of ρ actually gives a value for ρ^2 there is an additional sign ambiguity. There are two approaches to dealing with this. The first is to compare results from modified cross sections in IDRs to either the positive or negative values, treating each equally. The second is to note that the IDR results for ρ from all of the fits done to the pp, $p\bar{p}$ cross sections (regardless of whether or not they follow the Froissart bound) yield a positive value for ρ. In practice we use TOTEM's quoted upper limit on ρ statistically calculated from ρ^2 which accounts for the possibility that ρ could be negative and only places an upper limit on ρ (in essence an upper limit on $|\rho|$).

4.2 Forward Scattering Measurements and Fits

Fits to data suggest that the cross sections decrease with E until $E \sim 60$ GeV ($\sqrt{s} = 10.6$ GeV) and $E \sim 250$ GeV ($\sqrt{s} = 21.8$ GeV) for $pp, p\bar{p}$ respectively, before increasing. Furthermore, Froissart theory (§2.4.1) tells us that σ_{tot} asymptotically ($s \to \infty$) grows no faster than $\log^2$ of the energy, a fact that has been confirmed at currently available with fits to present experimental data [36].

The SM total $pp, p\bar{p}$ cross section σ_{SM} is typically parameterized as

$$\sigma_{SM}(E) = c_0 + c_1 \log\left(\frac{E}{m_p}\right) + c_2 \log^2\left(\frac{E}{m_p}\right) + c_3 \left(\frac{E}{m_p}\right)^{-\frac{1}{2}} \pm c_4 \left(\frac{E}{m_p}\right)^{\alpha-1}, \tag{4.5}$$

where m_p, the proton mass, is used as the energy scale. c_i, α are fit parameters with $\alpha < 1$. The $E^{-\frac{1}{2}}$ term is a result of invoking Regge behavior. The upper sign refers to pp scattering and the lower to $p\bar{p}$ scattering. The form of eq. 4.5 is motivated by being the most general and fastest rising form allowed by the Froissart bound. The values of the c_i and α from [9] are shown in table 4.1. The total pp cross section for the SM is included in fig. 5.1 (solid line, labeled as the h_0 case).

Note that our results are indifferent to different fits for the $pp, p\bar{p}$ cross sections because the current limits on the pp total cross section are predominately derived from data at and below the LHC. Fits to functions that behave differently than $\log^2(s)$ such as $\log(s)$ and s^ϵ have been essentially ruled out [36,37]. Auger does quote a value for the pp total cross section at 57 TeV [23], but the precision is low (a fractional error of 0.20) and depends on specifics built into the Glauber model. It does not severely limit the behavior of the cross section to high energies.

Concerning the first approximation of chapter 3, namely $m_p = 0$, we find that returning the physical, nonzero m_p to the integral eq. 3.4, which approximates ρ, (including $p'/E' \neq 1$) gives nonzero but negligible integral values of the integral of 2.649×10^{-8} and 5.966×10^{-9} at LHC energies $\sqrt{s} = 7$ and 14 TeV. On the other hand, keeping m_p zero but returning to σ_{pp} and $\sigma_{p\bar{p}}$

their realistic energy dependences yields nonzero integral values of 0.1345 and 0.1309 at $\sqrt{s} = 7$ and 14 TeV. And finally, using nonzero m_p and realistic pp and $p\bar{p}$ cross sections returns the values 0.1345 and 0.1309 at $\sqrt{s} = 7$ and 14 TeV. The final two integration sets (realistic σ's and zero or nonzero m_p) agree to about seven to eight decimal places respectively (on the order of m_p^2/s). The conclusion is that the $m_p \to 0$ approximation is generally a valid one, whereas the constant and equal SM cross section approximation in the previous section is not. However, the integral contributions of the SM to the IDRs (the solid lines in fig. 6.1) are not large, and we are encouraged to pursue further the contributions that might arise due to physics beyond the SM.

For the subtraction constant, we will take $f(0) = 0$, since the value from the fits above is $f(0) = -0.073 \pm 0.67$ mb GeV. We note that even at the value 1σ away from zero, the term $4\pi\, f(0)/(p\,\sigma_{pp})$ at LHC energies contributes less than one part in 10^5 to ρ.

4.3 The TOTEM Experiment

The TOTal Elastic and diffractive cross section Measurement (TOTEM) experiment at the LHC is designed to measure forward cross sections by probing very low $|t|$ regions [38]. TOTEM places a series of Roman pot detectors very close to the beam and very far from the interaction point. With improved LHC optics, TOTEM should be able to provide an improved measurement of ρ independent of IDRs [39]. A comparison of TOTEM's ρ, so determined, with the IDR prediction of ρ, then provides the potential evidence for new physics.

Similarly, the Absolute Luminosity For ATLAS (ALFA) [40] experiment, the LHC forward (LHCf [41] experiment, along with a host of others will also make comparable measurements in an attempt to improve the precision of the luminosity calculation, which is necessary to infer σ_{tot}, and then to infer ρ without the use of IDRs [42] (see §4.1). Thus, there are several experiments that aim to measure the total cross section. These offer hope for smaller error bars on IDR independent determinations of the crucial parameter $\rho(E)$.

A $\sqrt{s} = 7$ TeV, the TOTEM article presented a state of the art value for the IDR independent ρ, of $\rho = 0.145$ with error bars of $\sim 60\%$ [20]. TOTEM cited a 95% significance level (roughly speaking, a 2σ bound) that $\rho < 0.32$. Comparing this to the SM prediction of $\rho(\sqrt{s} = 7 \text{ TeV}) = 0.1345$ gives an upper limit of the fractional increase $(\rho - \rho_{\text{SM}})/\rho_{\text{SM}} = 1.38$ at the 95% significance level. For brevity, in what follows we denote $(\rho - \rho_{\text{SM}})/\rho_{\text{SM}}$ as $\Delta\rho/\rho$. In addition, an early report from TOTEM gives their error estimate as ~ 0.04 from their $\sqrt{s} = 8$ TeV analysis [43] corresponding to a fractional error of 30%, thus cutting the error in half.

As an illustrative example of what a future determination of ρ might mean for the IDR technique, we investigate a definite value for ρ; we choose as the definite value the experimentally inferred mean value $\rho(\sqrt{s} = 7 \text{ TeV}) = 0.145$. For this example, the fractional increase in ρ is $\Delta\rho/\rho = 7.8\%$. This value for ρ is chosen for illustration only, as it offers insight into the merit of IDRs should experiments greatly reduce their errors in the inference of ρ.

Compared to the presently published TOTEM error of 63%, the "new physics increase" has negligible significance, $\sim 0.1\sigma$. With the ongoing analysis at TOTEM, the new significance is expected to be $\sim 0.25\sigma$ [43]. Clearly, further improvement in the inference of ρ is needed for the program constructed in this part. Another reduction in error by about a factor of four (eight) would give a $1(2)\sigma$ significance to our illustrative example. One must hope that either the measured error is reduced significantly in the next LHC run, the new physics contribution to the cross section is larger than our chosen example, or both.

Chapter 5

Modifying the Cross Section

5.1 General Modification

We consider a class of modifications to the total pp cross section of the form

$$\sigma(s) = \sigma_{\mathrm{SM}}(s)[1 + h_i(s)]\,, \tag{5.1}$$

where σ_{SM} is the SM cross section. That is, it is the cross section that has been observed so far consistent with SM physics. σ is the true cross section. In general, the h_i will be zero up to some threshold s_{tr} and $0 \leq \lim_{s\to\infty} h_i(s) < \infty$. We apply the same enhancement to both σ_{pp} and $\sigma_{p\bar{p}}$ since, by the Pomeranchuk theorem discussed in §2.4.2, each cross section should respond to new physics in the same way at energies well above the proton mass.

We use this form as it allows for modifications to turn on at an arbitrary energy, preserving the measured fit, but also retaining the asymptotic limit predicted by the Froissart bound in §2.4.1. This form guarantees that σ will continue to grow at the same rate at σ_{SM}.

The first model we will present in §5.2 is a simple step function at s_{tr}. This model results in an especially close analogy to the idealized IDRs we discussed in chapter 3. In particular, this model yields a singularity in the IDR integrand at $E = E_{\mathrm{tr}}$ and therefore a singular value for $\rho(E = E_{\mathrm{tr}})$.

More realistically, we expect phase space to present a cross section for new physics that has no jump discontinuity at threshold. For example, two body phase space is $\beta/8\pi$, where β is either particle velocity in the COM frame; at threshold, β is identically zero. Furthermore, including parton distribution functions to the model also yields a zero cross section at threshold. The new physics matrix elements may also vanish right at threshold. So we are led to the next two models of BSM physics. The second model we present in §5.3 involves hard-scattering parton production of new particles, while the third model in §5.4 is constructed from diffractive phenomenology. The second and third models provide cross section modifications that vanish at threshold, leading to finite values for $\rho(E = E_{\mathrm{tr}})$.

Since only the first model, the step function, yields a nonzero change in the cross section at threshold, the ρ-value resulting from model h_1 should be considered an upper bound to the contribution of new physics BSM. The bounding of cross sections by the h_1 step function model is evident in fig. 5.1, where we show the SM cross section (given by zero enhancement and labeled by $h_0 = 0$) and its enhancements ($h_i, i = 1, 2, 3$) by the three new physics models that are presented in detail below.

No new conserved quantum number is assumed in our models (valid, e.g., for broken R-parity SUSY models). Thus, energy is the only impediment to production of heavy new single particles, and the heavy single mass value M_χ determines E_{tr}. Without a new quantum number, the new particle would decay to SM particles, and due to its large mass, decay very quickly. Consequently, other than invariant mass combinatorics, there is no good signature of the new particle's production. One may have to rely on IDRs and/or an anomalous $\Delta\sigma$ for new particle identification. Thus, we plot $\Delta\rho/\rho$ and $\Delta\sigma/\sigma$ versus M_χ ($M_\chi = \sqrt{s_{\mathrm{tr}}} - 2m_p \approx \sqrt{s_{\mathrm{tr}}}$), to see if the IDR technique can identify new physics via an anomalous ρ measurement, before the new physics would be directly noticeable in the cross section increase at the next high energy collider.

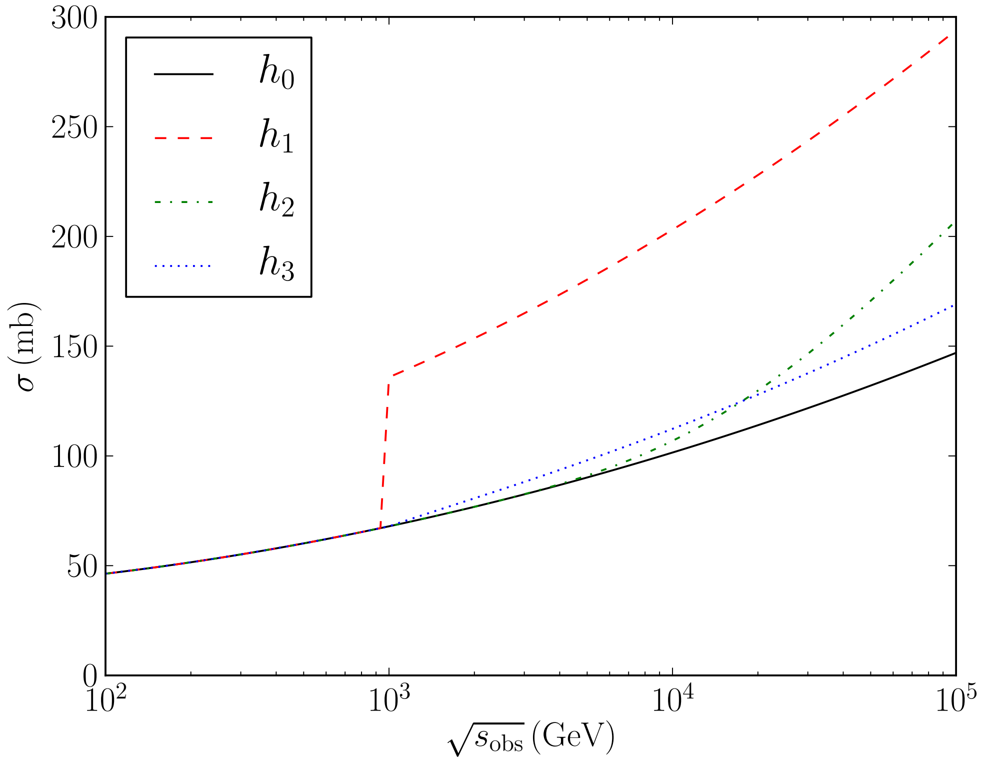

Figure 5.1: The pp total cross sections $\sigma_{\mathrm{SM}} + \sigma_{\mathrm{BSM}}$ are plotted, for the choice $\sqrt{s_{\mathrm{tr}}} = M_{\chi} = 10^3$ GeV. Doubling of the cross section at threshold is assumed for the h_1 model, i.e., $D = 1$. The SM cross section uses the parameters [9] shown in table 4.1, and leads to an error in the SM value of ρ of less than 1% [10]. The slow initial rise in h_2 is a result of the parton distribution functions. While the high energy behavior of h_3 is small compared to other models, it rises quickly at threshold, in contrast to h_2.

5.2 Step Function Modification

A simple example function for BSM physics is

$$h_1(s) = D\,\Theta(s - s_{\mathrm{tr}})\,, \tag{5.2}$$

a step-wise jump in cross section at the threshold COM energy $\sqrt{s_{\mathrm{tr}}}$. The parameter D is a measure of the size of the new cross section relative to the SM. For example, in the event that new physics exactly doubles the cross section at $s = s_{\mathrm{tr}}$, then $D = 1$. Modifying σ_{SM} in the form of eq. 5.2 guarantees that the new total cross section σ continues to grow as fast as $\sigma_{SM} \propto \log^2 s$ (but not faster), and that the new physics contribution remains large over a sizable energy range beyond the threshold energy.

As mentioned above, an unphysical aspect of the step function enhancement is a non-vanishing cross section at threshold, which leads to the uncanceled singularity in the IDR integrand at $E = E_{\mathrm{tr}}$ and a singular value for $\rho(E = E_{\mathrm{tr}})$ as shown in figs. 3.1 and 3.2. However, the model has redeemable value in that the width of the singularity is small since it is valid away from the singularity. Thus, the model offers a meaningful upper bound to new particle production away from the singularity.

5.3 A Partonic Model of New Physics

The most popular model of new physics at the electroweak symmetry breaking scale is R-parity preserving supersymmetry (SUSY), with masses tuned to the EW scale to stabilize the ratio m_h/M_{Planck} (the "hierarchy problem"). Unfortunately, R-parity conservation requires s, t, and u to have EW-scale values, which severely suppresses the SUSY cross section to $\sim 10^{-10}$ times the SM cross section. However, as LHC limits on R-parity conserving SUSY are becoming more constraining, R-parity violating (RPV) models are getting a closer look by theorists and the LHC experimentalists alike [44–48]. If R-parity is violated, we can replace one final state particle from a SM process with an effectively identical heavier counterpart for each possible final state. Then the only difference between the modified cross section and the SM cross section comes in the form of the reduced final state phase space and the threshold parton energy. Importantly, the fast growing $\log^2 s$ contribution to the SM σ_{tot}, which arises from soft and collinear gluon divergences, may be maintained. Also, other exotic models with extra dimensions [49] and a non-conserved Kaluza-Klein number resulting from additional compactified dimensions [50, 51] might grow a large cross section as a power law instead of the Froissart $\log^2 s$ limit. In what follows we present the phase space modification necessary to describe such a new physics modification on the total cross section.

Let $\sigma_i(s) = \sigma_i(pp \to \ldots)$ be the SM cross section and $\sigma_i^{\mathrm{BSM}}(s) = \sigma_i(pp \to \chi + \ldots)$ be the new physics contribution, where $i = \{\mathrm{el,\ inel,\ tot}\}$, and dots denote additional SM particles in the final states. Hats will denote parton cross sections instead of pp cross sections. We note that since $\sigma_{\mathrm{el}}^{\mathrm{BSM}} = 0$, then $\sigma_{\mathrm{inel}}^{\mathrm{BSM}}$ must equal $\sigma_{\mathrm{tot}}^{\mathrm{BSM}}$. Then the physical total pp cross section is $\sigma_{\mathrm{tot}} + D\sigma_{\mathrm{inel}}^{\mathrm{BSM}} = \sigma_{\mathrm{tot}}(1 + Dh_2(s))$ where $h_2 = \sigma_{\mathrm{inel}}^{\mathrm{BSM}}/\sigma_{\mathrm{tot}}$, in the form of eq. 5.1.

We start with a partonic expression of the conservation of momentum for the new physics contribution.

$$\sigma_{\mathrm{tot}}^{\mathrm{BSM}}(s) = \sum_{i,j} \int_{(\hat{s} > M_\chi^2)} dx_1 dx_2 f_i(x_1) f_j(x_2) \sigma^{\widehat{\mathrm{BSM}}}{}_{\mathrm{tot}}(\hat{s})\,, \tag{5.3}$$

where $\hat{s} \approx x_1 x_2 s$ is the parton COM energy and the f_i are the various parton distribution functions (pdfs). Let the SM final state masses be zero. The summations are over parton types and the integrals are over the accessible x_1, x_2 space: $\hat{s} > M_\chi^2$.

If we assume that for each SM particle in the final state, there is an analogous new particle χ produced with the same coupling, then there is little t or u-channel propagator suppression (see appendix A), and so the matrix elements will be similar. The new, heavier final state masses suppress only the available phase space. The two body phase space is

$$\frac{\sqrt{\lambda(s, m_3^2, m_4^2)}}{8\pi s} . \tag{5.4}$$

So we can set parameter $D = 1$, and write

$$\frac{\sigma^{\hat{\mathrm{BSM}}}{}_{\mathrm{tot}}(\hat{s})}{\sqrt{\lambda(\hat{s}, M_\chi^2, 0)}} = \frac{\hat{\sigma}_{\mathrm{inel}}(\hat{s})}{\sqrt{\lambda(\hat{s}, 0, 0)}} , \tag{5.5}$$

where the triangle function (symmetric in its arguments) is defined as

$$\lambda(a, b, c) = a^2 + b^2 + c^2 - 2ab - 2bc - 2ca , \tag{5.6}$$

and the two body phase space is

$$\frac{1}{8\pi s}\sqrt{\lambda(s, m_3^2, m_4^2)} . \tag{5.7}$$

The inelastic cross section shows up in the SM equivalent case since the related new particle cross sections must be inelastic.

It is easy to see that the relevant ratio can be simplified to

$$\sqrt{\frac{\lambda(\hat{s}, M_\chi^2, 0)}{\lambda(\hat{s}, 0, 0)}} = 1 - \frac{M_\chi^2}{\hat{s}} . \tag{5.8}$$

Then, combining eqs. 5.3, 5.5, and 5.8, and integrating out the internal $\sigma_{\mathrm{tot}}(\hat{s})$ which leaves behind a factor of $\hat{s}/s = x_1 x_2$, we obtain

$$\sigma_{\mathrm{inel}}^{\mathrm{BSM}}(s) = \sigma_{\mathrm{inel}}(s) \sum_{i,j} \int dx_1 dx_2 f_i(x_1) f_j(x_2) x_1 x_2 \left(1 - \frac{M_\chi^2}{\hat{s}}\right) . \tag{5.9}$$

Consistency of this model derivation gains support by noting that as either $M_\chi \to 0$ or $s \to \infty$, we recover the SM cross section (recalling that $\sum_i \int dx f_i(x) x = 1$ expresses conservation of momentum when the momentum of the parent nucleon is partitioned among partons).

Let us introduce the ratio $z \equiv \sigma_{\mathrm{inel}}/\sigma_{\mathrm{tot}}$. As suggested by the black disk limit, $z \to \frac{1}{2}$ as $s \to \infty$. However, data for the LHC $\sqrt{s} = 7$ TeV run, and cosmic ray data in the vicinity of $\sqrt{s} = 57$ TeV suggest that z is well (and conservatively) approximated as a constant $z \approx 0.7$ [37].[3] Our interest is the upcoming $\sqrt{s} = 14$ TeV LHC run, for which $z \approx 0.7$ is the appropriate value.

Finally, we arrive at our model of new physics:

$$h_2(s, M_\chi) = z \sum_{i,j} \int_{x_1 x_2 > M_\chi^2/s} dx_1 dx_2 f_i(x_1, M_\chi) f_j(x_2, M_\chi) x_1 x_2 \left(1 - \frac{M_\chi^2}{\hat{s}}\right) . \tag{5.10}$$

Of course, the pdfs $f_i(x, Q)$ also depend on the transfer energy Q, which we take to be M_χ. For our numerical work with pdfs, we use the CT10 parton distribution functions [52].

---

[3] We note that while $z \approx 0.7$ at LHC and Auger energies, the fit from [37] has $z \to 0.509 \pm 0.021$ as $s \to \infty$ as expected from the black disk limit; z converges to $\frac{1}{2}$ rather slowly on the scale of presently accessible energies.

Note that this model has a vanishing cross section right at threshold, (at $\hat{s} = M_\chi^2$), due to the $(1 - M_\chi^2/\hat{s})$ phase space ffactor, and due to the vanishing parton distributions at threshold. Thus, ρ is finite for all E values, including the peak at $E = E_{\rm tr}$. Furthermore, the rise from threshold is very slow, a notable feature of the h_2 model. This slow rise in h_2 is evident in fig. 5.1. We find that the slow rise is due to the suppressed pdfs near threshold; the phase-space reduction factor contributes a negligible suppression to the rise. We conclude that any deep inelastic model with partons as initial state particles will experience a similar slow rise from threshold. Finally, we note from eq. 5.10 that h_2 has a finite asymptotic value. In particular, $\lim_{s\to\infty} h_2 = z$. For our purposes we have fixed z at 0.7, yet extrapolating z as $s \to \infty$ likely gives $z = \frac{1}{2}$. This discrepancy in the constant value of z does not affect our results as IDRs are only sensitive to the local effects of the machine energy. In addition, we note that for comparison with Auger cross section measurements at 57 TeV, for new physics $M_\chi = 1, 5, 10$ TeV we have $h_2(57 \text{ TeV}) = 0.32, 0.053, 0.0099$ respectively, while the fractional uncertainty in $\sigma_{\rm tot}$ at 57 TeV is ~ 0.21 [23].

5.4 A Diffractive Model of New Physics

An alternative to the partonic approach presented in §5.3 is to consider general descriptions of pp inelastic cross sections without reference to partonic substructure. Inelastic cross sections can be described by the parameter $\xi \equiv M_X^2/s$. M_X is defined by first making a pseudorapidity,[4] η, cut at the mean η of the two tracks with the greatest difference in η. M_X is then taken as the larger invariant mass of the two halves. Ref. [53] provides a model form for the inelastic cross section. It is

$$\frac{d\sigma}{d\xi} \propto \frac{1+\xi}{\xi^{1+\epsilon}}\,, \tag{5.11}$$

where $\epsilon = \alpha(0) - 1$ and $\alpha(0)$ is the Pomeron trajectory intercept at $t = 0$. Values for ϵ are typically in the $[0.06, 0.1]$ range. We take the mean of this range, $\epsilon = 0.08$, in this part. Next, we note that $1 \geq \xi > m_p^2/s \equiv \xi_p$, since $\xi_{\rm min} = \xi_p$ describes elastic scattering. To find the total cross section, we integrate eq. 5.11 across $\xi \in [\xi_p, 1]$ and get

$$\sigma \propto \frac{(1-2\epsilon) + (\epsilon - 1)\xi_p^{-\epsilon} + \epsilon\xi_p^{1-\epsilon}}{\epsilon\,(\epsilon - 1)}\,. \tag{5.12}$$

As an interesting aside, we note that to $\mathcal{O}(\epsilon^1)$ in eq. 5.12, the leading energy behavior grows like $\log^2(s/m_p^2)$, thereby providing the expected asymptotic Froissart growth.[5] However, higher order terms in ϵ lead to higher logarithmic orders, indicating that eq. 5.12 is pre-asymptotic, more than sufficient for our use since IDRs are most sensitive to local effects.

We now consider a rapidity cluster containing a new particle of mass M_χ. With the substitution $\xi_p \to \xi_\chi \equiv M_\chi^2/s$ in eq. 5.12, divided by the SM case, we arrive at the useful ratio

$$R(M_\chi, s) \equiv \frac{\sigma_{\rm diff}^{\rm BSM}}{\sigma_{\rm diff}^{\rm SM}} = \frac{1 - 2\epsilon + (\epsilon - 1)\xi_\chi^{-\epsilon} + \epsilon\xi_\chi^{1-\epsilon}}{1 - 2\epsilon + (\epsilon - 1)\xi_p^{-\epsilon} + \epsilon\xi_p^{1-\epsilon}}\,. \tag{5.13}$$

Next we note the relation in eq. 5.11 describes single dissociative processes, which constitute only 15% of the inelastic cross section. We make the model assumption that the remaining 85% of the inelastic cross section, including double dissociative and non-diffractive processes, are also governed

---

[4] Pseudorapidity, defined by $\eta \equiv -\log\left(\tan\frac{\theta}{2}\right)$, provides a measure of the separation of tracks in a detector.

[5] The $\log^2(s/m_p^2)$ growth is perhaps best revealed by first expanding eq. 5.11 in ϵ, as $\frac{d\sigma}{d\xi} \propto \frac{1+\xi}{\xi}\,(1 - \epsilon\ln\xi + \cdots)$ and then integrating.

by the form in eq. 5.11. Finally, we include the factor $z = \sigma_{\rm inel}/\sigma_{\rm tot} \approx 0.7$ described in §5.3, and make explicit the on-shell requirement $M_\chi^2 \leq s$ with a Heaviside function, to arrive at our final model expression

$$h_3(s) = z\,\frac{1-2\epsilon+(\epsilon-1)\xi_\chi^{-\epsilon}+\epsilon\xi_\chi^{1-\epsilon}}{1-2\epsilon+(\epsilon-1)\xi_p^{-\epsilon}+\epsilon\xi_p^{1-\epsilon}}\Theta(1-\xi_\chi)\,. \tag{5.14}$$

As with model h_2, model h_3 has the desirable feature that the BSM cross section vanishes at threshold (here, $\xi_\chi = 1$). Thus, ρ is finite all energies, including the peak at $E = E_{\rm tr}$.

In fig. 5.1 we see that the h_3 model rises more quickly at threshold than the h_2 model, but attains a smaller asymptotic value:

$$\lim_{s\to\infty} h_3(s) = z\left(\frac{m_p}{M_\chi}\right)^{2\epsilon} \approx 0.23\left(\frac{1\ \text{TeV}}{M_\chi}\right)^{2\epsilon}\,, \tag{5.15}$$

i.e., about a 25% increase beyond the SM cross section. This faster rise but lower asymptotic value for h_3 compared to h_2 is evident in fig. 5.1. Note that with the appropriate $z \to \frac{1}{2}$ correction discussed in the previous subsection, the coefficient drops from $0.23 \to 0.16$. In addition, we note that for comparison with Auger results at 57 TeV, for $M_\chi = 1$, 5, or 10 TeV we have h_3(57 TeV) = 0.14, 0.080, or 0.058 respectively.

Chapter 6

Results

For each of the three models discussed in chapter 5, we calculate the effect they have on ρ. The parameter considered is the fractional increase in ρ, given as $\Delta\rho/\rho \equiv (\rho - \rho_{\mathrm{SM}})/\rho_{\mathrm{SM}}$. This is then related to the TOTEM results at $\sqrt{s} = 7$ TeV. We consider the mean value from their experiment as an example signal: $\rho = 0.145$ (± 0.091, 1σ confidence level) is compared to the SM prediction of $\rho = 0.1345$, a value which implies a fractional increase of $\Delta\rho/\rho = 0.0781$. The error in the theoretical calculation of ρ from existing measurements is $< 1\%$ [10]. This error is negligibly small compared to the effects presented here; we are justified in neglecting this error. We also look at the TOTEM upper limit, given as $\rho < 0.32$ at the 2σ confidence level, leading to a maximum fractional increase of $\Delta\rho/\rho < 1.38$ (2σ).

In what follows we conservatively neglect the increase in the elastic cross section due to new physics. This increase is model dependent. With the simplest assumptions, unitarity yields

$$\frac{\sigma_{\mathrm{el}}}{\sigma_{\mathrm{inel}}} = \frac{\eta}{2-\eta}\,, \tag{6.1}$$

where $0 < \eta \leq 1$ is a measure of the absorption [54]. In general η may vary with the partial wave value J. We also note that $\eta = 1$ corresponds to the black disk limit, but the LHC is pre-asymptotic.

6.1 Results From the Step Function Model

The step function enhancement of ρ is shown in fig. 6.1. As expected, a shape very similar to that of fig. 3.2 results. For comparison, the SM behavior of ρ is also shown. Here we have taken $D = 1$ and $\sqrt{s_{\mathrm{tr}}} = 20$ TeV. We see for a doubling of the cross section at $\sqrt{s_{\mathrm{tr}}} = 20$ TeV, a small increase in ρ is evident already at an energy an order of magnitude below $\sqrt{s_{\mathrm{tr}}} = 20$ TeV, and that ρ increases by nearly a factor of four at $\sqrt{s_{\mathrm{obs}}} = 14$ TeV.

Next, we look at what range of $\sqrt{s_{\mathrm{tr}}}$ and D values will give an large increase in ρ. The left and right panels of fig. 6.2 show contours of $\Delta\rho/\rho$ in the ranges $D \in [0,1]$ and $D \in [0,10]$. The $D \in [0,1]$ range of the left panel may be relevant to broken R-parity violating SUSY-like models, in which some or all of the SM particles might be doubled. The larger D range is plotted in the right panel, to show the increased reach of IDRs for still larger cross sections, as might be the case with extra-dimensional models. For the simple case of a step function with a significant increase in cross section, we see that IDRs offer a very powerful window to physics BSM.

Also displayed in fig. 6.2 are the regions of the generous h_1 step function model that are ruled out at 95% significance by these TOTEM results. The IDR technique is sensitive to a large range of $(\sqrt{s_{\mathrm{tr}}}, D)$ parameter space of the h_1 step function model, even with the currently large TOTEM errors on the IDR independent ρ. In particular, the IDR technique is sensitive to new energy thresholds well beyond the direct energy reach of the LHC. A minimal inference to be drawn from the 95% confidence level exclusion in the figure is that the cross section cannot increase particularly quickly near the LHC energy $\sqrt{s} = 7$ TeV.

Going forward, improvements are planned for the TOTEM optics, which will reduce the errors on ρ and thereby increase the sensitivity of the IDR toolkit to BSM physics.

Shown also in fig. 6.2 is the contour corresponding to our $\rho = 0.145$ example signal. Our example value of ρ is taken from the TOTEM experiment's inferred mean value. If such a signal

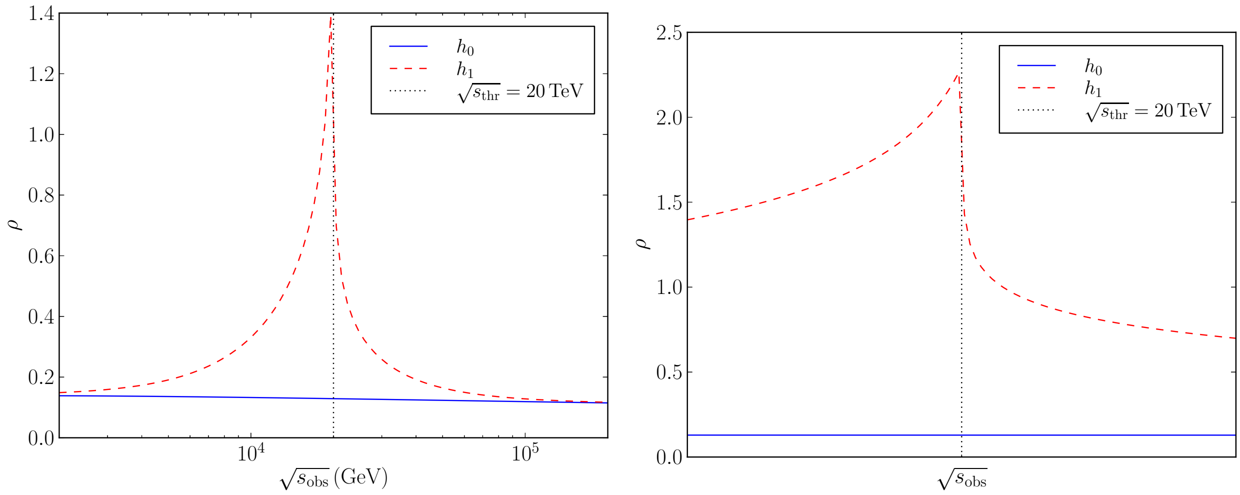

Figure 6.1: At observational energies around LHC energies, the SM ρ (solid line) remains roughly constant. Using the step function enhancement h_1 with $D = 1$ and $\sqrt{s_{\rm tr}} = 20$ TeV, we find a dramatic increase in ρ well below the new particle threshold. The right panel is an expanded piece of the left panel with a width of ~ 500 GeV on each side of the threshold energy, better showing the asymmetry of ρ about its singular peak value.

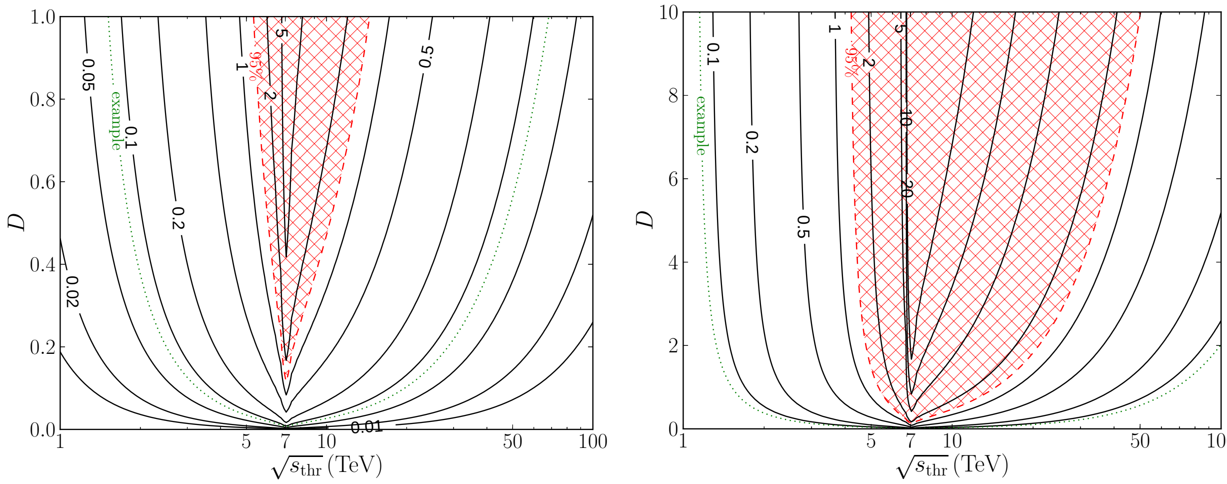

Figure 6.2: At $\sqrt{s_{\rm obs}} = 7$ TeV, the contours are parameterized by $\Delta\rho/\rho$. The form of the enhancement that includes new physics is h_1 – the step function. The left panel considers D in the range [0,1], which is the relevant parameter space for SUSY-type models. The right panel considers D values up to 10, relevant for extra-dimensional theories that have arbitrarily large increases in the cross section. The shaded regions have already been ruled out by TOTEM's $\sqrt{s} = 7$ TeV preliminary results. The dotted green contours correspond to the $\rho = 0.145$ example signal.

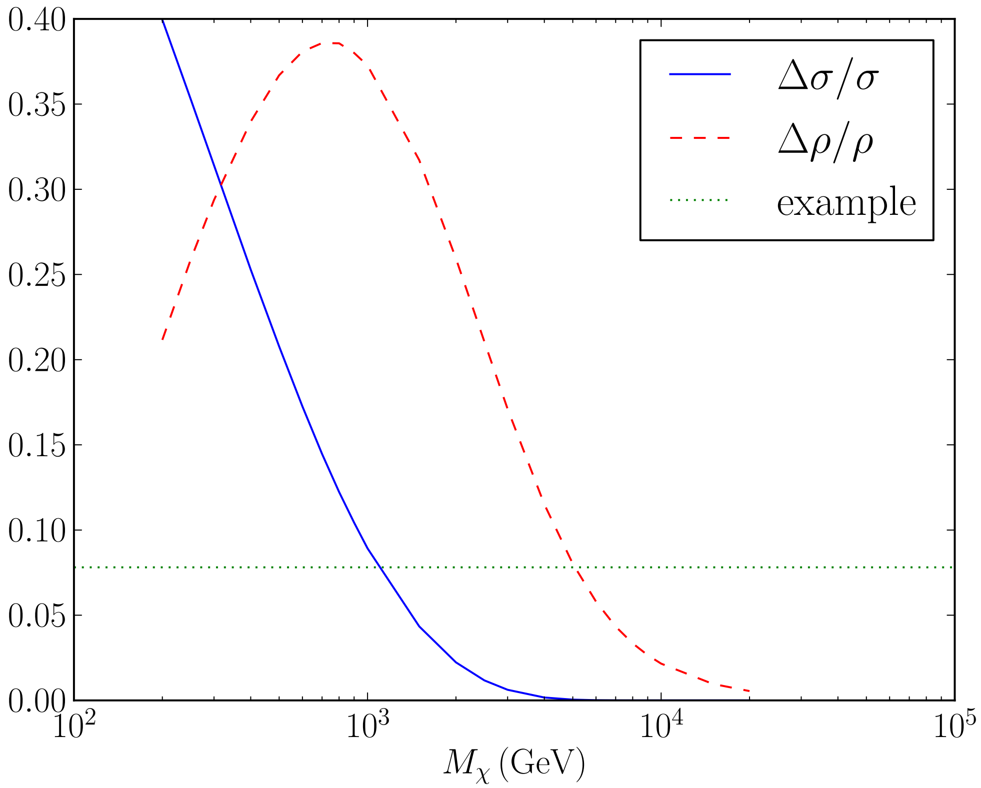

Figure 6.3: The fractional increases in ρ and σ using $h_2(s)$ at $\sqrt{s_{\text{obs}}} = 7$ TeV, versus M_χ. With the present significance of ρ data, the exclusion region is well above the top of the graph. The location of the peak is determined by the pdfs. The dotted green line labeled example presents the value of $\Delta\rho/\rho$ corresponding to the $\rho = 0.145$ example signature; from intersecting lines, a new $M_\chi = 5.1$ TeV threshold is predicted.

were statistically and systematically significant, we would expect new physics to show up as an increase in the *pp* cross section of height D and threshold $\sqrt{s_{\text{tr}}}$ somewhere on this contour. (We don't consider a signal of new physics at energies much below the machine energy, as direct detection of new event topologies or increased cross section would likely provide a better signal than a change in ρ as inferred through IDRs.)

We now turn to our more realistic models, h_2 and h_3, describing the onset of new physics. The h_1 model contains two parameters, D and E_{tr}, and so for this model we showed the prediction for $\Delta\rho/\rho$ as a contour plot. With the h_2 and h_3 models, there is no analog of D, and the only parameter is E_{tr}. Thus, we may show $\Delta\rho/\rho$ and $\Delta\sigma/\sigma$ for these models as simple ordinates versus the mass M_χ of the new particle, and we do so. With these models, our enthusiasm for the IDR approach will be somewhat tempered.

6.2 Results From the Partonic Model

Results for the partonic h_2 model are displayed in fig. 6.3, for future runs of the LHC at $\sqrt{s} = 14$ TeV.

For a small range of M_χ values, it is seen that $\Delta\rho/\rho$ is significantly larger than $\Delta\sigma/\sigma$. However, at present, the errors on the IDR independent ρ measurement ($\Delta\rho/\rho \lesssim 1.38$ at 2σ) are much larger than the accuracy (∼5%) with which energy-dependent changes in the total cross section can be inferred, so care is warranted here. From fig. 6.3 we can estimate a region of energy in the 2-5 TeV range for which $\Delta\rho/\rho \gtrsim 0.1$ and $\Delta\sigma/\sigma \lesssim 0.05$.

Our inference is that for new particle masses in the ∼2-5 TeV energy range, IDR independent measurements of ρ to an accuracy of one part in ten could reveal new physics of the type described by h_2 in section 5.3 at $\sqrt{s_{\rm obs}} = 7$ TeV.

One may wonder why the peak in ρ occurs so far below the machine energy of 14 TeV. The reason is the slow rise of the BSM cross section due to suppression from the pdfs: a peak at energy $E_{\rm tr} \sim \sqrt{s}$ weighted by the mean value of the parton momenta product, $\langle x_1 x_2 \rangle$, gives a peak at roughly an order of magnitude below the machine energy. A second inference is that models with new physics arising from initial state partons will enhance the value of ρ mainly below the machine energy. Of course, such models will also enhance the cross section below the machine energy, as seen in fig. 6.3.

There is still a small increase in ρ at the machine energy of $\sqrt{s_{\rm tr}} > 7$ TeV due to particle masses beyond 7 TeV. Beyond the machine energy, it is impossible for direct production to occur, so an inference of nonzero $\Delta\rho/\rho > 0$ due to particle masses beyond $\sqrt{s_{\rm tr}} > 7$ TeV would present a unique, and striking, discovery. Unfortunately, in the h_2 model, such an inference does not seem possible, as $\Delta\rho/\rho$ is $\lesssim 0.01$ for new particle masses just beyond 7 TeV. A more optimistic inference is that, if the cross section were to rise much more quickly than that of the h_2 model, as happens with a Kaluza-Klein tower of new particles, it may be possible to infer such new physics even if the threshold energies/new masses exceed the LHC energy.

We see that our example signal, plotted in fig. 6.3, implicates a new mass-scale $M_\chi = 5.1$ TeV. (The example $\Delta\rho/\rho$ also crosses the continuous curve at an energy below the machine energy; we assume that any new physics at this lower energy would be detected through more direct means.)

6.3 Results From the Diffractive Model

Finally, the h_3 model is plotted in fig. 6.4 at $\sqrt{s_{\rm obs}} = 7$ TeV. We see a modest contribution to ρ from the h_3 modification, as compared to that of the h_2 model. The larger contribution is due to the faster rise of the h_3 model from threshold ($s_{\rm tr} = M_\chi^2$). The non-partonic nature of model h_3 is at the heart of the larger, higher-energy peak. On the other hand, the effect of the smaller increase as $s \to \infty$ as described by eq. 5.15 can be seen in fig. 6.4 by the fast fall off in $\Delta\rho/\rho$ beyond $\sqrt{s} = M_\chi$.

We note that while no regions of M_χ parameter space can yet be excluded, our example signal implicates a new $M_\chi = 9.1$ TeV mass-scale. (We again ignore the lower energy crossing, where any new physics might be probed in a more direct manner.) This ~ 9 TeV mass-scale has not been directly probed at the LHC, and likely will be only weakly probed even at the 14 TeV run.

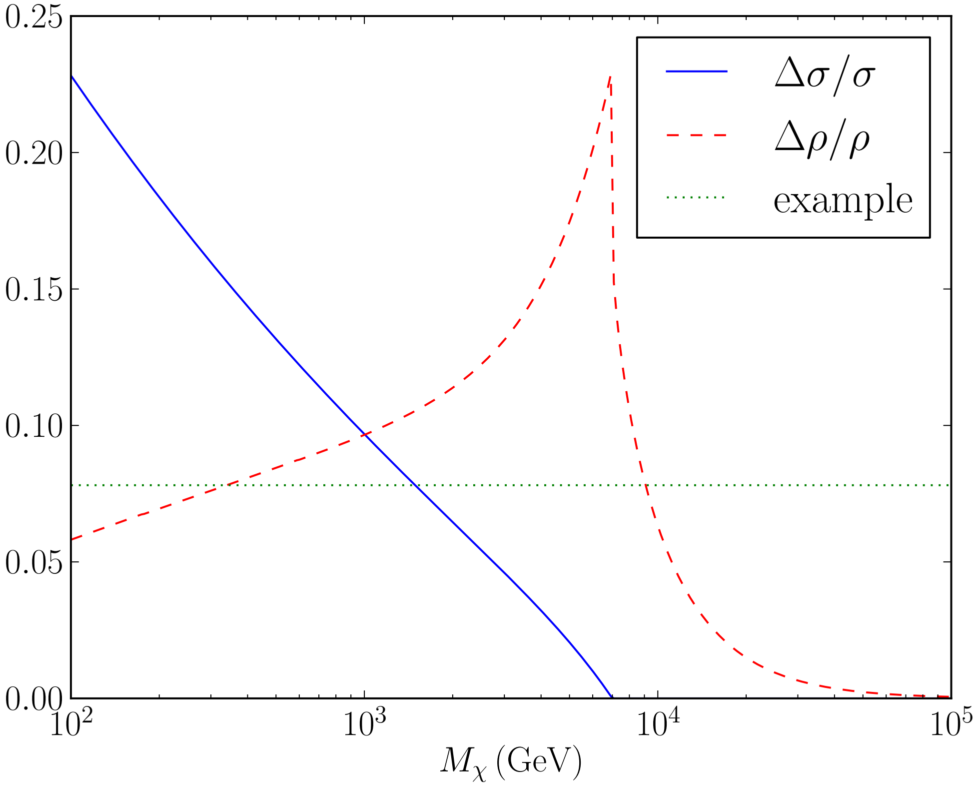

Figure 6.4: The fractional increase in ρ and σ for the h_3 model, at $\sqrt{s} = 7$ TeV. The increase in ρ compared to its SM value shows a peak of 0.23 at $M_\chi = \sqrt{s_{\text{obs}}}$. We also see that ρ has increased compared to its SM value slightly across a range of energies beyond the observation energy. With the present significance of ρ data, the exclusion region is well above the top of the graph. The location of the peak is at threshold since h_3, like h_1, is discontinuous at threshold. The dotted green line presents the value of $\Delta\rho/\rho$ corresponding to the $\rho = 0.145$ example signature; from intersecting lines, a new $M_\chi = 9.1$ TeV threshold is predicted.

Chapter 7

Conclusions

In the h_1 and h_3 models, the peak sensitivity of $\Delta\rho/\rho$ occurs when the new mass/new physics threshold is right at the machine energy. The sensitivity then falls off rapidly with increasing mass/threshold. However, the phase space for new particle production with mass at the machine energy is zero. Thus, a cross section measurement will not show an increase for such a mass value. However, the ρ-parameter will show a peak increase. Thus, the IDR technique primarily extends the reach of the LHC, to particle masses at the very end point of the machine energy. The LHC discovery potential is also extended beyond the machine energy, but with less sensitivity. In the h_2 model, the parton fractional momenta move the peak sensitivity to lower energies (by about an order of magnitude), thereby lessening the utility of the IDR technique for extending the LHC discovery potential to the machine energy and beyond.

It appears that this IDR technique may be sensitive to some reasonable models with large changes to the pp cross section, which have thresholds exceeding the reach of more direct detection.

The outlook for the near future is dependent on new measurements of ρ from experiments like TOTEM. The $\sqrt{s} = 8$ TeV data from TOTEM is in the process of being analyzed [55], and we eagerly await data from future LHC runs probing higher energies.

Appendix

A Minimum Transfer Energy in Two Lights to Light + One Heavy Processes

We need $|t|$ small in h_2 (see §5.3) to avoid amplitude suppression by propagators. Here we calculate the kinematic range of t in the $2 \to 2$ process $p_1 + p_2 \to k_1 + k_2$, with $p_1^2 = p_2^2 = k_2^2 = 0$ all labeling SM particles and $k_1^2 = M_\chi^2$ labeling a new heavy particle. We will see that $t = 0$ is allowed, leading to an unsuppressed amplitude for massless particle exchange.

Let θ be the angle between p_1 and k_1 in the COM frame. Then the transfer energy squared is

$$\begin{aligned} t &= (p_1 - k_1)^2 && \text{(A.1)} \\ &= M_\chi^2 - 2(p_1^0 k_1^0 - |\mathbf{p}_1|\,|\mathbf{k}_1|\,\cos\theta)\,, && \text{(A.2)} \end{aligned}$$

where $k_1^0 = {\mathbf{k}_1}^2 + M_\chi^2$. So, $t_{\max\,/\,\min}$ are given by

$$t_{\max\,/\,\min} = M_\chi^2 - 2p_1^0 k_1^0 \pm 2|\mathbf{p}_1|\,|\mathbf{k}_1|\,, \tag{A.3}$$

at $\theta = 0, \pi$ respectively. Then we have

$$\begin{aligned} p_1^0 &= \frac{\sqrt{\hat{s}}}{2}\,, \qquad k_1^0 = \frac{\hat{s} + M_\chi^2}{2\sqrt{\hat{s}}}\,, \quad \text{and} && \text{(A.4)} \\ |\mathbf{p}_1| &= p_1^0, \qquad |\mathbf{k}_1| = \frac{\hat{s} - M_\chi^2}{2\sqrt{\hat{s}}}\,, \quad \text{and so} && \text{(A.5)} \\ p_1^0 k_1^0 &= \frac{\hat{s} + M_\chi^2}{4}\,, \qquad |\mathbf{p}_1|\,|\mathbf{k}_1| = \frac{\hat{s} - M_\chi^2}{4}\,. && \text{(A.6)} \end{aligned}$$

Then, the maximum/minimum values of t are

$$t = M_\chi^2 - \frac{\hat{s} + M_\chi^2}{2} \pm \frac{\hat{s} - M_\chi^2}{2} = \begin{pmatrix} 0 \\ M_\chi^2 - \hat{s} \end{pmatrix}, \tag{A.7}$$

where $t = 0$ occurs for the forward scattering $\theta = 0$ case, and the maximum $|t|$ transfer occurs for the backward scattering $\theta = \pi$ case. The $t_{\min} = 0$ result confirms that $pp \to \chi$+light particles will favor small $|t|$.

Part II

Ultra High Energy Cosmic Ray Anisotropy

Chapter 8

Introduction

8.1 Introduction

This part of the thesis is focused on ultra high energy cosmic ray (UHECR) anisotropy. A conference proceeding outlining this work can be found at reference [2]. Two articles on this can be found at references [3, 4]. The former of those two references is largely contained in chapter 12 while the later contains the content in the remaining chapters. In the remainder of this chapter we will outline the path of this part and motivate the study of UHECR anisotropy as well as discuss previous anisotropy searches. In chapter 9 we discuss the relevant modern UHECR experiments and the parameters used for the comparison between partial sky ground based experiments and space based full sky experiments. We present the tools we will be using to search for anisotropies in chapter 10. In chapter 11 we discuss the various approaches for reconstructing dipolar and quadrupolar anisotropies for experiments with full sky or partial sky exposure. Chapter 12 explains how anisotropies on certain scales, the quadrupole for the relevant experimental parameters, can be reconstrcuted for ground based partial sky experiments while using the simpler and more accurate approaches designed only for space based full sky experiments. We discuss the difficulties of distinguishing between dipoles and quadrupoles with partial sky experiments and how they are resolved by full sky experiments in chapter 13. Chapter 14 contains the results of the general comparison between full sky and partial sky experiments and chapter 15 contains our conclusions.

8.2 Motivation

Pierre Auger kicked off the field of high energy cosmic ray research when he realized that extensive air showers (EASs) implied the existence of very high energy cosmic rays in 1938 [56]. At the highest energies, $\sim 10^{20}$ eV, the flux drops to about one event per square kilometer per century. Measuring this flux requires extremely large experiments as have been built and proposed, see chapter 9.

Despite measuring the cosmic ray flux up to and beyond energies of 10^{20} eV (10^{11} GeV, 100 EeV), determining their properties has been less successful. It is unknown if the UHECRs[6] are protons or heavier nuclei [57, 58] or what their sources are. It is also unknown if the apparent suppression that lines up with that predicted from the GZK phenomenon is, in fact, due to the GZK phenomenon or if sources naturally end at the same energy. The properties of galactic [59, 60] and extragalactic magnetic fields [61] are also poorly understood with the latter being nearly completely unconstrained. Finally, the sources and acceleration methods of UHECRs are not yet understood and most models struggle to account for both the large maximum energy of UHECRs and the flux at those energies [62–67].

In light of this impressive list of unknowns, determining the sources of UHECRs is a top priority in disentangling these related questions. Once the identification of UHECR sources is complete, the path towards understanding the remaining questions will become more clear. To this end, however, little progress has been made. While Auger has noted some weakly significant signals [68], their current status is unclear [69]. TA recently found a 20° "hotspot" [70] at global significance of

---

[6] UHECR typically means $E \gtrsim 10^{19}$ eV or so, although this varies in the literature.

3.4σ with an expanded data set. None of these analyses have yet identified the source of UHECRs despite a plethora of different search techniques.

In this part, we take a simplifying approach. We attempt to maximize the ability for experiments to identify any deviation from isotropy using a maximally generalized mathematical framework. We adopt spherical harmonics as a tool to identify anisotropies at varying scales and address the strengths and weaknesses of them at partial sky ground based experiments and full sky space based experiments.

8.3 Previous Anisotropy Searches

No all sky observatory has yet flown. Consequently, the first full sky large anisotropy search was based on combined northern and southern hemisphere ground based data. The respective data came from the SUGAR [71] and AGASA [72] experiments, taken over a 10 year period. No significant deviation from isotropy was seen by these experiments, even at energies beyond 4×10^{19} eV [73]. More recently, the Pierre Auger Collaboration carried out various searches for large scale anisotropies in the distribution of arrival directions of cosmic rays above 10^{18} eV (an EeV) [74,75]. At the energies exceeding 6×10^{19} eV $= 60$ EeV, early hints for a dipole anisotropy existed, but these hints have grown increasingly weaker in statistical strength [76]. The latest Auger study was performed as a function of both declination and right ascension (RA) in several energy ranges above 10^{18} eV. Their results were reported in terms of dipole and quadrupole amplitudes. Assuming that any cosmic ray anisotropy is dominated by dipole and quadrupole moments in this energy range, the Pierre Auger Collaboration derived upper limits on their amplitudes. Such upper limits challenge an origin of cosmic rays above 10^{18} eV from long lived galactic sources densely distributed in the galactic disk [77]. In the $E > 8$ EeV bin, they did report a dipolar signal with a p value of 6.4×10^{-5} (not including a "look elsewhere" penalty factor) [78]. Their cutoff of ~ 8 EeV is above the galactic to extragalactic transition energy of ~ 1 EeV, but still below the GZK cutoff energy of ~ 55 EeV. Also, Telescope Array (TA), the largest cosmic ray experiment in the northern hemisphere, has reported a different weak anisotropy signal above their highest energy cut of 57 EeV [70].

Chapter 9

Experiments

The Pierre Auger Observatory is an excellent, largest in its class, ground based experiment. However, in the natural progression of science, it is expected that eventually ground based observation will be superseded by space based observatories. The Extreme Universe Space Observatory (EUSO) is proposed to be the first of its class, space based observatory, building upon ground based successes. In this chapter we outline the relevant parameters of the two main ground based experiments, the Pierre Auger Observatory and the Telescope Array, and a proposed space based experiment, the Extreme Universe Space Observatory.

9.1 Current Ground Based Experiments

The largest cosmic ray experiments currently are the Pierre Auger Observatory (Auger) and the Telescope Array (TA). These experiments will be the focus of this section.

9.1.1 Pierre Auger Observatory

The Pierre Auger Observatory (Auger) is situated in Argentina at 35.2°S, 69.5°W and is a hybrid detector designed to detect the extensive air showers (EASs) that result from the interaction of UHECRs and air particles using the atmosphere as a calorimeter. The experiment is made up of a surface detector (SD) and a fluorescence detector (FD). The SD is a collection of 1,600 tanks covering an area of 3,000 km^2. As a useful comparison, this is roughly the size of the state of Rhode Island. The tanks of water are about a meter deep and a meter and a half in radius to detect Cherenkov radiation charged particles with photomultiplier tubes and a reflective inner surface.

At about 1 km from the core of the EAS, muons saturate the signal, while the contribution from photons and electrons is negligible [79,80]. The FD is a collection of 24 telescopes positioned across four sites overlooking the SD array. The FD is designed to measure the light yield from nitrogen fluorescence of EASs on dark moonless nights [81]. This provides a more accurate calorimetric measurement that is then used to calibrate the SD for the remaining of the data [79].

A major success of this experiment is the measurement of the flux suppression above $\sim 4\times10^{19}$ eV due to the so called GZK[7] phenomenon [82–84]. The focus of UHECR anisotropy is in looking at the events with energies large enough that their sources must be relatively nearby due to the GZK phenomenon – this typically means with $E \gtrsim 55$ EeV which implies $d \lesssim 100$ Mpc. Above these energies anisotropies are expected to appear.

9.1.2 Telescope Array

Telescope Array (TA) in Utah at 39.3°N, 112.9°W provides a northern hemisphere complement to the southern hemisphere's Auger. TA is also a hybrid detector with a similar FD design as Auger with three sites each composed of multiple telescopes overlooking the SD array [85]. The TA SD

---

[7] The GZK process is where high energy protons lose energy when scattering off the cosmic microwave background radiation (CMB), mainly resonantly through a Δ baryon: $p+\gamma_{\text{CMB}} \to \Delta \to N+\pi$. There are also additional channels for protons to lose energy by scattering off the CMB, including higher Δ resonances and alternate decay channels that typically include more pions.

array covers an area of 700 km^2 made up of 507 SDs. The TA SDs are plastic scintillators which detect the electromagnetic component of showers [86]. In addition to covering the other part of the sky, TA also complements Auger by providing an important systematic check on Auger for key UHECR observables such as the spectrum of the flux and the composition of the UHECRs.

Recently, TA has announced the location of a "hotspot" – a 20° window with a slightly higher flux than expected – with global significance of 3.4σ [70].

9.1.3 Partial Sky Exposure

The exposure functions of ground based experiments cover only part of the sky, and are highly nonuniform across that part of the sky that they do see.

The relative exposure of a ground based cosmic ray experiment [87] is given explicitly by,

$$\begin{aligned} \omega(\delta) &\propto \cos a_0 \cos\delta \sin\alpha_m + \alpha_m \sin a_0 \sin\delta \\ \text{with} \quad \alpha_m &\equiv \begin{cases} 0 & \text{for } \xi > 1 \\ \pi & \text{for } \xi < -1 \\ \cos^{-1}\xi & \text{otherwise} \end{cases} \\ \text{and} \quad \xi &= \frac{\cos\theta_m - \sin a_0 \sin\delta}{\cos a \cos\delta} . \end{aligned} \tag{9.1}$$

Both Auger and TA are fully efficient at energies above 10 EeV [88], well below the threshold typically considered for UHECRs, ~ 50 EeV. The exposure is seen to depend on two experimental parameters, the latitude of the experiment, termed a_0 in conventional language, and the experiment's acceptance angle, θ_m. Also appearing in the formula is δ, the declination at which the relative exposure is to be calculated. Auger's latitude is $-35.2°$, and $\theta_m = 80°$ is the new [69] maximum zenith angle Auger accepts. The corresponding numbers for TA are $a_0 = 39.3°$; the value of θ_m varies across the literature, but does not affect this analysis – we take it to be $\theta_m = 45°$ from [89]. We have assumed that any longitudinal variation in exposure due to weather, down time of the machine, etc., is a random process whose average is independent of right ascension (RA). Thus, the detector is effectively uniform in RA. Auger recently modified their acceptance from $\theta_m = 60° \to 80°$ with the extension calculated using a different metric. The $S(1000)$ technique is used for zenith angles $\theta \in [0°, 60°]$, and the N_{19} muon based technique is used for the new range, $\theta \in [60°, 80°]$. These inclined events extend Auger's reach up to a declination on the sky of $+45°$, as can be seen in fig. 9.1. In contrast, a space based observatory such as EUSO would see in all directions with nearly uniform exposure as shown in fig. 9.2. Throughout this work we will take EUSO's exposure to be exactly flat since the corrections are small.

9.2 Future Space Based Experiments

Proposals currently exist for all sky, space based cosmic ray detectors such as the Extreme Universe Space Observatory (EUSO) [90] and the Orbiting Wide Angle Lens (OWL) [91]. In addition, work is currently underway to combine datasets from the two large ground based experiments, Auger in the southern hemisphere and TA in the northern hemisphere [88]. This work will use EUSO as the example for a full sky observatory, but our conclusions will apply to any full sky observatory.

EUSO is a down looking telescope optimized for near ultraviolet fluorescence produced by extended air showers in the atmosphere of the Earth in a similar fashion to the FDs of Auger and TA. EUSO was originally proposed for the International Space Station (ISS), where it would

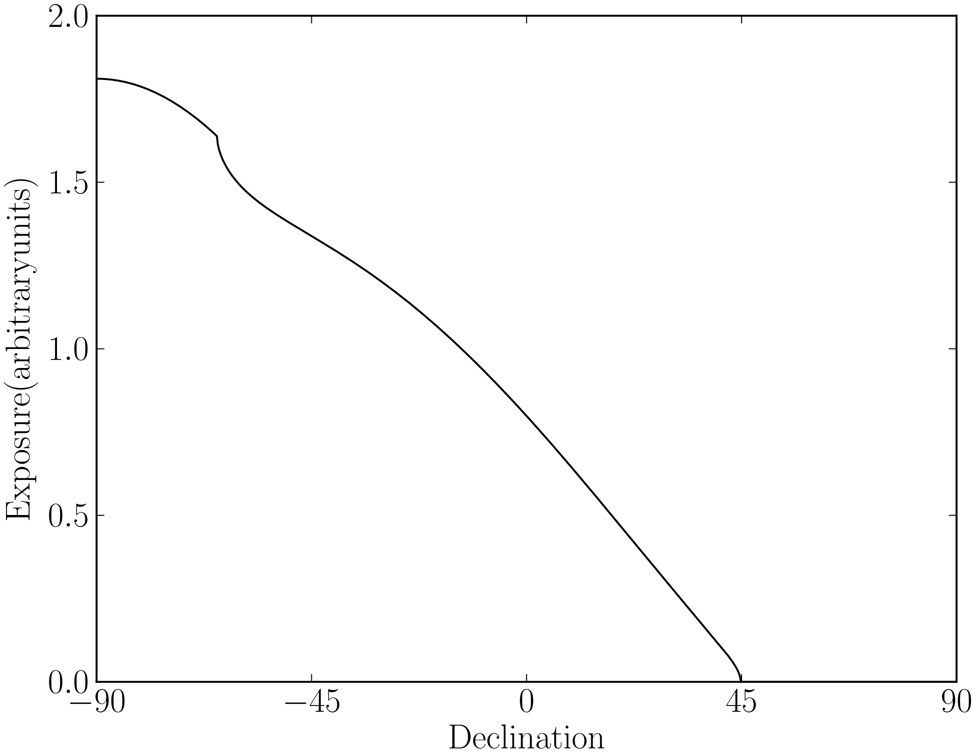

Figure 9.1: Auger's exposure function normalized to $\int \omega(\Omega)d\Omega = 4\pi$. Note that the exposure is exactly zero for declinations 45° and above.

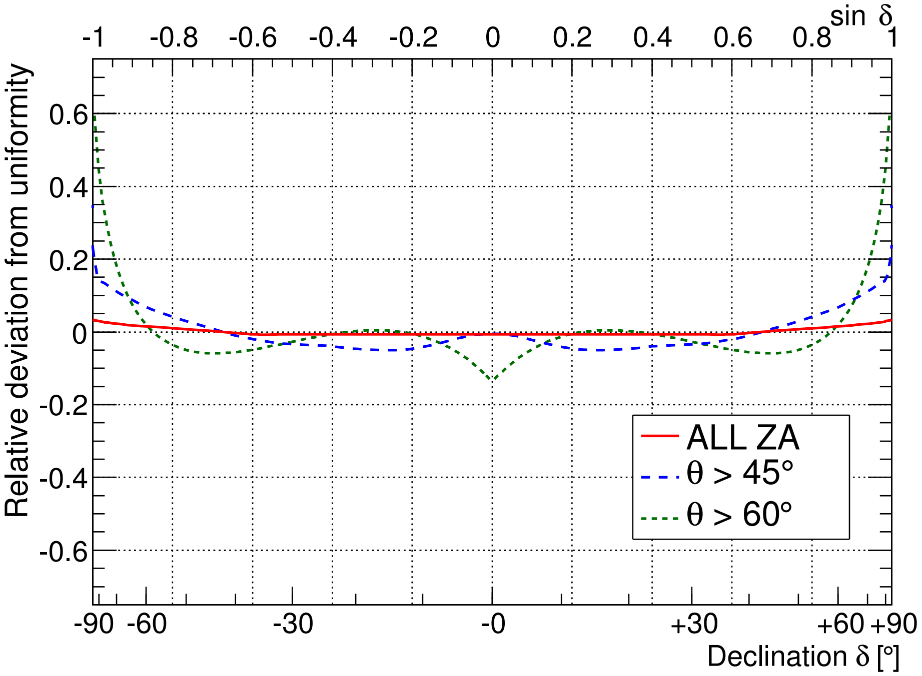

Figure 9.2: EUSO's exposure plotted as a function of declination and maximum zenith angle. The vertical axis shows a deviation from uniformity [11].

collect up to 1000 cosmic ray events at and above 55 EeV (1 EeV = 10^{18} eV) over a 5 year lifetime, surpassing the reach of any ground based project.

It must be emphasized that because previous data from ground based experiments were so sparse at energies which would be accessible to EUSO, upper limits on anisotropy were necessarily restricted to energies below the threshold of EUSO. EUSO expects many more events at $\sim 10^{20}$ eV, allowing an enhanced anisotropy reach. In addition, EUSO would observe more events with a higher rigidity $\mathcal{R} = E/Z$, events less bent by magnetic fields which may be helpful in identifying point sources on the sky.

EUSO brings two new, major advantages to the search for the origins of UHECRs. One advantage is the large field of view (FOV), attainable only with a space based observatory. With a 60° opening angle for the telescope, the down pointing ("nadir") FOV is

$$\pi(h_{\rm ISS}\tan(30^\circ))^2 \approx h_{\rm ISS}^2 \approx 150,000\,{\rm km}^2\,. \tag{9.2}$$

We will compare the ability to detect large scale anisotropies at a space based, full sky experiment with that of a ground based partial sky experiment. For reference, we will use the largest ground based cosmic ray observatory, Auger [92]. Thus the proposed EUSO FOV, given in eq. 9.2, is 50 times larger for instantaneous measurements (e.g., for observing transient sources). Multiplying the proposed EUSO FOV by an expected 18% duty cycle, yields a time averaged nine fold increase in acceptance for the EUSO design compared to Auger, at energies where the EUSO efficiency has peaked (at and above $\gtrsim 50-100$ EeV). Tilting the telescope turns the circular FOV given in eq. 9.2 into a larger elliptical FOV. The price paid for "tilt mode" is an increase in the threshold energy of the experiment.

The second advantage of a space based experiment over a ground based one is the coverage of the full sky (4π steradians) with nearly constant exposure and consistent systematic errors on the energy and angle resolution, again attainable only with a space based observatory. This part compares full sky studies of possible anisotropies to partial sky studies. The reach benefits from the 4π sky coverage, but also from the increased statistics resulting from the greater FOV.

9.3 Event Rates

The 231 event sample published by Auger over 9.25 years of recording cosmic rays at and above ~ 52 EeV [69] allows us to estimate the flux at these energies. The annual rate of such events at Auger is $\sim 231/9.25 = 25$. For simplicity, we consider a 250 event sample for Auger, as might be collected over a full decade.

Including the suppressed efficiency of EUSO down to ~ 55 EeV reduces the factor of 9 relative to Auger down to a factor $\sim$6 for energies at and above 55 EeV. We arrive at the 450 event sample as the EUSO expectation at and above 55 EeV after three years running in nadir mode (or, as is under discussion, in tilt mode with an increased aperture but a reduced number of photons). A 750 event sample is then expected for five years of EUSO running in a combination of nadir and tilt mode. Finally, the event rate at an energy measured by TA is known to significantly exceed that of Auger. This leads to a five year event rate at EUSO of about 1000 events. Thus, we consider the motivated data samples of 250, 450, 750, and 1000 events in the simulations that follow.

Chapter 10

Tools for Anisotropy Searches

10.1 Spherical harmonics

The real spatial event distribution, $I(\Omega)$, normalized to $\int d\Omega I(\Omega) = 1$, can be expressed as the sum of spherical harmonics,

$$I(\Omega) = \sum_{\ell=0}^{\infty} \sum_{|m| \leq \ell} a_\ell^m Y_\ell^m(\Omega)\,, \tag{10.1}$$

where Ω denotes the solid angle parameterized by the pair of zenith (θ) and azimuthal (ϕ) angles. The Y_ℓ^m's are the angular part of the solution to Laplace's equation in spherical coordinates. They can be enumerated as

$$Y_{\ell m}(\theta, \phi) = (-1)^m \sqrt{\frac{2\ell+1}{4\pi} \frac{(\ell-m)!}{(\ell+m)!}} P_m^\ell(x) e^{im\phi}\,, \tag{10.2}$$

where P_m^ℓ is the associated Legendre polynomial. The set $\{Y_\ell^m\}$ is complete, and so the expansion eq. 10.1 is unique. Besides being complete, the set $\{Y_\ell^m\}$ is also orthonormal, with orthonormality condition

$$\int d\Omega Y_{\ell_1}^{m_1}(\Omega) Y_{\ell_2}^{m_2 *}(\Omega) = \delta_{\ell_1 \ell_2} \delta_{m_1 m_2}\,. \tag{10.3}$$

The asterisk denotes complex conjugation of the spherical harmonic; the complex Y_ℓ^m's satisfy the relation $Y_\ell^{m*} = (-1)^m Y_\ell^{-m}$. Since the Y_ℓ^0 are real, so are the a_ℓ^0, while those with $m \neq 0$ are, in general, complex. The a_ℓ^m coefficients contain all the information about the flux distribution. Inversion of eq. 10.1 gives the coefficients

$$a_\ell^m = \int d\Omega\, Y_\ell^{m*}(\Omega)\, I(\Omega)\,. \tag{10.4}$$

This relation makes it clear that a_ℓ^0 is real (since Y_ℓ^0 is real), and that a_ℓ^m, $m \neq 0$, is complex (because Y_ℓ^m, $m \neq 0$, is complex).

In practice the observed flux is the sum of Dirac delta functions,

$$\bar{I}(\Omega) = \frac{1}{N} \sum_{i=1}^{N} \delta(\mathbf{u}_i, \Omega)\,, \tag{10.5}$$

where $\{\mathbf{u}_i\}_{i=1}^N$ is the set of N directions of cosmic rays and the Dirac delta function is defined on the sphere in the usual fashion,

$$\int f(\mathbf{u}) \delta(\mathbf{u}, \mathbf{v}) d\mathbf{u} = f(\mathbf{v})\,, \tag{10.6}$$

for some function on the sphere f. This allows us to estimate the coefficients in eq. 10.4 as

$$\bar{a}_\ell^m = \frac{1}{N} \sum_{i=1}^{N} Y_\ell^{m*}(\mathbf{u}_i)\,, \tag{10.7}$$

where $\mathbf{u}_i$ is the unit direction vector to the ith cosmic ray, $1 \leq i \leq N$. $\bar{a}_\ell^m$ converges to the actual a_ℓ^m as $N \to \infty$.

The lowest multipole is the $\ell = 0$ monopole term which contains no anisotropy information. The normalization of the all sky event distribution to unity fixes the value $a_0^0 = \frac{1}{\sqrt{4\pi}}$. Guaranteed by the orthogonality of the Y_ℓ^m's, the higher multipoles (i.e., $\ell \geq 1$) when integrated over the whole sky equate to zero. Their coefficients a_ℓ^m, when nonzero, correspond to anisotropies.

10.1.1 Dipole Overview

Dipoles excite the specific spherical harmonics corresponding to Y_1^m, with the three Y_1^m's proportional to $\hat{\mathbf{x}}$, $\hat{\mathbf{y}}$, and $\hat{\mathbf{z}}$. A dipolar distribution is theoretically motivated by a single point source producing the majority of UHECRs whose trajectories are subsequently smeared by galactic and extragalactic magnetic fields.

With full sky coverage it is straightforward to reconstruct the dipole moment so long as the exposure function is always nonzero (and possibly nonuniform). For the full sky case (EUSO), we use the description presented in §11.1.1, which even allows for a nonuniform exposure, provided that the flux does not become too close to zero anywhere on the sky.

Reconstructing any anisotropy, including the dipole, with partial sky exposure is challenging. One approach for dipole reconstruction is that presented in §11.2.1. We refer to this approach as the AP method. We note that continuing the AP approach becomes very cumbersome for reconstructing the quadrupole and higher multipoles. Another approach for reconstructing any Y_ℓ^m with partial coverage is presented in §11.2.2, which we refer to as the K-matrix approach. A comparison of these approaches is presented in §11.2.3

10.1.2 Quadrupole Overview

The physically motivated quadrupoles are characterized by the spherical harmonics corresponding to $Y_2^0 \propto 3z^2 - 1$. Y_2^0 represents an anisotropy that is maximal along the equator and minimal along the poles (or, depending on the sign of a_2^0, the opposite). Such a distribution is motivated by the presence of many sources distributed along a plane, such as is the case with the supergalactic plane. As a real, physical example of a well known source distribution distributed with a quadrupole contribution, we calculate the power spectrum, C_ℓ, (defined in eq. 10.8 which quantifies the the anisotropy of a distribution at each ℓ) as might be seen at the Earth for the 2MRS catalog of the closest 5310 galaxies above a minimum intrinsic brightness [12]. The catalog contains redshift information and contains all galaxies above a minimum intrinsic brightness out to $z = 0.028 \sim 120$ Mpc. As such, it is reasonable to suppose that UHECRs come from these galaxies and, for simplicity, we implement uniform flux from each galaxy.

In the left panel of fig. 10.1 we show the power spectrum that results for the known physical locations of these galaxies. In the right panel we show the power spectrum that results when each galaxy is weighted by the number of events expected from it, i.e., by the inverse square of the distance to the galaxy, a $1/d^2$ weighting. We remark that for the closest ~ 200 galaxies, the distance to each galaxy is known better from the direct "cosmic distance ladder" approach than it is from the redshift, and we use these direct distances. For the farther galaxies, direct distances are less reliable, and we use the redshift inferred distances. In this way, we also avoid any (possibly large) peculiar velocity contributions to the redshifts of the nearer galaxies.

It is instructive to compare the two panels. Without the $1/d^2$ weighting (left panel), the intrinsic quadrupole nature of the distribution of 2MRS galaxies dominates the power spectrum; C_2 exceeds the other C_ℓ's in the panel by a factor of $\gtrsim 5$. In the right panel, galaxies are weighted by their

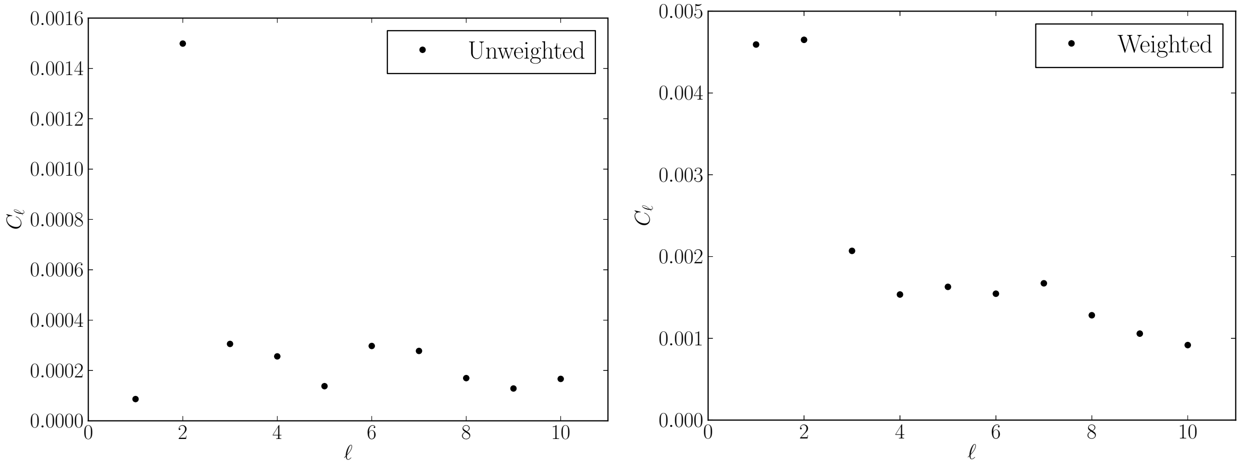

Figure 10.1: The power spectrum (see eq. 10.8) for nearby galaxies out to $z = 0.028$ (to $d = 120$ Mpc) based on their positions (left panel), and weighted according to $1/d^2$ (right panel). The 2MRS catalog [12] includes a cut on Milky Way latitudes $|b| < 10^\circ$ which is accounted for in the calculation of the power spectrum, see appendix B. C_2 is large because the galaxies roughly form a planar (quadrupolar) structure; C_1 in the right panel is large because we are not in the center of the super cluster, thereby inducing a dipole contribution. (The relative scale between the ordinates of the two figures carries no information.)

apparent fluxes so the closest galaxies dominate. The large dipole is due to the proximity of Cen A, and the fact that the next closest galaxy, M87, is ~ 4 times farther from the Earth. When determinations of the C_ℓ's are made, it is likely to be the dipole and quadrupole that will first emerge from the data based on the distributions of nearby galaxies. This quantifiably motivates our choice made in this part to examine the dipole and quadrupole anisotropies. While the actual distribution is likely a combination of dipole and quadrupole components, throughout this part we consider the simpler cases where the distribution of sources has either a pure dipole anisotropy or a pure quadrupole anisotropy.

The quadrupole distribution that will be considered in this part is of the form $I(\Omega) \propto 1 - B\cos^2\theta$ for $0 \leq B \leq 1$, aligned with a particular quadrupole axis where θ is the angle between the axis and Ω. The quadrupolar distribution is a linear combination of the monopole term Y_0^0 and Y_2^0 oriented along the quadrupole axis. The distribution has two minima at opposite ends of the quadrupole axis and a maximum in the plane perpendicular to this axis. The quadrupolar data and the reconstruction of the quadrupole axis are shown in the lower panel of fig. 10.3.

For the full sky case, we will use the method outlined by Sommers in [87] and §11.1.2 to reconstruct the quadrupole amplitude and axis. As discussed in chapter 12, it is possible to accurately reconstruct the quadrupole moment for experiments with partial sky exposure at particular latitudes, independently of their exposure function. This is because there is very little quadrupole moment in the exposure function. By some chance, Auger is exactly at the optimal latitude in the southern hemisphere, and TA is very close to the optimal latitude in the northern hemisphere. Therefore we can use Sommers's technique for quadrupole reconstruction of both full sky EUSO and partial sky Auger.

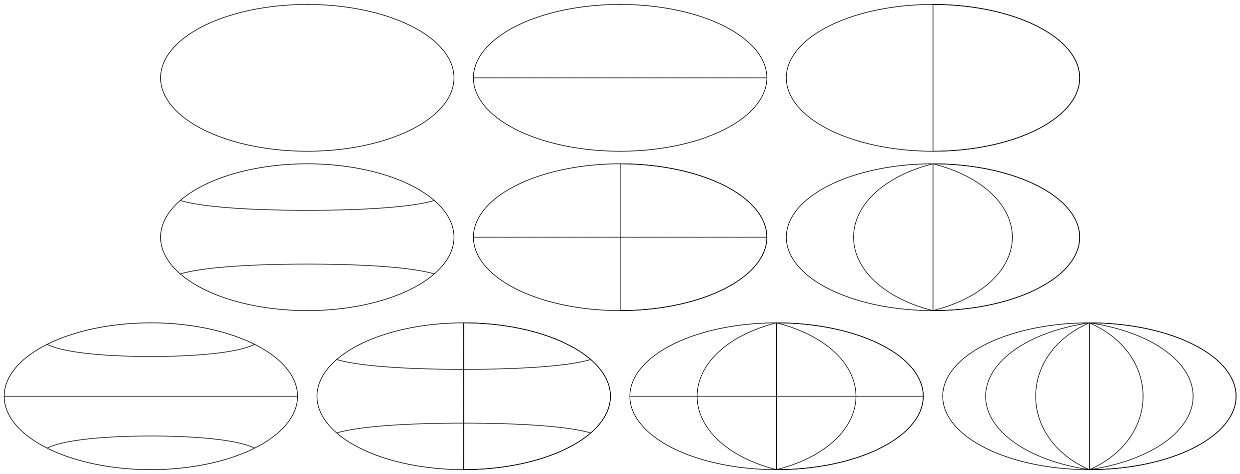

Figure 10.2: Nodal lines separating excess and deficit regions of sky for various (ℓ, m) pairs. The top row shows the $(0, 0)$ monopole, and the partition of the sky into two dipoles, $(1, 0)$ and $(1, 1)$. The middle row shows the quadrupoles $(2, 0)$, $(2, 1)$, and $(2, 2)$. The bottom row shows the $\ell = 3$ partitions, $(3, 0)$, $(3, 1)$, $(3, 2)$, and $(3, 3)$.

10.2 Power Spectrum

The power spectrum is defined as

$$C_\ell \equiv \frac{1}{2\ell+1} \sum_{m=-\ell}^{\ell} |a_\ell^m|^2 , \tag{10.8}$$

The following subsections discuss various properties of the power spectrum.

10.2.1 Nodal Lines

A Y_ℓ^m with a nonzero m corresponds to $2\,|m|$ longitudinal "slices" ($|m|$ nodal meridians) on the sky. There are $\ell - |m| + 1$ latitudinal "zones" ($\ell - |m|$ nodal latitudes). In fig. 10.2 we show the partitioning described by some low multipole moments. Useful visualizations of spherical harmonics can also be found in [93]. The configurations with $(\ell, -|m|)$ are related to those with $(\ell, +|m|)$ by a longitudinal phase advance $\phi \Rightarrow \phi + \frac{\pi}{2}$, or $\cos\phi \Rightarrow \sin\phi$.

A simple approximation for the number of cosmic rays necessary to resolve power at a particular level is to count the number $N_Z(\ell, m)$ of nodal zones in each Y_ℓ^m. Each Y_ℓ^m has

$$N_Z(\ell, m) = \begin{cases} \ell + 1 & m = 0 \\ 2|m|(\ell - |m| + 1) & m \neq 0 \end{cases} , \tag{10.9}$$

nodal zones. The average over m of the number nodal zones at a given ℓ is,

$$\langle N_Z(\ell) \rangle = \frac{\ell+1}{3(2\ell+1)}(2\ell^2 + 4\ell + 3) . \tag{10.10}$$

For low values of ℓ, this returns the obvious results,

$$\langle N_Z(\ell = 0) \rangle = 1 , \quad \langle N_Z(\ell = 1) \rangle = 2 . \tag{10.11}$$

For large ℓ,

$$\langle N_Z(\ell)\rangle \to \frac{\ell^2}{3}\,. \tag{10.12}$$

If we make the simple assumption of requiring $\mathcal{O}(1)$ event per nodal zone to resolve a particular term in the power spectrum, then, for large ℓ we require $\sim \ell^2/3$ events to resolve C_ℓ. Thus, the rule of thumb is that our EUSO fiducial samples of 450, 750, and 1000 events can resolve the C_ℓ's up to an ℓ value of the mid 30's, mid 40's, and mid 50's, respectively, i.e., (using $\theta \sim \frac{90^\circ}{\ell}$) can resolve structures on the sky down to $2-3^\circ$. A ground based observatory, due to having fewer events and no full sky coverage, would do much worse. We note that the statistical error in angle estimated here for EUSO event numbers is well matched to the expected systematic angular resolution error $\sim 1^\circ$ of EUSO.

10.2.2 Proof of the Rotational Invariance of the Power Spectrum

While calculating the coefficients of the spherical harmonics, the a_ℓ^m's, is useful, the a_ℓ^m's suffer the disadvantage that they are frame dependent. The spherical harmonics coefficients, the a_ℓ^m's given in eq. 10.1, are clearly coordinate dependent, as a simple rotation in the ϕ coordinate will change the $e^{im\phi}$ part of the spherical harmonic for $m \neq 0$, and a rotation in the θ coordinate will change the associated Legendre polynomial part $P_\ell^m(\theta)$ for $\ell \neq 0$. So only the $\ell = m = 0$ monopole coefficient is coordinate independent.

To combat this problem of rotational noninvariance of the spherical harmonic coefficients, we turn to the power spectrum, defined in eq. 10.8. While it may be intuitive that the C_ℓ should be rotationally (coordinate) invariant, this attribute is not obvious. The purpose of this subsection is to prove the rotational invariance of the power spectrum.

For a discrete set of sources, the normalized intensity function is given by eq. 10.5. In terms of spherical harmonics, one finds that the spherical harmonic coefficients are given by eq. 10.7 where $\mathbf{u}_i$ is the unit direction vector to the ith cosmic ray, $1 \le i \le N$.

To construct the estimation of the associated power spectrum, we square these a_ℓ^m's followed by a sum over m:

$$\begin{aligned}\bar{C}_\ell &\equiv \frac{1}{2\ell+1}\sum_{|m|\le\ell}|\bar{a}_\ell^m|^2 \\ &= \frac{1}{N^2(2\ell+1)}\sum_{|m|\le\ell}\left|\sum_{i=1}^{N} Y_\ell^{m*}(\mathbf{u}_i)\right|^2 .\end{aligned} \tag{10.13}$$

Since the sums are finite they may be rearranged and expanded to

$$\bar{C}_\ell = \frac{1}{N^2(2\ell+1)}\sum_{i=1}^{N}\sum_{|m|\le\ell}|Y_\ell^m(\mathbf{u}_i)|^2 + +\frac{2}{N^2(2\ell+1)}\sum_{i<j}\sum_{|m|\le\ell}Y_\ell^{m*}(\mathbf{u}_i)Y_\ell^m(\mathbf{u}_j)\,. \tag{10.14}$$

The addition formula [94] for spherical harmonics is

$$P_\ell(\mathbf{x}\cdot\mathbf{y}) = \frac{4\pi}{2\ell+1}\sum_{|m|\le\ell}Y_\ell^{m*}(\mathbf{x})Y_\ell^m(\mathbf{y})\,, \tag{10.15}$$

where $P_\ell(\cos\theta)$ is the Legendre polynomial. Since $P_\ell(1) = 1$, setting the unit direction vectors $\mathbf{x}$ and $\mathbf{y}$ to be equal in eq. 10.15, one gets

$$\frac{2\ell+1}{4\pi} = \sum_{|m|\le\ell}|Y_\ell^m(\mathbf{x})|^2\,. \tag{10.16}$$

Combining eqs. 10.14, 10.15, and 10.16 gives

$$\bar{C}_\ell = \frac{1}{4\pi N} + \frac{1}{2\pi N^2} \sum_{i<j} P_\ell(\mathbf{u}_i \cdot \mathbf{u}_j)\,. \tag{10.17}$$

Experimentally only $\bar{a}_\ell^m$ and $\bar{C}_\ell$ may be measured, but these are estimates of their continuous counterparts a_ℓ^m, C_ℓ respectively. Finally, since inner products are invariant under rotations, the C_ℓ are also invariant under rotations. This completes the proof.

10.3 Anisotropy Measure

Commonly, a major component of the anisotropy is defined via a max/min directional asymmetry,

$$\alpha \equiv \frac{I_{\max} - I_{\min}}{I_{\max} + I_{\min}} \in [0, 1]\,. \tag{10.18}$$

A dipole (plus monopole) distribution is defined by a dipole axis and an intensity map given by

$$I(\Omega) \propto 1 + A\cos\theta\,, \tag{10.19}$$

where θ is the angle between the direction of observation, denoted by Ω, and the dipole axis. This form contains a linear combination of the Y_1^m's. In particular, a monopole term is required to keep the intensity map positive definite. One readily finds that the anisotropy due to a dipole is simply $\alpha_D = A$.

A quadrupole distribution (with a monopole term but without a dipole term) is similarly defined, as

$$I(\Omega) \propto 1 - B\cos^2\theta\,. \tag{10.20}$$

In the frame where the $\hat{\mathbf{z}}$ axis is aligned with the quadrupole axis, the quadrupole contribution is composed of just the Y_2^0 term. In any other frame, this Y_2^0 is then related to all the Y_2^m's, by the constraint of rotational invariance of the C_ℓ's mentioned above. In any frame, one finds that the anisotropy measure is

$$\alpha_Q = \frac{B}{2 - B}\,, \tag{10.21}$$

and the inverse result is

$$B = \frac{2\alpha}{1 + \alpha}\,. \tag{10.22}$$

An advantage of using a spherical harmonic based approach to anisotropy is that it is model independent. See [95] for a discussion of anisotropies as seen by full sky experiments for two different source models.

Sample sky maps of dipole and quadrupole distributions are shown in fig. 10.3 for both full sky acceptance and for Auger's acceptance, along with the actual and reconstructed symmetry axes.

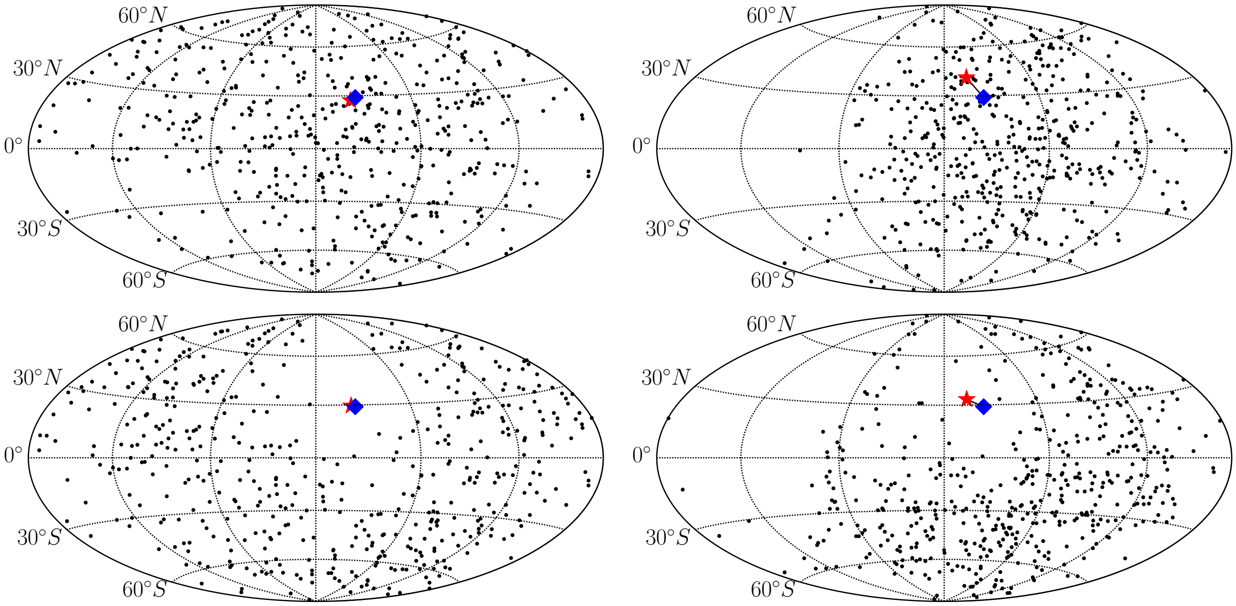

Figure 10.3: Shown are sample sky maps of 500 cosmic rays. The top row corresponds to the $\alpha_{D,\mathrm{true}} = 1$ dipole, while the bottom row corresponds to the $\alpha_{Q,\mathrm{true}} = 1$ quadrupole distribution. The left and right panels correspond to all sky, space based and partial sky, ground based coverage, respectively. The injected dipole or quadrupole axis is shown as a blue diamond, and the reconstructed direction is shown as a red star. We see that reconstruction of the multipole direction with an event number of 500 is excellent for an all sky observatory (left panels) and quite good for partial sky Auger (right panels). In practice, α_D and α_Q are likely much less than unity, and the event rate for all sky EUSO is expected to be ~ 9 times that of Auger. Both effects on the comparison of Auger and EUSO are shown in figs. 14.1 and 14.2.

Chapter 11

Reconstructing Anisotropies

Detecting any deviation from isotropy in UHECRs has been a long sought after goal. For example, at high energies above the GZK suppression, the anisotropies are expected to reveal the distribution of cosmic ray sources among nearby galaxies. One common approach for measuring anisotropies is to partition the sky into regions of various sizes with the use of spherical harmonics. The low order spherical harmonics correspond to simple structures. The lowest nontrivial order, $\ell = 1$, called the dipole, may correspond to a single source where the cosmic rays have been smeared out by magnetic fields during propagation. The next order, $\ell = 2$, called the quadrupole, can correspond to a planar distribution of sources, such as might be the case if the sources are spread across the galactic or supergalactic plane. Unfortunately partial sky experiments cannot, in principle, distinguish between dipoles and quadrupoles. For example, Auger would see a dipole with a maximum towards the north pole as a band of maxima along the equator and would be indistinguishable from a planar quadrupole with the same axis.

11.1 Full Sky Coverage

Reconstructing the spherical harmonics in general, including the quadrupole anisotropy magnitude arising from a planar distribution of sources, is straightforward with full sky (even nonuniform) coverage. In this section we will explain the standard approaches in the literature for reconstructing the $\ell = 1, 2$ spherical harmonics with full sky coverage. We also present a new approach for reconstructing a quadrupole with either full or partial sky coverage that is more transparent than the standard approach.

11.1.1 Sommers's Approach for Dipoles

P. Sommers presented a straightforward approach to reconstruct dipolar anisotropies with full sky coverage but possibly nonuniform exposure, hereafter referred to as Sommers's approach [87]. Given N events at directions $\hat{\mathbf{u}}^{(i)}$ with relative exposures ω_i at each event, under the assumption that ω is zero nowhere on the sphere, the dipole anisotropy magnitude and direction is given simply by

$$\alpha_D D_a = \frac{3}{\mathcal{N}} \sum_{i=1}^{N} \frac{1}{\omega_i} u_a^{(i)} \,, \tag{11.1}$$

where $i \in \{x, y, z\}$, $\hat{\mathbf{D}}$ is the unit vector in the dipole direction, and

$$\mathcal{N} = \sum_{i=1}^{N} \frac{1}{\omega_i} \,, \tag{11.2}$$

is the appropriate normalization factor given the relative exposure.

11.1.2 Sommers's Approach for Quadrupoles

P. Sommers also presented an approach to reconstruct quadrupolar anisotropies with full sky coverage but possibly nonuniform exposure, hereafter referred to as Sommers's approach [87]. He presents his quadrupolar matrix,

$$S_{ab} = \int I(\Omega) u_a u_b d\Omega\,, \tag{11.3}$$

with $a, b \in \{x, y, z\}$, so u_a is a particular component of $\mathbf{u}$. For discrete sources, this can be estimated in the typical fashion,

$$S_{ab} = \frac{1}{\mathcal{N}} \sum_{i=1}^{N} \frac{1}{\omega(\mathbf{u}_i)} u_a^{(i)} u_b^{(i)}\,, \tag{11.4}$$

with $\mathcal{N}$ given by eq. 11.2. Then, for $\lambda_1 < \lambda_2 < \lambda_3$ the eigenvalues of S,

$$\Delta = \frac{\lambda_2 + \lambda_3}{2} - \lambda_1\,, \qquad \xi = \frac{2 - 10\Delta}{2 + 5\Delta}\,. \tag{11.5}$$

Finally, the anisotropy from a quadrupolar distribution is given by,

$$\alpha_Q = \frac{1 - \xi}{1 + \xi}\,. \tag{11.6}$$

11.1.3 New Approach for Quadrupoles

Sommers outlines one method for calculating the anisotropy from a pure quadrupolar distribution [87] as discussed in §11.1.2. His approach assumes full sky (possibly nonuniform) exposure. Based on the results from chapter 12, that same approach can be applied for Auger and TA by ignoring their exposure.

Since the power spectrum is rotationally invariant as shown in §10.2.2, we can consider a new alternate derivation of the quadrupole strength. Begin by choosing a coordinate frame that aligns the z-axis with the symmetry axis of the quadrupole. Then only a_0^0 and a_2^0 are nonzero.

In terms of Cartesian coordinates,

$$Y_2^0 = A(3z^2 - 1)\,, \tag{11.7}$$

with $A = \frac{1}{4}\sqrt{\frac{5}{\pi}}$. The intensity function in Cartesian coordinates aligned with the quadrupole axis is

$$I = B(1 - Cz^2)\,, \tag{11.8}$$

where the normalization requirement sets $\frac{1}{B} = 4\pi(1 - \frac{C}{3})$. We then invert eq. 11.7 to write the intensity as a function of Y_0^0 and Y_2^0.

$$I = \frac{1}{\sqrt{4\pi}} Y_0^0 - \frac{BC}{3A} Y_2^0\,. \tag{11.9}$$

In the coordinate frame where the quadrupole symmetry axis is aligned with the z axis, only a_0^0 and a_2^0 are nonzero and are given by eq. 11.9. Then $a_2^0 = -\sqrt{5C_2}$ where we used the definition of the power spectrum from eq. 10.8 and the sign is because a_2^0 in eq. 11.9 is negative definite. This form is reminiscient of some aspects of that presented by Sommers in §11.1.2.

Then we have a new prescription to find α_Q as defined in eq. 10.18. First calculate the power spectrum for $\ell = 2$ in any coordinate frame for data with either full sky coverage or from experiments at latitudes $30^\circ \lesssim |a_0| \lesssim 40^\circ$ (see chapter 12 for further discussion on reconstructing quadrupoles with partial sky exposure). Then get a_2^0 and then find C as described in eq. 11.9 and this gives α_Q from eq. 12.21.

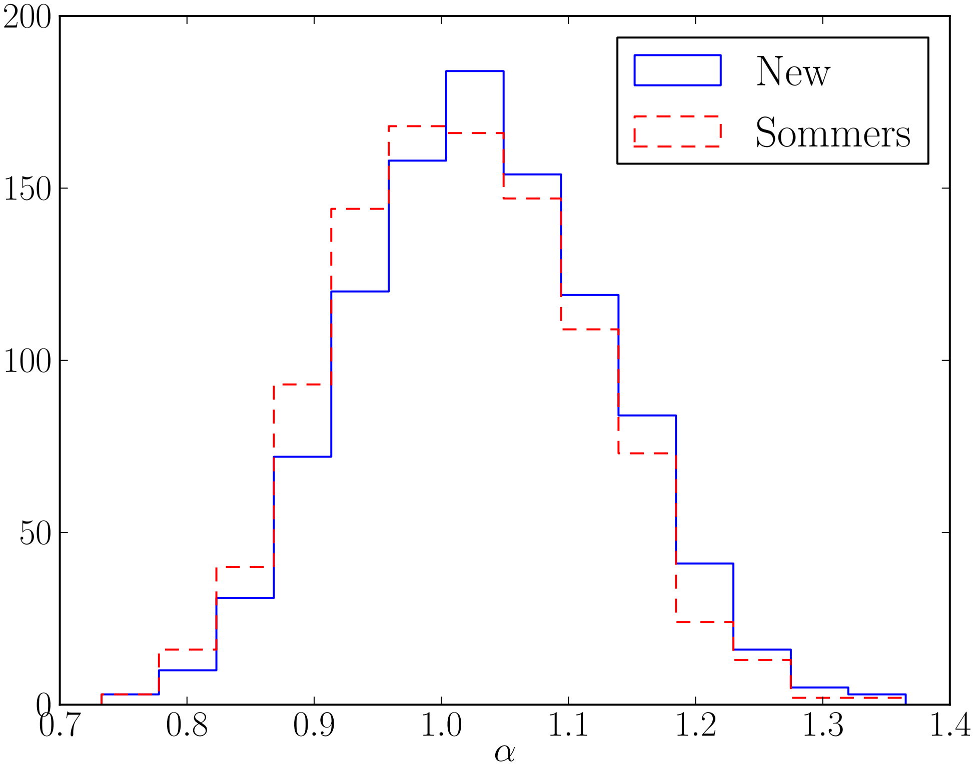

Figure 11.1: 500 directions were simulated with a quadrupolar distribution aligned in a random direction, and with Auger's exposure. Here, α_Q is set to unity. The quadrupole strength was then reconstructed with each of the two techniques. This process was repeated 1000 times. Both approaches are correlated - that is when one approach gives a small value of α, the other will as well.

We compare this approach to that described by Sommers in [87]. We note that this new technique does not provide directional information, which is available in the eigenvectors of the Q tensor as described by Sommers. A plot of the comparison is shown in fig. 11.1 of the reconstructed quadrupole amplitude. The results are consistent with each other. In particular, the means and standard deviation for each approach are 1.033 ± 0.099 for this new approach and 1.017 ± 0.098 for Sommers's approach, compared to a correct value of 1. The nonnegligible deviations in the reconstructed values are not due to the small corrections mentioned in eq. 12.19, rather they are due to the fact that a discrete sampling with finite N number of delta functions of a continuous distribution tends to lend itself to larger anisotropies. Nonetheless, this approach has value due to its straightforward derivation from the power spectrum.

11.2 Partial Sky Coverage

Reconstructing spherical harmonics with partial sky coverage complicates things dramatically compared to the full sky case. While the techniques in the literature for dealing with the dipole on partial sky coverage are fairly simple, those for a quadrupole are not [75, 96, 97]. In this section we present two approaches for reconstructing dipoles with partial sky coverage and a comparison of the two. We present no approach for reconstructing the quadrupole with partial sky coverage because we will show in chapter 12 that either of the full sky approaches presented can be used for partial sky due to the particular locations of the two ground based UHECR experiments.

11.2.1 AP Approach for Dipoles

J. Aublin and E. Parizot presented one approach for reconstructing dipoles with partial sky anisotropy, hereafter referred to as the AP approach [98]. We summarize the AP approach in this subsection. They made the important observation that the nonuniformity of the exposure function of ground based experiments is much less important than the regions where it is zero.

They begin by defining a number of useful intermediate variables.

$$d = \cos\theta_{\text{min}} - \cos\theta_{\text{max}}\,, \tag{11.10}$$

$$s = \cos\theta_{\text{min}} + \cos\theta_{\text{max}}\,, \tag{11.11}$$

$$p = \cos\theta_{\text{min}} \times \cos\theta_{\text{max}}\,, \tag{11.12}$$

$$\gamma = \frac{s^2 - p}{3}\,, \tag{11.13}$$

where $\theta_{\text{min}} = 90^\circ - \theta_m - a_0$ and $\theta_{\text{max}} = 90^\circ$. Next, they calculate the zeroth and first order moments of the flux.

$$I_0 = \int_{\theta_{\text{min}}}^{\theta_{\text{max}}} d\theta \sin\theta \int_0^{2\pi} d\phi \Phi(\mathbf{u})\,, \tag{11.14}$$

$$\mathbf{I} = \int_{\theta_{\text{min}}}^{\theta_{\text{max}}} d\theta \sin\theta \int_0^{2\pi} d\phi \mathbf{u}\Phi(\mathbf{u})\,. \tag{11.15}$$

From this they invert and find that the dipole magnitude and direction is given by

$$\alpha_D D_x = \frac{I_x}{sI_z - 2\gamma I_0} \frac{\gamma - p}{\gamma - 1}\,, \tag{11.16}$$

$$\alpha_D D_y = \frac{I_y}{sI_z - 2\gamma I_0} \frac{\gamma - p}{\gamma - 1}\,, \tag{11.17}$$

$$\alpha_D D_z = \frac{sI_0 - 2I_z}{sI_z - 2\gamma I_0}\,. \tag{11.18}$$

This approach provided a significant improvement over the standard at the time, which was a one dimensional Rayleigh analysis which discards all declination information [99].

11.2.2 K-matrix Approach

P. Billoir and O. Deligny present an approach to reconstruct anisotropies of any order hereafter referred to as the K-matrix approach [97]. They begin by writing down the K-matrix for a given exposure function (generally defined for ground based experiments in eq. 9.1),

$$[K]_{\ell\ell'}^{mm'} = \int d\Omega Y_\ell^m(\Omega)\omega(\Omega)Y_{\ell'}^{m'}\,. \tag{11.19}$$

This matrix describes how the exposure function ω causes the various spherical harmonics to interfere. From this the uncorrected spherical harmonic coefficients observed at a ground based experiment,

$$b_\ell^m = \int d\Omega Y_\ell^{m*}(\Omega)\omega(\Omega)I(\Omega)\,, \tag{11.20}$$

can be exactly related to the true spherical harmonic coefficients,

$$a_\ell^m = \int d\Omega Y_\ell^{m*}(\Omega)I(\Omega)\,, \tag{11.21}$$

by the relation

$$b_\ell^m = \sum_{\ell',m'} [K]_{\ell\ell'}^{mm'} a_{\ell'}^{m'}\,. \tag{11.22}$$

Of course, we are interested in turning uncorrected coefficients into true coefficients which involves inverting an infinite matrix. To this end, an $\ell_{\rm max}$ must be introduced to truncate the matrix. This approach is completely generalizable to calculate any ℓ. Once the estimate of the true coefficients are acquired, the anisotropy measure can be calculated using either Sommers's approach for full sky discussed in §11.1.1 for dipoles or the new approach presented in §11.1.3 for quadrupoles, although we will show in chapter 12 that the K-matrix step can be skipped for partial sky experiments with certain experimental parameters, which both Auger and TA satisfy when they are measuring quadrupoles. A numerical comparison of this approach applied to reconstructing dipoles and the AP approach presented in §11.2.1 is presented in §11.2.3.

11.2.3 Comparison of Partial Sky Dipole Approaches

§11.2.1 and §11.2.2 present the AP and K-matrix approaches, respectively, for reconstructing dipoles measured at a ground based partial sky experiment. We compare these two approaches to determine which optimally reconstructs a given dipole distribution. Our result is most clearly presented in fig. 11.2. We consider 500 cosmic rays with a dipole distribution of magnitude $\alpha_{D,\rm true} = 1$

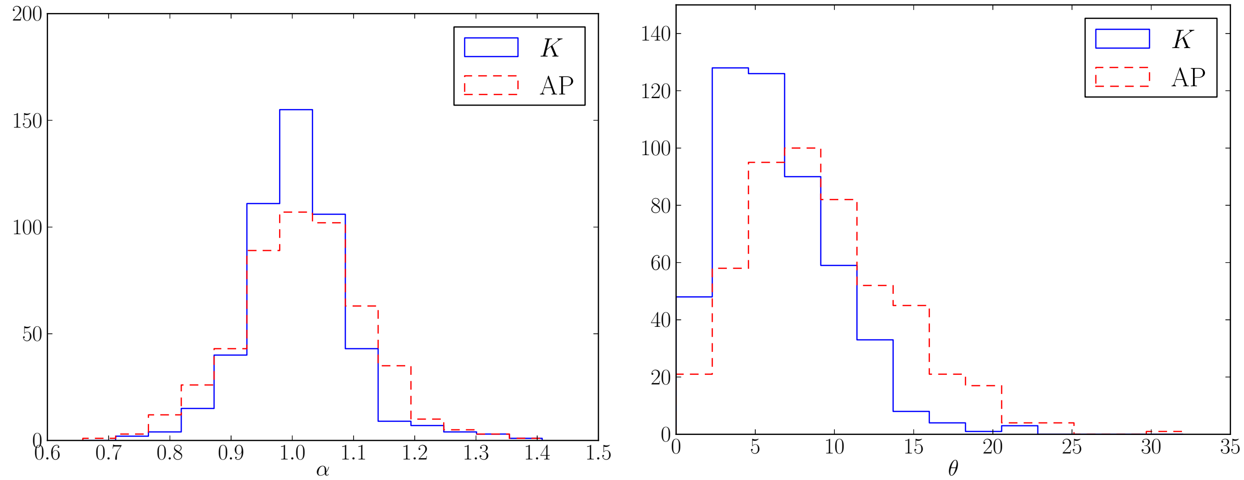

Figure 11.2: We simulated 500 cosmic rays with a dipole of amplitude of $\alpha_{D,\text{true}} = 1$ pointing in a random direction, and with the Auger exposure. Then we reconstructed both the direction and the dipole amplitude 500 times with both reconstruction techniques (AP and K-matrix). In the left panel we show a histogram of the reconstructed values of $\alpha_{D,\text{true}}$, and in the right panel the angle (in degrees) between the correct dipole direction and the reconstructed direction.

oriented in a random direction. Using Auger's exposure map, we then reconstruct the strength of the dipole using each method. This entire process was repeated 500 times. The reconstructed values of α_D are $\alpha_{D,\text{rec}} = 1.017 \pm 0.104$ and $\alpha_{D,\text{rec}} = 1.009 \pm 0.084$ for the AP and K-matrix approaches, respectively, where the uncertainty is one standard deviation. The mean angles between the actual dipole direction and the reconstructed dipole direction are $\theta = 9.25^\circ$ and $\theta = 6.41^\circ$ for the AP and K-matrix approaches respectively. The the results of the two approaches are comparable. Since the K-matrix approach does slightly better than the AP method, we will use the K-matrix approach for partial sky dipole reconstructions in what follows.

Chapter 12

Reconstructing Quadrupoles at the With Partial Sky Coverage

In this chapter we present a new formalism for reconstructing anisotropies. This formalism has some similarities to the K-matrix approach presented in §11.2.2, but it allows for experiments to take advantage of terms that may happen to be zero.

The result of this chapter is two fold. The first is that exposure function of Auger (and, to a lesser extent, TA) has no quadrupole component. The next is that this fact is enough to reconstruct a quadrupole with a partial sky experiment with essentially the same accuracy of a full sky experiment. These claims will be derived analytically in this chapter and verified numerically in chapter 14.

12.1 Square Brackets

We will continue to use the notation presented in §11.2.2, where the b_ℓ^m are the uncorrected coefficients observed at earth, and $\bar{a}_\ell^m, \bar{b}_\ell^m$ are the approximate coefficients from the sum of discrete sources that approximates the true flux.

Instead of writing down an infinite matrix to relate a_ℓ^m, b_ℓ^m, we take a different approach. We first expand the exposure function in spherical harmonics,

$$\omega(\Omega) = \sum_{\ell=0}^{\infty} \sum_{|m|\leq\ell} c_\ell^m Y_\ell^m(\Omega)\,, \tag{12.1}$$

where the c_ℓ^m coefficients can be calculated by

$$c_\ell^m = \int d\Omega Y_\ell^{m*}(\Omega)\omega(\Omega)\,. \tag{12.2}$$

Again, the c_ℓ^0's are real and the c_ℓ^m's, $m \neq 0$, are complex. From the normalization of the exposure function given above, we infer that $c_0^0 = 4\pi Y_0^0 = \sqrt{4\pi}$. The key ingredient of this chapter will be the claim that the c_2^0 coefficient, the amount of quadrupole in the Auger and TA exposure functions, is nearly zero (and so can be neglected). Furthermore, the normalization choice on the directly inferred event distribution implies that $\sum_{\ell,m}(a_\ell^{m*}c_\ell^m) = 1$ where $\sum_{\ell,m}$ is shorthand for $\sum_{\ell=0}^{\infty}\sum_{m=-\ell}^{m=+\ell}$ (or in a related notation, for $\sum_{\ell=0}^{\infty}\sum_{|m|\leq\ell}$). Since we have seen that a_0^0 and c_0^0 are real with a product equal to unity, this constraint may be written as $\sum_{\ell\geq1,m}(a_\ell^{m*}c_\ell^m) = 0$.

We pause here to collect the inferences of our normalization choices. The a_ℓ^0, b_ℓ^0, and c_ℓ^0's are real. The a_ℓ^m, b_ℓ^m, and c_ℓ^m's with $m \neq 0$ are complex. In addition, the monopole coefficients are fixed to be $a_0^0 = b_0^0 = \frac{1}{\sqrt{4\pi}}$ and $c_0^0 = \sqrt{4\pi}$. The sum $\sum_{\ell\geq1,m}(a_\ell^{m*}c_\ell^m)$ is zero. We also recall the definitions of the various coefficients:

$$\begin{aligned} a_\ell^m &\quad\Rightarrow\quad \text{Nature's true distribution,} \\ b_\ell^m &\quad\Rightarrow\quad \text{seen by a partial sky experiment,} \\ c_\ell^m &\quad\Rightarrow\quad \text{the partial sky exposure function.} \end{aligned}$$

Inserting eqs. 10.1 and 12.1 into eq. 11.20 yields

$$b_\ell^m = (-1)^m \sum_{\ell_1,m_1} \sum_{\ell_2,m_2} a_{\ell_1}^{m_1} c_{\ell_2}^{m_2} \begin{bmatrix} \ell_1 & \ell_2 & \ell \\ m_1 & m_2 & -m \end{bmatrix}, \tag{12.3}$$

where we define our bracket as[8]

$$\begin{bmatrix} \ell_1 & \ell_2 & \ell_3 \\ m_1 & m_2 & m_3 \end{bmatrix} \equiv \int d\Omega Y_{\ell_1}^{m_1}(\Omega) Y_{\ell_2}^{m_2}(\Omega) Y_{\ell_3}^{m_3}(\Omega) \,. \tag{12.6}$$

It is clear from the integral definition of the bracket that the bracket is invariant under the interchange of indices. As is well known, this bracket, or triple Y_ℓ^m integral, is non vanishing only if several important requirements are met [94]. The first is that $m_1 + m_2 + m_3 = 0$, the m-rule. The next is that $|\ell_i - \ell_j| \leq \ell_k \leq \ell_i + \ell_j$ for different i, j, k, the triangle inequality rule. The third is that $\ell_1 + \ell_2 + \ell_3$ must be even, the parity rule.

Eq. 12.3, relating the inferred anisotropy coefficients (b_ℓ^m's) to the true coefficients (a_ℓ^m's) and exposure coefficients (c_ℓ^m's), is completely general.

The exposures of ground based experiments are essentially constant in the equatorial coordinate "right ascension" (RA). Therefore, expansions of the exposure have non-vanishing coefficients only when the m-value of the $c_{\ell_2}^{m_2}$ expansion coefficient is zero, i.e., $m_2 = 0$. Thus, for experiments with constant efficiency in RA, we may remove the m summations in eq. 12.3 to get

$$b_\ell^m = (-1)^m \sum_{\ell_1} \sum_{\ell_2} a_{\ell_1}^m c_{\ell_2}^0 \begin{bmatrix} \ell & \ell_1 & \ell_2 \\ m & -m & 0 \end{bmatrix} . \tag{12.7}$$

With m_2 identically zero, the m-rule then requires $m_1 = m$, i.e. inferred b_ℓ^m and true $a_{\ell_1}^m$ will share the same m-value. However, the ℓ values will in general differ.

The values of nonzero, independent brackets with ℓ values up to four, and one m value equal to zero, are listed in tables C.1 and C.2 of appendix C. It is seen that the brackets remain sizable even as ℓ increases. In particular, the brackets with one ℓ_1 or ℓ_2 equal to ℓ and the other equal to zero retain their value $\frac{1}{\sqrt{4\pi}}$ for all values of ℓ by orthonormality. The cutoff in the summation in eq. 12.7 must therefore come from the a_ℓ^m and c_ℓ^0 coefficients. The set of a_ℓ^m's are determined by Nature and are awaiting discovery by our experiments. The set of c_ℓ^0's are determined by the location (latitude) of the ground based experiment, and by the experiment's opening angle of acceptance on the sky, and are thus more amenable to providing information about a cutoff.

Since exposures are relatively smooth functions of declination, fits to exposures will be dominated by lower multipoles (small ℓ values). Moreover, as the ground based experiment moves farther from the equator, the symmetry about the equator of its exposure function decreases; this latter fact diminishes the participation of even parity (even ℓ) multipoles in the fits. Thus, we expect the dominant fitted multipole to be the $\ell = 1$ dipole, characterized by c_1^0 (in tandem with an $\ell = 0$ monopole to ensure a positive definite flux across the sky).

---

[8] The triple Y_ℓ^m integral is equal to a product of Clebsch-Gordan coefficients,

$$\int d\Omega Y_{\ell_1}^{m_1}(\Omega) Y_{\ell_2}^{m_2}(\Omega) Y_\ell^m(\Omega) = N(\ell_1, \ell_2, \ell) \times (-1)^m \langle \ell_1 \ell_2; m_1 m_2 | \ell; -m \rangle \,, \tag{12.4}$$

where the normalization factor N depends only on the ℓ's and not on the m's

$$N = \sqrt{\frac{(2\ell_1 + 1)(2\ell_2 + 1)}{4\pi\,(2\ell + 1)}} \times \langle \ell_1 \ell_2; 00 | \ell; 0 \rangle \,. \tag{12.5}$$

The triple Y_ℓ^m integral is also related to Wigner's $3j$ symbol. But our bracket notation is more streamlined for the present problem.

12.2 Low Order Multipoles

In this section we look at several illuminating cases of eq. 12.7 for various small values of ℓ (which corresponds to the scale of the observed coefficient, b_ℓ^m). We have seen that the inferred monopole ($\ell = 0$) is simply given by normalization to be $b_0^0 = \frac{1}{\sqrt{4\pi}}$.

The inferred dipole expansion is more interesting. With $\ell = 1$, the triangle rule and the parity rule restrict the values of, say ℓ_2 relative to ℓ_1, to be ±1. From eq. 12.7, the dipole sum becomes

$$b_1^m = (-1)^m \sum_{\ell_1} \sum_{Z=\pm 1} a_{\ell_1}^m c_{\ell_1+Z}^0 \begin{bmatrix} 1 & \ell_1 & \ell_1+Z \\ m & -m & 0 \end{bmatrix} . \tag{12.8}$$

We learn a lesson here, that an inferred dipole can be "faked" by a non-dipole multipole when multiplied by a multipole component of the exposure differing by one unit of ℓ. As with any angular momentum addition, a true multipole and an exposure multipole can add constructively or destructively.

Finally, we write down the expansion for the inferred quadrupole. Here the triangle rule and the parity rule restrict ℓ_2 to be equal to ℓ_1 or to differ from ℓ_1 by two. The result is

$$b_2^m = (-1)^m \sum_{\ell_1} \sum_{Z=0,\pm 2} a_{\ell_1}^m c_{\ell_1+Z}^0 \begin{bmatrix} 2 & \ell_1 & \ell_1+Z \\ m & -m & 0 \end{bmatrix} . \tag{12.9}$$

Here we learn that an apparent quadrupole can also be faked by a true multipole and a multipole moment of the experimental exposure. For example, a true monopole event distribution (a_0^0) would appear without correction as a quadrupole (b_2^m) if the experimental exposure were quadrupolar (c_2^0). To take a more relevant example, a true dipole distribution observed with a dipole exposure (c_1^0) may appear as a quadrupole distribution (b_2^m).

Experiments with less than 4π exposure, which includes all ground based experiments, are subject to this ambiguity. Assumptions, such as which particular moments Nature chooses to present, must be made. There are two ways around this ambiguity. Both ways require all sky coverage. The first way is to consider space based experiments, such as EUSO. The second way is to combine data from different experiments so that the whole sky is effectively observed. The latter method introduces the sticky problem of combining experiments which have different systematic errors and requires the usage of "fudge" parameters. Combining the data of Auger and TA is an example of the latter approach [88].

12.3 Vanishing Quadrupole Component of the Exposure Function

We turn now to our claim that the quadrupole component of the Auger and TA exposure functions (i.e., the c_2^0 coefficient) is nearly zero in equatorial coordinates at the latitudes of these two experiments. This claim is neither clear nor automatic.

To understand the plausibility of vanishing c_2^0, notice that if experiments were near the equator, then their exposures would show a clear Y_2^0 shape aligned along the pole. On the other hand, if the experiments were at a pole, there would be a quadrupole moment in the exposure, although the exposure would only sense half of it. Moreover, the value of c_2^0 for an experiment at a pole would have the sign of c_2^0 opposite to that of an experiment at the equator. Therefore, we infer that there is some latitude δ in each hemisphere at which c_2^0 must vanish. That unique $|\delta|$ at which c_2^0 vanishes turns out to be very near the latitudes of Auger and TA, as we now show.

In fig. 12.2, we show the first four spherical harmonic coefficients for the exposure function of ground based (fixed latitude δ) experiments. The values of $\ell \neq 2$ are included for scale and

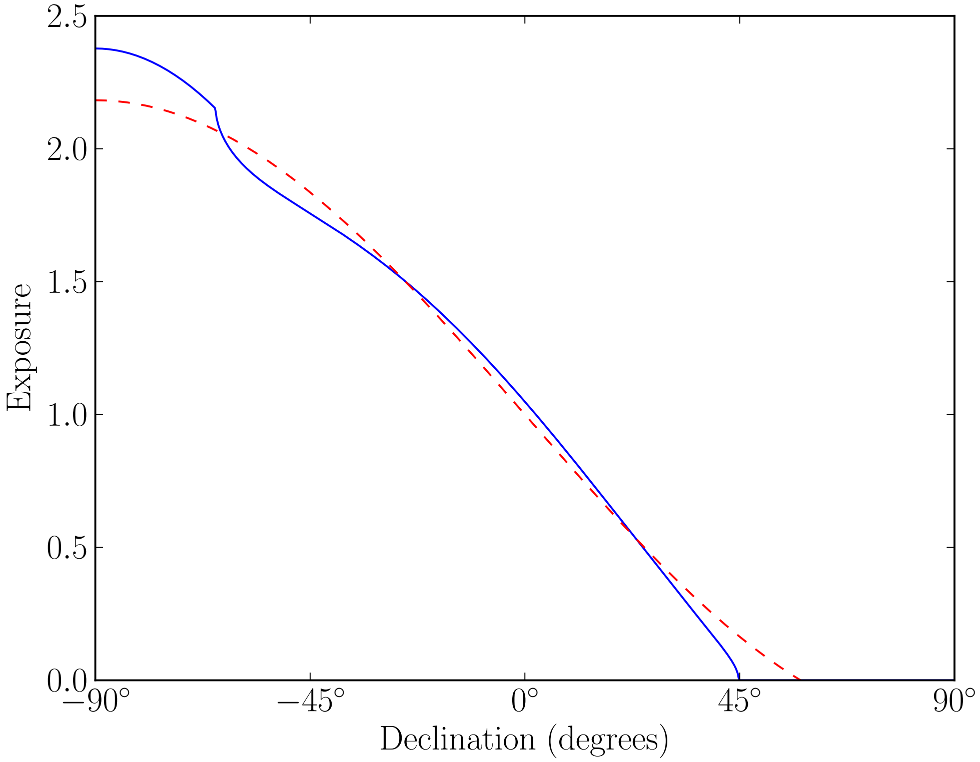

Figure 12.1: The relative exposure of Auger as a function of declination. Note that the exposure is zero for declinations above 45°. The dashed line is the dipole contribution; the contributions from the higher order multipoles are comparatively small as shown in fig. 12.2.

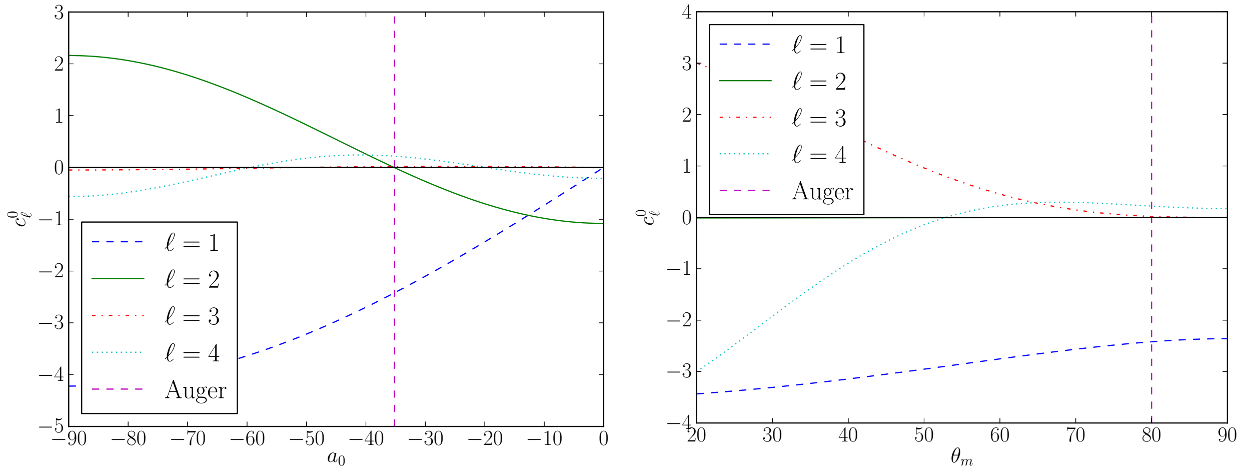

Figure 12.2: In the left panel are the coefficients of the experimental exposure, expressed in terms of spherical harmonics at various latitudes, with $\theta_m = 60°$ fixed. In the right panel are the same coefficients in terms of θ_m, with $a_0 = -35.2°$ fixed to the Auger latitude. In the right panel, the solid green $\ell = 2$ line lies nearly on top of the $c^0_\ell = 0$ line, which implies not only that c^0_2 is nearly vanishing at the Auger latitude, but also that it is independent of θ_m.

comparison. The left panel plots the first four c_ℓ^0 coefficients versus the experimental latitude a_0, in degrees. It is seen that the ±latitude for which c_2^0 vanishes agrees very accurately with the latitudes of Auger and TA. In fact, Auger's latitude is $-35.21°$ (termed a_0 in conventional notation), while the unique latitude at which c_2^0 vanishes is $-35.26°$. The difference between these two latitudes is ~ 7 km – much smaller than the scale of Auger. That is, the latitude at which c_2^0 vanishes runs right through Auger.

It is also seen that the higher ℓ coefficients are small. The values of the fitted coefficients c_0^0, c_1^0, c_2^0, c_3^0, and c_4^0 at the Auger latitude, and with the Auger opening angle of 80°, are $\sqrt{4\pi}$, -2.42, -0.003, 0.019, and 0.218, respectively.

The dependence on the acceptance angle θ_m is shown in the right panel of fig. 12.2. Note that the c_2^0 curve is zero to within the line thickness of the plot for all θ_m. It is seen that variations in this angle does not affect this vanishing of c_2^0 at the Auger latitude.

At Auger's latitude, we see that the largest exposure coefficient in magnitude is c_1^0, and that it is negative. This agrees with the expectation from fig. 12.1, which appears to be largely dipolar in Nature. (We also note that at the equator c_1^0 vanished, while c_2^0 is large as expected. We briefly comment on this case in §12.8.)

A conceptual complication is that the exposure function is necessarily evaluated in equatorial coordinates, while anisotropies of interest are best considered in galactic coordinates. Any rotation in coordinates mixes the set of $(2\ell+1)$ Y_ℓ^m's with fixed ℓ. However, it is possible to reconstruct anisotropy information in the coordinate frame of one's choosing by using the rotationally invariant (see §10.2.2) power spectrum defined in eq. 10.8.

12.4 A Simplifying Cutoff

Armed with the result that the Auger exposure is dominantly dipole (c_1^0) in shape, with a fortuitously small quadrupole ($c_2^0 \ll c_1^0$), and small higher multipoles, we expand the dipole and quadrupole sums up to order $\ell_2 = 2$. This is high enough order to reveal the gift that comes with the justified neglect of c_2^0 for Auger and TA.

Applying a cutoff at $\ell_2 = 2$ in the expansion of the exposure function, eqs. 12.8, and 12.9 are

$$b_1^m = \delta_{m0}\frac{c_1^0}{4\pi} + a_1^m + (-1)^m \left\{ a_1^m c_2^0 \begin{bmatrix} 1 & 1 & 2 \\ m & -m & 0 \end{bmatrix} \right. \\ \left. + a_2^m c_1^0 \begin{bmatrix} 1 & 2 & 1 \\ m & -m & 0 \end{bmatrix} + a_3^m c_2^0 \begin{bmatrix} 1 & 3 & 2 \\ m & -m & 0 \end{bmatrix} \right\}, \tag{12.10}$$

and

$$b_2^m = \delta_{m0}\frac{c_2^0}{4\pi} + a_2^m + (-1)^m \left\{ a_1^m c_1^0 \begin{bmatrix} 2 & 1 & 1 \\ m & -m & 0 \end{bmatrix} + a_2^m c_2^0 \begin{bmatrix} 2 & 2 & 2 \\ m & -m & 0 \end{bmatrix} \right. \\ \left. + a_3^m c_1^0 \begin{bmatrix} 2 & 3 & 1 \\ m & -m & 0 \end{bmatrix} + a_4^m c_2^0 \begin{bmatrix} 2 & 4 & 2 \\ m & -m & 0 \end{bmatrix} \right\}. \tag{12.11}$$

With $|c_2^0(\delta, \theta_m)|$ set to its minimum value of zero, a very good approximation for the latitudes of Auger and TA, we get

$$b_1^m = \delta_{m0}\frac{c_1^0}{4\pi} + a_1^m + (-1)^m a_2^m c_1^0 \begin{bmatrix} 1 & 2 & 1 \\ m & -m & 0 \end{bmatrix}, \tag{12.12}$$

and

$$b_2^m = a_2^m + (-1)^m c_1^0 \left\{ a_1^m \begin{bmatrix} 2 & 1 & 1 \\ m & -m & 0 \end{bmatrix} + a_3^m \begin{bmatrix} 2 & 3 & 1 \\ m & -m & 0 \end{bmatrix} \right\} . \tag{12.13}$$

The dependence of b_1^m on a_3^m, and the dependence of b_2^m on a_4^m, has vanished with c_2^0 set to zero. However, the uncorrected dipole b_1^m still depends on c_1^0 and a_2^m, in addition to a_1^m; while the uncorrected quadrupole b_2^m depends on c_1^0 and a_1^m, and a_3^m, in addition to a_2^m.

From the fit to the Auger exposure function, the value of c_1^0 is -2.42. All of the nonzero brackets in eqs. 12.12 and 12.13 have a factor of $(-1)^m$, and in absolute value are $\in [0.18, 0.26]$. Thus the observed b_ℓ^m, a mixture of the actual a_ℓ^m's, actually contain significant influence from a_ℓ^m's with other ℓ and m values.

We now consider further simplifications on top of the cutoff in the expansion of the exposure function. If it is assumed that Nature's distribution of sources is a true dipole (plus monopole, of course), then all a_ℓ^m vanish except for a_1^m. Then the dipole and quadrupole eqs. 12.12 and 12.13 become simply

$$b_1^m = \delta_{m0} \frac{c_1^0}{4\pi} + a_1^m , \tag{12.14}$$

and

$$b_2^m = (-1)^m a_1^m c_1^0 \begin{bmatrix} 2 & 1 & 1 \\ m & -m & 0 \end{bmatrix} , \tag{12.15}$$

reasserting the notion that the b_ℓ^m include a mixture of the a_ℓ^m. Here the correction to the dipole term is numerically $-0.193\delta_{m0}$ in eq. 12.14 and in eq. 12.15 it is $b_2^m = -0.611a_1^m, -0.529a_1^m, 0$ for $|m| = 0, 1, 2$ respectively. Thus the corrections may well be quite significant.

On the other hand, if it is assumed that Nature's distribution of sources is a true quadrupole (plus monopole), then all a_ℓ^m vanish except for a_2^m, and the dipole and quadrupole eqs. 12.12–12.13 become simply

$$b_1^m = \delta_{m0} \frac{c_1^0}{4\pi} + (-1)^m a_2^m c_1^0 \begin{bmatrix} 1 & 2 & 1 \\ m & -m & 0 \end{bmatrix} , \tag{12.16}$$

and

$$b_2^m = a_2^m . \tag{12.17}$$

Then the dipole term will be notably nonzero, while the quadrupole will be reconstructed correctly and exactly without accounting for the exposure function in any fashion (including the initial cutoff at $\ell_2 > 2$).

The $\bar{b}_\ell^m$'s are determined experimentally and in the limit of $N \to \infty$, $\bar{b}_\ell^m = b_\ell^m$. Thus, eqs. 12.12–12.13 could be inverted to yield the desired a_ℓ^m's. That approach – applying an ℓ_2 cutoff to the expansion of the exposure function and inverting – is similar to the K-matrix approach described in §11.2.2. The mixing of coefficients shows up in the K-matrix approach as taking the inverse of a non-diagonal matrix.

The description presented here has two slight advantages over the K-matrix approach. First, the symmetries making some terms equivalent or zero are made explicit by the properties of the bracket object. Second, the fact that c_2^0 is zero or sufficiently small for Auger and TA respectively can be explicitly taken advantage of. While the K-matrix approach is easily extended to arbitrary order in the ℓ_2 cutoff, the resolution falls off very quickly as the cutoff ℓ_2 is increased; the practicality of the approach fails for $\ell_2 \gtrsim 2$. Auger uses this K-matrix approach, but only up to a cutoff of $\ell_2 = 2$. Auger obtains a result easily reproduced here.

In the next section of this chapter, we follow a similar path, but we include the full expansion of the exposure function and consider the case when Nature provides just a quadrupole anisotropy.

12.5 Pure Quadrupole

When a pure quadrupole moment distribution is assumed, only the reconstructed $b_{\ell=2}^m$ terms are of interest. The pure quadrupolar flux distribution is given by $I_{\text{Quad}}(\Omega) = \frac{1}{4\pi} + \sum_{m=-2}^{2} a_2^m\, Y_2^m(\Omega)$. Then the near vanishing of c_2^0 for Auger and TA leads to the simple relation

$$b_2^m = a_2^m(-1)^m \left\{ c_0^0 \begin{bmatrix} 2 & 2 & 0 \\ m & -m & 0 \end{bmatrix} + c_4^0 \begin{bmatrix} 2 & 2 & 4 \\ m & -m & 0 \end{bmatrix} \right\} . \tag{12.18}$$

The first bracket is $(-1)^m/\sqrt{4\pi}$ and so the first term is simply a_2^m. According to values from table C.1 of appendix C, the second bracket is $f(m)/7\sqrt{4\pi}$, where $f(m) = 6, 4, 1$ for $|m| = 0, 1, 2$, respectively. Inputing these values, the above expression becomes

$$b_2^m = a_2^m \left[1 + \frac{(-1)^m\, c_4^0\, f(m)}{7\sqrt{4\pi}} \right] . \tag{12.19}$$

Using the Auger exposure function yields the value of c_4^0 fitted to the Auger exposure is 0.218, so that the final term is 0.0528, −0.0352, and 0.00880 for $|m| = 0, 1, 2$, respectively. So $b_2^m \approx a_2^m$ up to a correction of $\lesssim 5\%$. We note that the mixing of the a_2^m's with different m values, mentioned previously, actually improves the precision here as the errors are smaller and, in general, with different signs, in the $|m| = 1, 2$ cases than in the $m = 0$ case.

To summarize this section, the fortuitous positioning of Auger and TA at mid-latitudes in the range ±(30 to 40) degrees presents an exposure with no c_2^0 component. In turn, this allows these experiments to equate the experimental b_2^0 with the true a_2^0 quadrupole coefficient to $\lesssim 5\%$, assuming a negligible true dipole contribution, without any consideration of the experiment's partial sky exposure.

The standard technique in the literature to reconstruct the quadrupole moment with full sky exposure is that outlined by Sommers in [87]. Since Auger and TA's partial sky exposures can be ignored when reconstructing a pure quadrupole, we have shown that it is possible to reconstruct the pure quadrupole amplitude using a uniform exposure technique even when the exposure is nonuniform. An explicit presentation of a new approach to reconstruct the quadrupole and a comparison with Sommers's approach can be found in §11.1.3. We note that for the success of either approach, the experiment must be at or near the optimal latitude (or the experiment must have uniform full sky exposure for which it is also the case that $c_\ell^0 = 0$ for all $\ell \geq 1$), and all the multipoles other than the true quadrupole must be small.

12.6 Numerical Verification for the Pure Quadrupole Case

For numerical confirmation that Auger and TA's exposures do not need to be accounted for when reconstructing the quadrupole anisotropy measure, we simulate pure quadrupole distributions of cosmic rays and apply a partial sky exposure at various latitudes. We then reconstruct the pure quadrupole moment.

The process for generating a quadrupole distribution is to first pick a symmetry axis. Then, we generate cosmic rays with a flux

$$I(\Omega) \propto 1 - B\cos^2\theta\,, \tag{12.20}$$

where θ is the angle between the symmetry axis and Ω, and $B \in [0, 1]$ is some constant. We use the standard measure for anisotropy defined in eq. 10.18. For a purely quadrupolar distribution,

$$\alpha_Q = \frac{B}{2 - B} . \tag{12.21}$$

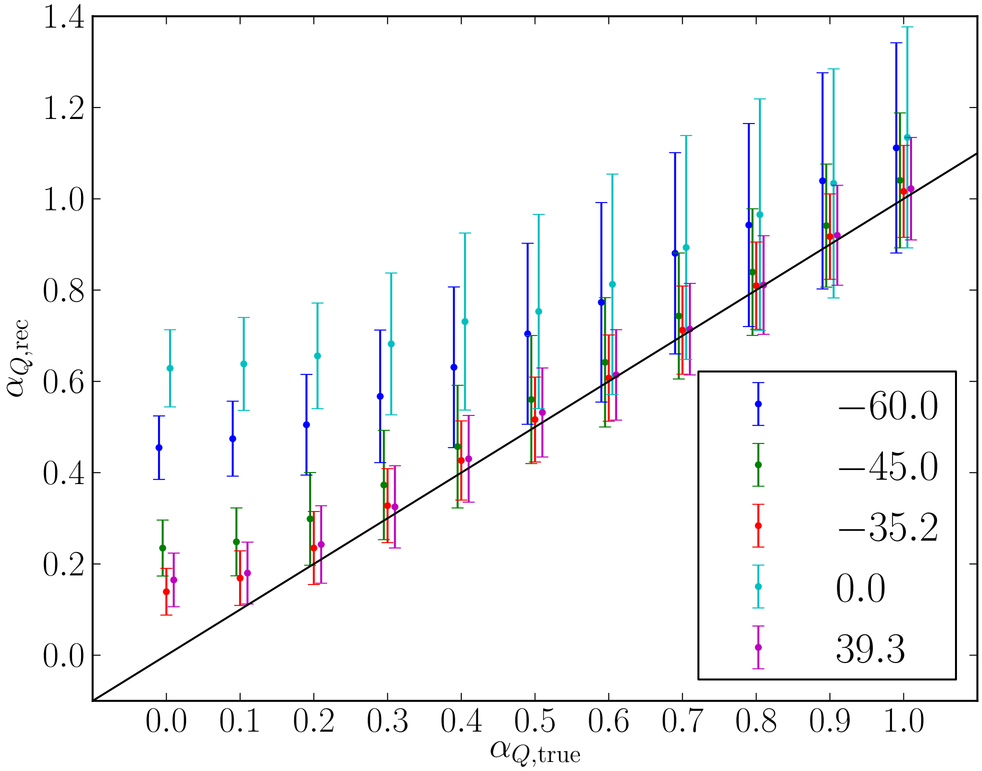

Figure 12.3: Quadrupoles with magnitudes shown on the horizontal axis are injected into an experiment at the shown latitudes. The error bars for the inferred quadrupoles correspond to one standard deviation over 500 repetitions with a different symmetry axis in each repetition. The black line is $\alpha_{Q,\mathrm{rec}} = \alpha_{Q,\mathrm{true}}$. The behavior of the inference at $a_0 = -35.2°$ away from the line at low values of $\alpha_{Q,\mathrm{true}}$ is due to random fluctuations. The horizontal shift within one value of $\alpha_{Q,\mathrm{true}}$ for different latitudes is implemented for clarity only.

The reconstructed pure quadrupole magnitude is shown in fig. 12.3 for several true quadrupole magnitudes and several latitudes. In each simulation, a symmetry axis was randomly chosen. Then 500 cosmic rays were distributed according to the quadrupolar distribution and the experiment's exposure at the given latitude. This process was repeated 500 times and the mean and standard deviation is shown. We see that $a_0 = -35.2°$ (Auger) reconstructs the quadrupole well. In addition, $a_0 = 39.3°$ (TA) reconstructs the quadrupole well (but slightly less so than $|a_0| = 35.2°$). In between the two optimal latitudes, $a_0 = \pm 35.2°$, we see that the ability to simply reconstruct the quadrupole moment vanishes by the large discrepancy in the $a_0 = 0°$ reconstruction attempts. In addition, locating the experiments closer to the poles also nullifies this effect as seen in the $a_0 = -60°$ case. Finally, at $a_0 = -45°$ we see how this effect begins to fall off as we move outside the $30° \lesssim |a_0| \lesssim 40°$ region.

12.7 A Quadrupole Purity Test

In order to determine if a measured quadrupole is pure or if it is tainted by the other spherical harmonics, we propose a simple statistical test. We only consider contamination from the $\ell = 1$ dipole contribution. For a given reconstructed α_Q we want to know that the dipole amplitude α_D,

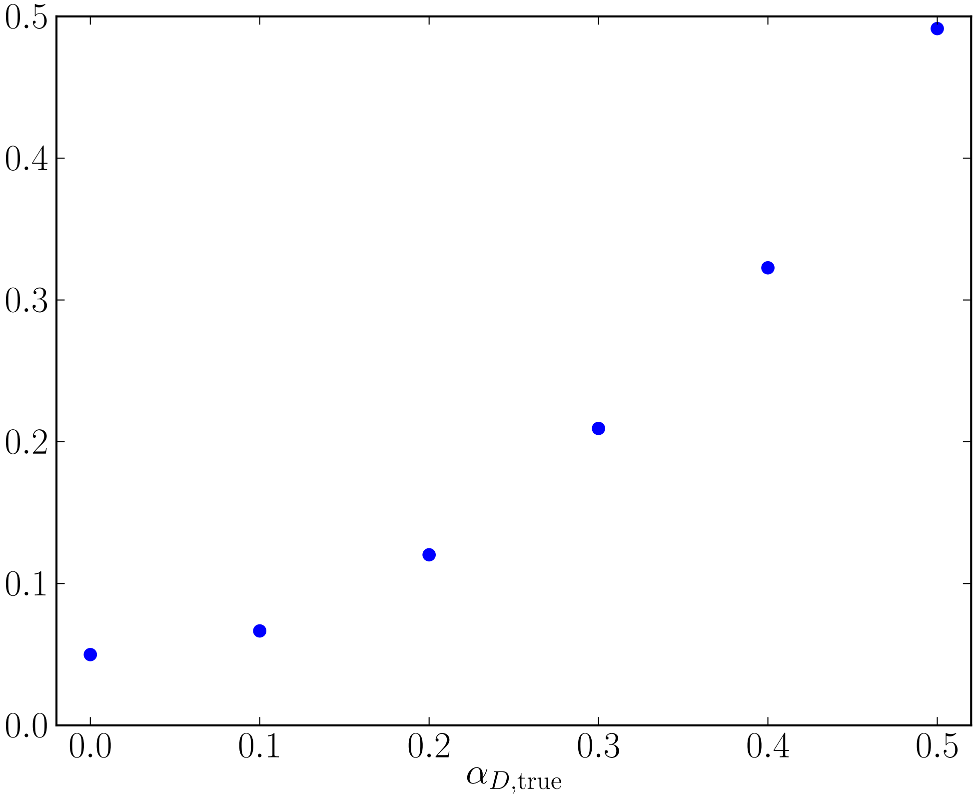

Figure 12.4: Distributions with 500 cosmic rays, Auger's exposure, maximal quadrupolar anisotropy, and varying dipolar anisotropies were simulated. α_D was then reconstructed using the K-matrix approach. Plotted on the vertical axis is the fraction of simulations with $\alpha_{D,\mathrm{rec}}$ not consistent with zero at a 95% confidence level.

our test statistic, is small.

We simulated 500 cosmic rays with Auger's exposure and maximal quadrupole anisotropy, $\alpha_Q = 1$. We then added in increasing amounts of dipole contribution, α_D and reconstructed α_D using the K-matrix approach defined in §11.2.2. After repeating this process 10,000 times we counted how often $\alpha_{D,\mathrm{rec}}$ was greater than the 95% limit for the $\alpha_D = 0$ pure quadrupole case. The results are shown in fig. 12.4.

For example, for a dipole contribution corresponding to $\alpha_D = 0.5$ compared with $\alpha_Q = 1$, there is a 49% chance that $\alpha_D = 0$ could be rejected at the 95% confidence level. As the contaminating dipole gets weaker, so does this probability.

We see that, as we expected, it is not particularly easy to determine if a quadrupole is pure or not with partial sky coverage. As shown in eqs. 12.12–12.13, a quadrupolar signal may mimic a dipolar signal and vice versa.

12.8 Pure Dipole

For completeness, we address the pure dipole analogy to the pure quadrupole discussion of §12.5. When a pure dipole distribution is assumed, we have $I_{\mathrm{Dipole}} = \frac{1}{4\pi} + \sum_{m=-1}^{1} a_1^m Y_1^m(\Omega)$. Then the near vanishing of c_2^0 reduces eq. 12.10 to simply

$$b_1^m = \delta_{m0} \frac{c_1^0}{4\pi} + a_1^m \,, \tag{12.22}$$

the same result as in the ℓ_2 cutoff case shown in eq. 12.14. In the pure quadrupole case, we found that b_2^m was equal to a_2^m times a multiplicative factor that was within a few percent of unity. Here we find the equality between a_1^m and b_1^m is exact for $m \neq 0$, but is broken by an additive factor for $m = 0$. The additive factor is neither large nor small, but rather it is -0.193. This additive factor will also show up with the same relative strength in the power spectrum coefficient C_1.

Referring back to fig. 12.2, one sees that an experiment near the equator would have vanishing c_ℓ^0's except for the quadrupole $c_2^0 \sim -1.08$. It is amusing to ask what pure dipole reconstruction might be possible with such an experimental location. Eq. 12.22 is replaced with the following equation:

$$\begin{aligned} b_1^m &= a_1^m \left\{ 1 + (-1)^m c_2^0 \begin{bmatrix} 1 & 1 & 2 \\ m & -m & 0 \end{bmatrix} \right\} \\ &= a_1^m \left[1 + 0.14(1 - 3\delta_{m0}) \right] \,. \end{aligned} \tag{12.23}$$

Unfortunately, the multiplicative correction from the now nonzero c_2^0 coefficient is large.

Chapter 13

Distinguishing Between Dipoles and Quadrupoles

One topic of concern is determining at what significance an injected dipole (quadrupole) distribution can be distinguished from a quadrupole (dipole), and from isotropy. Generally, the level of significance will depend on the number of observed cosmic ray events, the strength of the anisotropy, etc. Fig. 13.1 shows what happens when Auger or EUSO attempt to reconstruct a pure dipole or a pure quadrupole when the signal is actually the opposite. The mean values and one standard deviation error bars are derived from 500 repetitions of the given number of cosmic ray events, where the dipole or quadrupole axis direction is randomly distributed on the sphere. The dashed lines in each plot are the 95% upper limit for an isotropic distribution (i.e., $\alpha_{\rm true} = 0$). We see that as the actual anisotropy strength increases, quite a significant region of the parameter space would show an anisotropy in the absent multipole at the 95% confidence level when reconstructed by Auger. We also see that the relative size of the error bars reflects the statistical advantage of space based observatories, while the central values of the data points, falsely rising with $\alpha_{\rm true}$ for Auger but constant for EUSO, reveals the systematic difference of partial sky coverage versus full sky coverage.

This entire discussion is easily understood in the context of the "interference" of spherical harmonics which have been effectively truncated on the part of the sky where the exposure vanishes. The various truncated harmonics interfere heavily, a fact that is built into the K-matrix method (and into any method that attempts to reconstruct spherical harmonics based on only partial sky exposure). Even though the true exposure of EUSO won't be exactly uniform, the fact that it sees the entire sky with nearly comparable coverage means that the individual spherical harmonics are noninterfering, and so can be treated independently.

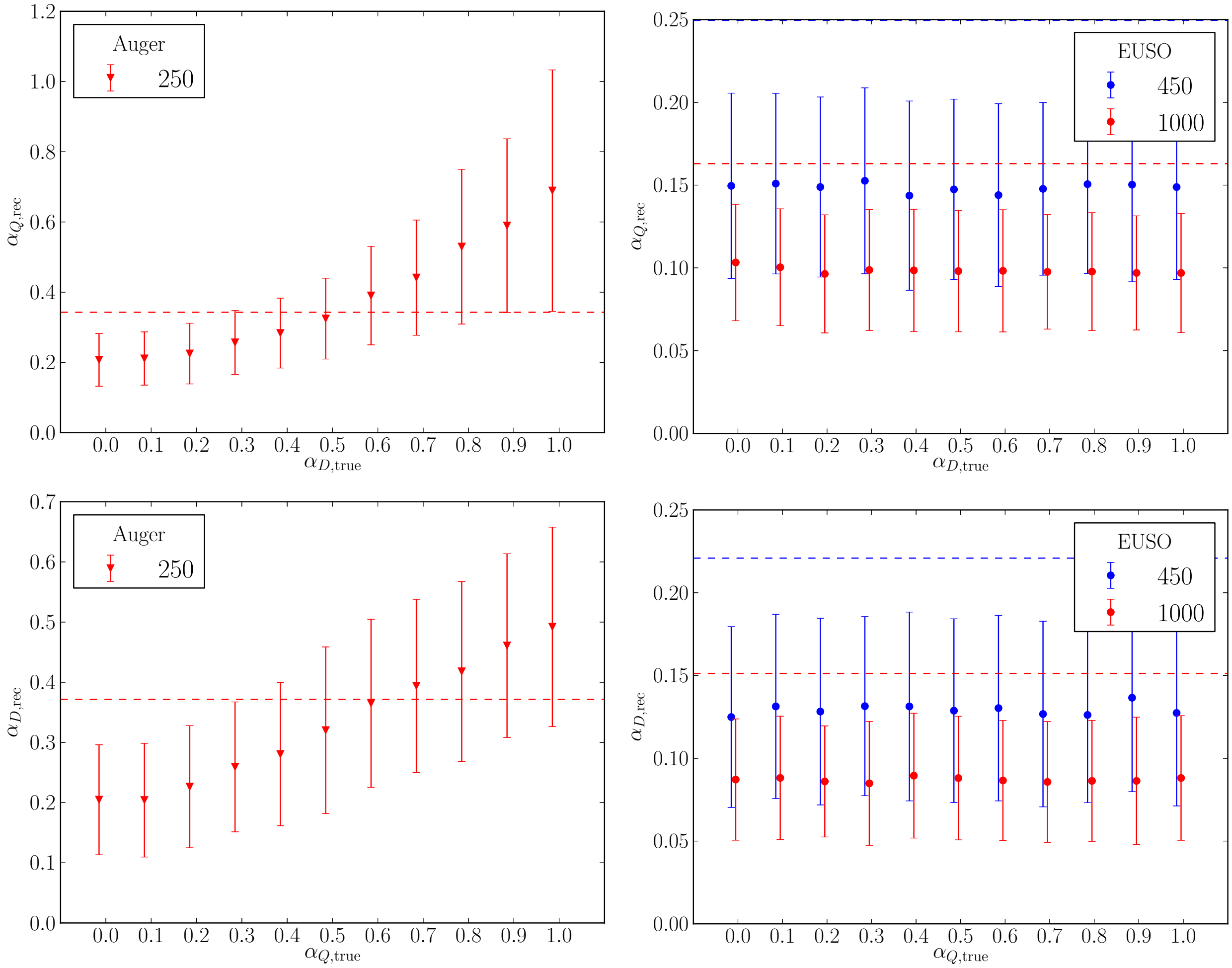

Figure 13.1: These panels show the results of attempting to reconstruct a dipole (quadrupole) when there is actually a quadrupole (dipole). The top two panels show the effect of attempting to infer a quadrupole moment from a pure dipole state of varying magnitudes while the bottom two panels show the effect of attempting to infer the dipole moment from a pure quadrupole state of varying magnitudes. The left two panels assume Auger's partial coverage and 250 cosmic rays, while the right panels assume uniform exposure and the estimated number of events for EUSO (450 minimally, and 1000 maximally). The mean values and the one standard deviation error bars are derived from 500 samplings. Note that the left most data point in each plot ($\alpha_{(D,Q),\text{true}} = 0$) corresponds to the isotropic case, for which the dashed lines are the 95% upper limit. Finally, note that the vertical scales vary significantly between the partial sky low statistics and full sky larger statistics figures.

Chapter 14

Results

In this chapter we tally our results of the comparison of space based full sky and ground based partial sky experiments' abilities to reconstruct anisotropies. The standard procedure involves simulating a number of cosmic rays with a given dipolar or quadrupolar anisotropy shape and amplitude (α_{true}) aligned in a random direction. We then reconstruct the amplitude (α_{rec}) and direction (here we assume knowledge of the kind of anisotropy – dipole or quadrupole – unlike in chapter 13) and compare to the true values. This process is repeated 500 times and the shown uncertainties are one standard deviation over the 500 repetitions.

14.1 Dipole results

In fig. 14.1 we compare the capabilities of design EUSO and Auger to reconstruct a dipole anisotropy. In this comparison, both advantages of EUSO, namely the increased FOV and the 4π sky coverage, are evident.

The first panel shows how changing only the exposure function between Auger and EUSO affects the value of the reconstructed dipole amplitude. For the same number of cosmic ray events, the EUSO reconstruction is a bit closer to the expected value and has a smaller variation than does the Auger reconstruction. In the next panel we show the angular separation between the actual dipole direction and the reconstructed direction for Auger after a maximal amount of Auger data of ~ 250 cosmic ray events, compared to EUSO's minimal and maximal data sizes: 450 and 1000 cosmic ray events, respectively. Even for a pure dipole, Auger will only reach 10° accuracy in dipole direction for a maximum strength dipole, $\alpha_D = 1$, while EUSO does much better. In the third panel we compare both experiments at the same number of cosmic rays across a range of dipole strengths. Even if we assume that Auger will see significantly more cosmic rays than it is expected to, it still has a larger error in its ability to reconstruct a dipole of any amplitude than EUSO. The low dipole magnitudes will always lead to a small erroneously reconstructed dipole due to random walking away from zero. Finally, in the fourth panel we show the discovery power of each experiment to distinguish a dipole amplitude from isotropy. We see that Auger with 250 events would claim a discovery at five standard deviations above isotropy only if the dipole strength is 0.62 or greater – a situation that is unlikely given Auger's anisotropy results to date [88]. EUSO could claim the same significance if the dipole amplitude is $0.37, 0.30, 0.27$, or greater, for 450, 750, or 1000 events, respectively. The EUSO significance should be enough to probe at high significance the weak signal currently reported by Auger.

14.2 Quadrupole results

In fig. 14.2 we again compare Auger and design EUSO in the context of quadrupole anisotropies. The same panels are plotted here as in fig. 14.1 except with an initial quadrupole rather than dipole anisotropy, and a quadrupole reconstructed. We note that while the increased number of events that EUSO will detect will certainly lead to a better resolution of the quadrupole amplitude (as shown in the first and fourth panels) and direction (as shown in the second panel), we see that the full sky coverage does not provide any benefit in this case (as deduced from the first and third

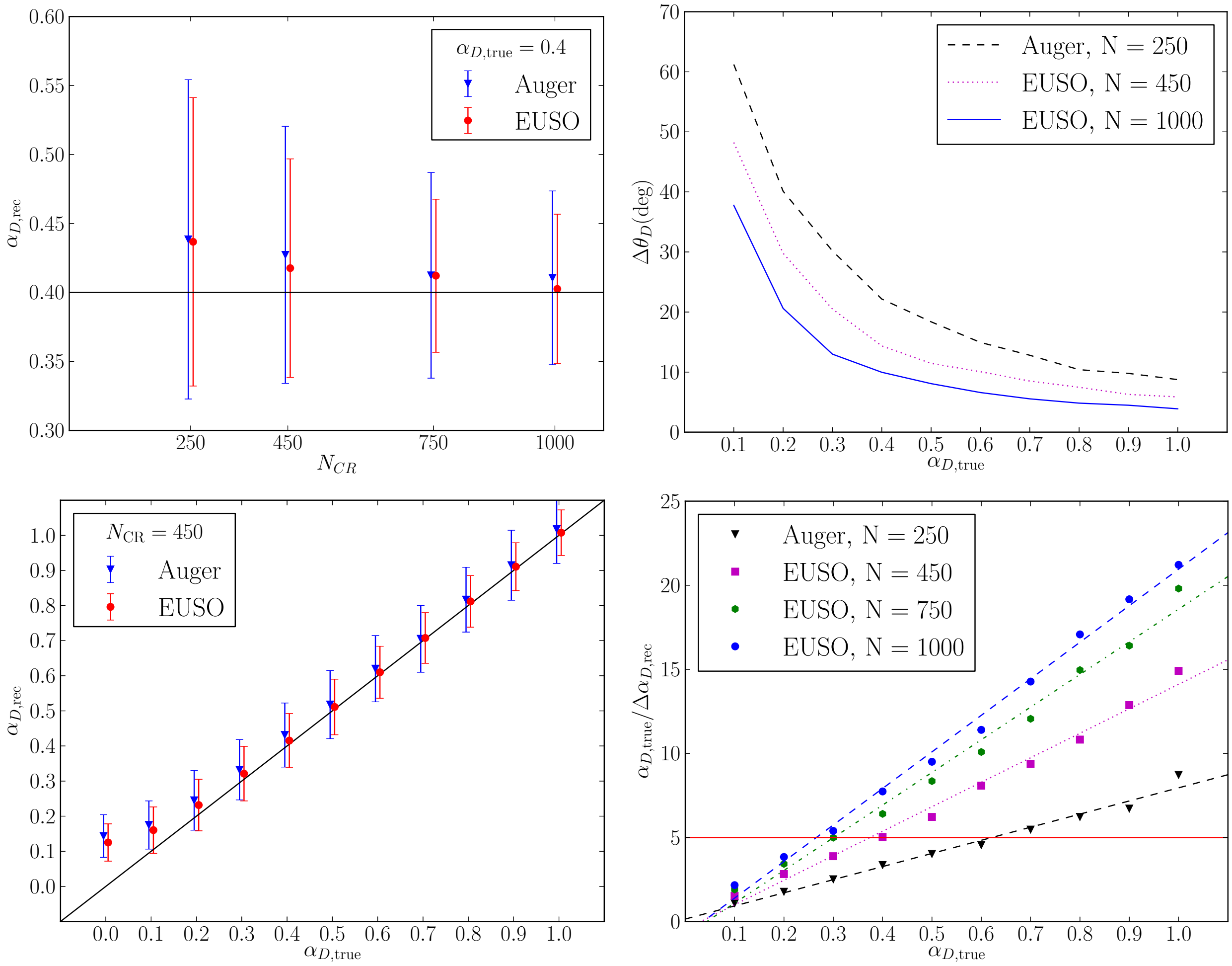

Figure 14.1: Reconstruction of the dipole amplitude and direction across various parameters. Each data point is the mean value (and one standard deviation error bar as applicable) determined from 500 independent simulations. The dipole amplitude and direction for Auger's partial coverage were reconstructed with the K-matrix approach. The ordinate on the fourth panel, $\frac{\alpha_{\mathrm{true}}}{\Delta\alpha_{\mathrm{rec}}}$, labels the number of standard deviations above $\alpha_D = 0$.

panels). This result numerically confirms the claims made in chapter 12 that Auger with $c_2^0 = 0$ does well with assumed quadrupole.

Even though EUSO gains no benefit from its full sky exposure for the determination of a quadrupole anisotropy, EUSO's increased statistics will still lead to a detection sooner than Auger. Auger with 250 events would only be expected to claim a quadrupole discovery at five standard deviations above isotropy if the quadrupole strength is 0.67 or greater. EUSO could claim the same significance if the quadrupole amplitude is $0.47, 0.36, 0.29$, or greater, for 450, 750, or 1000 events, respectively.

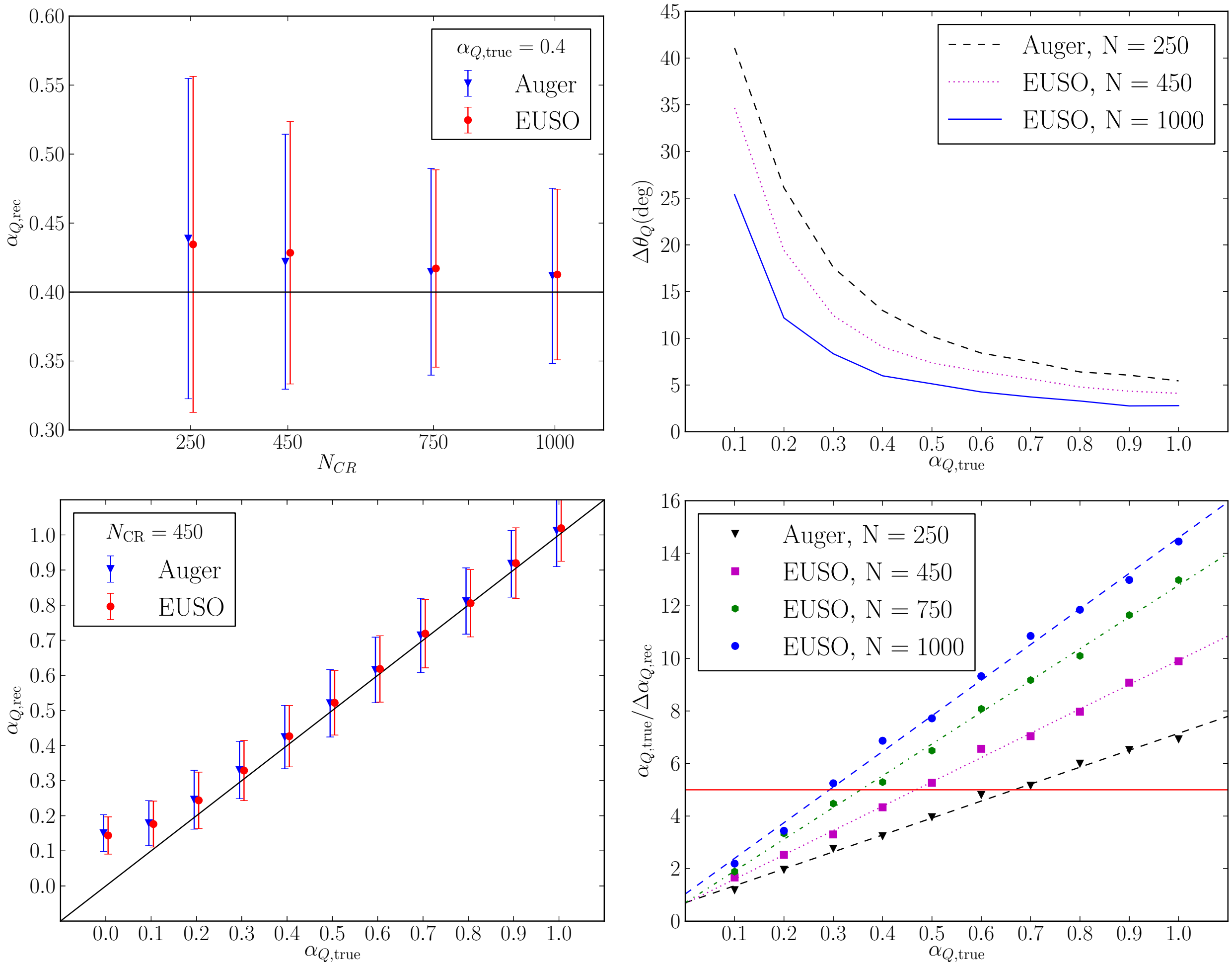

Figure 14.2: Reconstruction of the quadrupole amplitude and direction across various parameters. Each data point is the mean value (and one standard deviation error bar as applicable) determined from 500 independent simulations. The quadrupole amplitude and direction for Auger's partial coverage and the full sky (EUSO) case were reconstructed with Sommers's approach using the result of chapter 12. The ordinate on the fourth panel, $\frac{\alpha_{\mathrm{true}}}{\Delta\alpha_{\mathrm{rec}}}$, labels the number of standard deviations above $\alpha_Q = 0$.

Chapter 15

Conclusions

The interesting result from chapter 12, $b_2^m \approx a_2^m$ as given in eq. 12.19, occurs only in the case where the experimental latitude is near ±35°. At these special latitudes, the reconstruction of a pure quadrupole source distribution is not disadvantaged by partial sky coverage. By a lucky chance, Auger is located at precisely the correct latitude to benefit from the vanishing of c_2^0. TA's latitude is sufficiently close to 35° to also benefit.

If Auger and TA reconstruct both a dipole and a quadrupole simultaneously, then the simplification fails, since both experiments have significant dipole moments in their exposure functions. The confusion is apparent in the mixing within eqs. 12.12 and 12.13. With any source distribution that contains more than a single nontrivial multipole, the partial sky coverage inherent in these ground based experiments exacts a significant price as shown in figs. 14.1 and 14.2.

Considering that an experiment 5° away from the optimal latitude reconstructs the quadrupole well while 10° does not, we claim that experiments at latitudes $30^\circ \lesssim |a_0| \lesssim 40^\circ$ can reconstruct a pure quadrupole moment while ignoring their experiment's particular exposure.

Many well motivated models predict, in the simplest limit, a dipolar or quadrupolar anisotropy in the UHECR flux. The importance of the two lowest nontrivial orders ($\ell = 1, 2$) can be seen from the 2MRS distribution of the 5310 nearest galaxies that was demonstrated in fig. 10.1. Due to the lack of any conclusive anisotropy from the partial sky ground based experiments, we explored the possible benefits that a full sky space based experiment, such as proposed EUSO, has over a ground based experiment for detecting dipolar or quadrupolar anisotropies. In particular, we see that in addition to the increased statistics that proposed EUSO brings over any ground based experiment, proposed EUSO significantly outperforms Auger when reconstructing a dipole. Moreover, for inferences of both the dipole and the quadrupole, partial sky experiments fail to differentiate between the two due to the mixing of the spherical harmonics when truncated by the exposure function. This situation is not present with all sky observation, where the exposure function is nearly uniform and nonzero everywhere.

Appendix

B b10-cut

The source catalog from the 2MRS [12] has a 'b10-cut' applied to it. That is, only galaxies with $|b| > 10^\circ$ are included due to the obscuring effects of our own Milky Way galaxy. In order to calculate the spherical harmonics correctly on a partial sky-map, this effect can be analytically considered due to the simple nature of the "exposure map" unlike that of Auger which has a highly non-linear shape and misses much of the sky.

A uniform intensity distribution is given by

$$I_u(\Omega) = \frac{1}{4\pi}\,. \tag{B.1}$$

We then define another distribution over part of the sky by

$$I_{u,<10}(\Omega) = \frac{1}{4\pi}\begin{cases}1 & |\cos\theta| < \cos(80^\circ)\\ 0 & \text{else}\end{cases}\,. \tag{B.2}$$

where θ is the polar angle measured from the galactic north pole. Then the remaining sky looks like

$$I_{u,>10}(\Omega) = I_u(\Omega) - I_{u,<10}(\Omega)\,, \tag{B.3}$$

$$I_{u,>10}(\Omega) = \frac{1}{4\pi}\begin{cases}0 & |\cos\theta| < \cos(80^\circ)\\ 1 & \text{else}\end{cases}\,. \tag{B.4}$$

Next we express the distribution of local galaxies by splitting the sky as expected,

$$I_g(\Omega) = I_{g,>10}(\Omega) + I_{g,<10}(\Omega)\,. \tag{B.5}$$

Since there is not complete information about $I_{g,<10}$, we replace it with a uniform distribution,

$$I_g(\Omega) = I_{g,>10}(\Omega) + I_{u,<10}(\Omega)\,. \tag{B.6}$$

We take the usual definition of a_ℓ^m from eq. 10.1,

$$I(\Omega) = \sum_{\ell=0}^{\infty}\sum_{m=-\ell}^{\ell} a_\ell^m Y_\ell^m(\Omega)\,. \tag{B.7}$$

By orthogonality of the Y_ℓ^m,

$$a_\ell^m = \int Y_\ell^m(\mathbf{u}) I(\mathbf{u}) d\Omega\,. \tag{B.8}$$

By linearity, the coefficients are then,

$$(a_\ell^m)_g = (a_\ell^m)_{g,>10} + (a_\ell^m)_{u,<10}\,, \tag{B.9}$$

where $(a_\ell^m)_{g,>10}$ is the quantity that will be measured and $(a_\ell^m)_{u,<10}$ is a correction to be applied to give the desired quantity $(a_\ell^m)_g$. From eq. B.2 we note that $I_{u,<10}(\Omega)$ isn't a function of ϕ and use

$$\int d\phi e^{im\phi} = 2\pi\delta_{m0}\,. \tag{B.10}$$

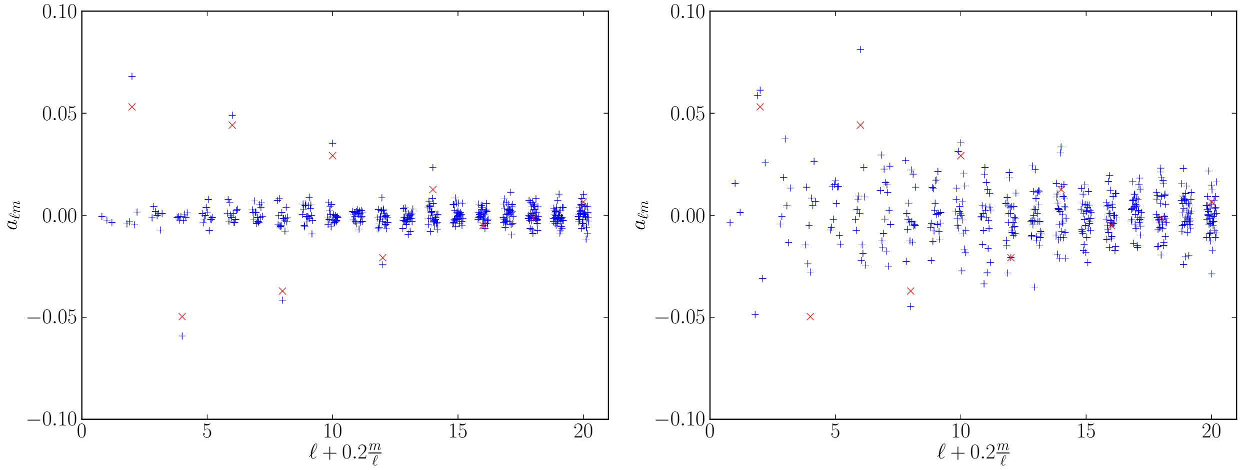

Figure 15.1: The red x's are the analytic calculation of eq. B.13 which line up with the large spikes as expected. On the left is a uniformly generated sky map with a 'b10-cut'. The data on the right is the unmodified a_ℓ^m's calculated from the positions of the galactic data set.

Then we have

$$a_\ell^m = 2\pi\sqrt{\frac{2\ell+1}{4\pi}}\int P_\ell(x)I(x)d(x)\delta_{m0}\,, \tag{B.11}$$

where $x = \cos\theta$. Next, since $I_{u,<10}(\Omega)$ is even in $\cos\theta$ and the P_ℓ have definite parity, only $\ell = 2k$ for $0 < k \in \mathbb{Z}$ remain. From eq. B.3,

$$(a_{2k}^0)_{u,>10} = -(a_{2k}^0)_{u,<10} \qquad 0 < k \in \mathbb{Z}\,, \tag{B.12}$$

since $(a_{2k}^0)_u = 0$ for $k > 0$. So we have that $(a_\ell^m)_{u,<10} \neq 0$ only for $m = 0, \ell = 2k$ and those coefficients are given by

$$(a_\ell^0)_{u,<10} = \sqrt{\frac{2\ell+1}{4\pi}}\int_0^{\cos(80^\circ)} P_\ell(x)dx\,. \tag{B.13}$$

Numerical confirmation is shown in fig. 15.1. All relevant calculations in the paper have been modified according to eqs. B.9 and B.13.

C Tables of Low Multipole Square Brackets

Eq. 12.7 describes the general relation between the experimentally inferred raw multipole coefficients b_ℓ^m, and the true multipole coefficients a_ℓ^m and exposure coefficients c_ℓ^0, in terms of a bracket of the form

$$\begin{bmatrix} \ell & \ell_1 & \ell_2 \\ m & -m & 0 \end{bmatrix}, \tag{C.1}$$

for an experiment with uniform exposure in RA, where we recall from their definition in eq. 12.6 that the square bracket is the integral of three Y_ℓ^m's. In this appendix, we list the nonzero, independent such bracket objects and their values, including all ℓ values up to four in tables C.1 and C.2. We note that the nonzero brackets remain large in magnitude as ℓ, ℓ_1, ℓ_2 are increased. In particular, they do not generally go to zero with increasing ℓ values.

ℓ (m)	ℓ_1 $(-m)$	ℓ_2 $(m_2 = 0)$	m	$\sqrt{4\pi}\begin{bmatrix}\ell & \ell_1 & \ell_2 \\ m & -m & 0\end{bmatrix}$
0	ℓ_1	$\ell_2 = \ell_1$	0	1
ℓ	0	$\ell_2 = \ell$	0	1
ℓ	$\ell_1 = \ell$	0	any $\lvert m\rvert \leq \ell$	$(-1)^m$
1	1	2	0	$\frac{2}{\sqrt{5}}$
			± 1	$\frac{1}{\sqrt{5}}$
1	2	1	± 1	$-\sqrt{\frac{3}{5}}$
1	2	3	0	$3\sqrt{\frac{3}{35}}$
			± 1	$\frac{3}{\sqrt{35}}$
1	3	2	± 1	$-3\sqrt{\frac{2}{35}}$
1	3	4	0	$\frac{4}{\sqrt{21}}$
			± 1	$\sqrt{\frac{2}{7}}$
1	4	3	± 1	$-\sqrt{\frac{10}{21}}$
2	2	2	0	$\frac{2\sqrt{5}}{7}$
			± 1	$-\frac{\sqrt{5}}{7}$
			± 2	$-\frac{2\sqrt{5}}{7}$
2	2	4	0	$\frac{6}{7}$
			± 1	$\frac{4}{7}$
			± 2	$\frac{1}{7}$
2	3	1	± 1	$-2\sqrt{\frac{6}{35}}$
			± 2	$\sqrt{\frac{3}{7}}$
2	3	3	0	$\frac{4}{3\sqrt{5}}$
			± 1	$-\frac{1}{3}\sqrt{\frac{2}{5}}$
			± 2	$-\frac{2}{3}$
2	4	2	± 1	$-\frac{\sqrt{30}}{7}$
			± 2	$\frac{\sqrt{15}}{7}$
2	4	4	0	$\frac{20\sqrt{5}}{77}$
			± 1	$-\frac{5\sqrt{6}}{77}$
			± 2	$-\frac{30\sqrt{3}}{77}$

Table C.1: Values for independent, non-vanishing brackets with $\ell = 0, 1$, and 2, when $m_2 = 0$. When $m = 0$ as well, the brackets are symmetric under interchange of any ℓ values.

ℓ (m)	ℓ_1 $(-m)$	ℓ_2 $(m_2 = 0)$	m	$\sqrt{4\pi}\begin{bmatrix}\ell & \ell_1 & \ell_2 \\ m & -m & 0\end{bmatrix}$
3	3	2	±1	$-\frac{1}{\sqrt{5}}$
			±2	0
			±3	$\frac{\sqrt{5}}{3}$
3	3	4	0	$\frac{6}{11}$
			±1	$-\frac{1}{11}$
			±2	$-\frac{7}{11}$
			±3	$-\frac{3}{11}$
3	4	1	±1	$-\sqrt{\frac{5}{7}}$
			±2	$\frac{2}{\sqrt{7}}$
			±3	$-\frac{1}{\sqrt{3}}$
3	4	3	±1	$-\frac{\sqrt{15}}{11}$
			±2	$-\frac{\sqrt{3}}{11}$
			±3	$\frac{3\sqrt{7}}{11}$
4	4	2	±1	$-\frac{17\sqrt{5}}{77}$
			±2	$\frac{8\sqrt{5}}{77}$
			±3	$\frac{\sqrt{5}}{11}$
			±4	$-\frac{4\sqrt{5}}{11}$
4	4	4	0	$\frac{486}{1{,}001}$
			±1	$-\frac{243}{1{,}001}$
			±2	$-\frac{27}{91}$
			±3	$\frac{81}{143}$
			±4	$\frac{54}{143}$

Table C.2: Values for independent, non-vanishing brackets for $\ell = 3$ and 4, when $m_2 = 0$. When $m = 0$ as well, the brackets are symmetric under interchange of any ℓ values.

Bibliography

[1] P. B. Denton and T. J. Weiler, "Using integral dispersion relations to extend the LHC reach for new physics," *Phys. Rev. D* **89** (Feb, 2014) 035013, `arXiv:1311.1248 [hep-ph]`.

[2] **JEM-EUSO** Collaboration, P. B. Denton, L. A. Anchordoqui, A. A. Berlind, M. Richardson, and T. J. Weiler, "Sensitivity of orbiting JEM-EUSO to large-scale cosmic-ray anisotropies," *J. Phys. Conf. Ser.* **531** (2014) 012004, `arXiv:1401.5757 [astro-ph.IM]`.

[3] P. B. Denton and T. J. Weiler, "The Fortuitous Latitude of the Pierre Auger Observatory and Telescope Array for Reconstructing the Quadrupole Moment," *Astrophys. J.* **802** no. 1, (2015) 25, `arXiv:1409.0883 [astro-ph.HE]`.

[4] P. B. Denton and T. J. Weiler, "Sensitivity of full-sky experiments to large scale cosmic ray anisotropies," *JHEAp* **8** (2015) 1–9, `arXiv:1505.03922 [astro-ph.HE]`.

[5] N. Arsene, L. I. Caramete, P. B. Denton, and O. Micu, "Quantum Black Holes Effects on the Shape of Extensive Air Showers," `arXiv:1310.2205 [hep-ph]`.

[6] L. A. Anchordoqui, P. B. Denton, H. Goldberg, T. C. Paul, L. H. M. Da Silva, B. J. Vlcek, and T. J. Weiler, "Weinberg's Higgs portal confronting recent LUX and LHC results together with upper limits on B^+ and K^+ decay into invisibles," *Phys. Rev.* **D89** no. 8, (2014) 083513, `arXiv:1312.2547 [hep-ph]`.

[7] P. B. Denton, H. Minakata, and S. J. Parke, "Compact Perturbative Expressions For Neutrino Oscillations in Matter," `arXiv:1604.08167 [hep-ph]`.

[8] P. B. Denton, "`Nu-Pert` v0.2.2," June, 2016. `http://dx.doi.org/10.5281/zenodo.54629`. `https://github.com/PeterDenton/Nu-Pert`.

[9] M. Block and F. Halzen, "Duality as a robust constraint on the LHC cross section," *Phys.Rev.* **D73** (2006) 054022, `arXiv:hep-ph/0510238 [hep-ph]`.

[10] M. M. Block and F. Halzen, "Forward hadronic scattering at 8 TeV: predictions for the LHC," *Phys.Rev.* **D86** (2012) 014006, `arXiv:1205.5514 [hep-ph]`.

[11] **JEM-EUSO** Collaboration, J. H. Adams *et al.*, "An evaluation of the exposure in nadir observation of the JEM-EUSO mission," *Astropart. Phys.* **44** (2013) 76–90, `arXiv:1305.2478 [astro-ph.HE]`.

[12] J. P. Huchra, L. M. Macri, K. L. Masters, T. H. Jarrett, P. Berlind, *et al.*, "The 2MASS Redshift Survey - Description and Data Release," *Astrophys.J.Suppl.* **199** (2012) 26, `arXiv:1108.0669 [astro-ph.CO]`.

[13] H. Goldberg and T. J. Weiler, "Lower energy consequences of an anomalous high-energy neutrino cross section," *Phys. Rev. D* **59** (Apr, 1999) 113005. `http://link.aps.org/doi/10.1103/PhysRevD.59.113005`.

[14] R. D. L. Kronig, "On the theory of dispersion of x-rays," *J. Opt. Soc. Am.* **12** no. 6, (Jun, 1926) 547 – 556. Kronig includes the following footnote at the beginning of his paper: "As Professor Kramers kindly informs me, he too has obtained most of the results derived in 3. (To be published shortly.)".

[15] H. A. Kramers, “La diffusion de la lumière par les atomes,” in *Atti del Congresso Internazionale dei Fisici, Como-Pavia-Roma*, vol. 2, pp. 545 – 557. 1927.

[16] M. Gell-Mann, M. L. Goldberger, and W. E. Thirring, “Use of causality conditions in quantum theory,” *Phys. Rev.* **95** (Sep, 1954) 1612 – 1627.

[17] P. Söding, “Real part of the proton-proton and proton-antiproton forward scattering amplitude at high energies,” *Physics Letters* **8** no. 4, (1964) 285 – 287.

[18] M. Block and R. Cahn, “High-Energy $p\bar{p}$ and pp Forward Elastic Scattering and Total Cross-Sections,” *Rev.Mod.Phys.* **57** (1985) 563.

[19] **CDF** Collaboration, F. Abe *et al.*, “Measurement of the $\bar{p}p$ total cross-section at $\sqrt{s} = 546$ GeV and 1800-GeV,” *Phys. Rev.* **D50** (1994) 5550–5561.

[20] **TOTEM** Collaboration, G. Antchev *et al.*, “Luminosity-independent measurements of total, elastic and inelastic cross-sections at $\sqrt{s} = 7$ TeV,” *Europhys. Lett.* **101** (2013) 21004.

[21] R. M. Baltrusaitis, G. L. Cassiday, J. W. Elbert, P. R. Gerhardy, S. Ko, E. C. Loh, Y. Mizumoto, P. Sokolsky, and D. Steck, “Total Proton Proton Cross-Section at s**(1/2) = 30-TeV,” *Phys. Rev. Lett.* **52** (1984) 1380–1383.

[22] M. Honda, M. Nagano, S. Tonwar, K. Kasahara, T. Hara, N. Hayashida, Y. Matsubara, M. Teshima, and S. Yoshida, “Inelastic cross-section for p-air collisions from air shower experiment and total cross-section for p p collisions at SSC energy,” *Phys. Rev. Lett.* **70** (1993) 525–528.

[23] **Pierre Auger** Collaboration, P. Abreu *et al.*, “Measurement of the proton-air cross-section at $\sqrt{s} = 57$ TeV with the Pierre Auger Observatory,” *Phys. Rev. Lett.* **109** (2012) 062002, `arXiv:1208.1520 [hep-ex]`.

[24] R. J. Glauber, “Cross sections in deuterium at high energies,” *Phys. Rev.* **100** (Oct, 1955) 242–248.

[25] A. Alkin, J. Cudell, and E. Martynov, “Dispersion relations for meson-proton and proton-proton forward elastic scattering,” *Few Body Syst.* **53** (2012) 87 – 98, `arXiv:1109.1306 [hep-ph]`.

[26] S. Mandelstam, “Determination of the pion - nucleon scattering amplitude from dispersion relations and unitarity. General theory,” *Phys.Rev.* **112** (1958) 1344 – 1360.

[27] M. E. Peskin and D. V. Schroeder, *An Introduction To Quantum Field Theory*, pp. 230–236. Addison-Wesley Publishing Company, 1995. Two approaches are discussed. One based on an S-matrix approach and the other based on a Feynman diagram approach.

[28] M. Froissart, “Asymptotic behavior and subtractions in the mandelstam representation,” *Phys. Rev.* **123** (Aug, 1961) 1053–1057.

[29] Y. Azimov, “How Robust is the Froissart Bound?,” *Phys.Rev.* **D84** (2011) 056012, `arXiv:1104.5314 [hep-ph]`.

[30] A. Martin and S. Roy, “Froissart Bound on Total Cross-section without Unknown Constants,” *Phys.Rev.* **D89** (2014) 045015, `arXiv:1306.5210 [hep-ph]`.

[31] Y. I. Azimov, "Comment on "Froissart bound on total cross section without unknown constants" by A. Martin and S.M. Roy [arXiv:1306.5210]," `arXiv:1405.2448 [hep-ph]`.

[32] I. Y. Pomeranchuk, "Equality of total cross sections of interactions of nucleons and antinucleons at high energies," *JETP* **34** (1958) 725.

[33] R. J. Eden, "Use of unitarity in proving pomeranchuk's theorem on cross sections at high energies," *Phys. Rev. Lett.* **16** (Jan, 1966) 39–41.

[34] T. Kinoshita in *Perspectives in Modern Physics*, R. E. Marshak, ed., p. 211. John Wiley and Sons, 1st ed., 1966.

[35] **Particle Data Group** Collaboration, J. Beringer *et al.*, "Review of particle physics," *Phys. Rev. D* **86** (Jul, 2012) 010001.

[36] M. Block and F. Halzen, "Evidence for the saturation of the Froissart bound," *Phys.Rev.* **D70** (2004) 091901, `arXiv:hep-ph/0405174 [hep-ph]`.

[37] M. M. Block and F. Halzen, "New experimental evidence that the proton develops asymptotically into a black disk," *Phys.Rev.* **D86** (2012) 051504, `arXiv:1208.4086 [hep-ph]`.

[38] `totem-experiment.web.cern.ch/totem-experiment`.

[39] G. Antchev, P. Aspell, I. Atanassov, V. Avati, J. Baechler, *et al.*, "First measurement of the total proton-proton cross section at the LHC energy of $\sqrt{}$ s =7 TeV," *Europhys.Lett.* **96** (2011) 21002, `arXiv:1110.1395 [hep-ex]`.

[40] "Luminosity determination using the atlas detector," Tech. Rep. ATLAS-CONF-2010-060, CERN, Geneva, Jul, 2010.

[41] `home.web.cern.ch/about/experiments/lhcf`.

[42] **ATLAS Collaboration** Collaboration, G. Aad *et al.*, "Luminosity Determination in pp Collisions at sqrt(s)=7 TeV Using the ATLAS Detector at the LHC," *Eur.Phys.J.* **C71** (2011) 1630, `arXiv:1101.2185 [hep-ex]`.

[43] J. Kaspar, "Totem results on elastic scattering and total cross-section," in *EDS Blois 2013*. 2013. `http://indico.cern.ch/event/267509/contributions/1605297/attachments/478067/661405/jan_kaspar_eds_2013.pdf`.

[44] H.-T. Wei, R.-Y. Zhang, L. Guo, L. Han, W.-G. Ma, *et al.*, "Probe R-parity violating stop resonance at the LHeC," *JHEP* **1107** (2011) 003, `arXiv:1107.4461 [hep-ph]`.

[45] F. Bazzocchi, S. Morisi, E. Peinado, J. W. F. Valle, and A. Vicente, "Bilinear R-parity violation with flavor symmetry," *JHEP* **01** (2013) 033, `arXiv:1202.1529 [hep-ph]`.

[46] B. Bhattacherjee, J. L. Evans, M. Ibe, S. Matsumoto, and T. T. Yanagida, "Natural supersymmetrys last hope: R-parity violation via UDD operators," *Phys. Rev.* **D87** no. 11, (2013) 115002, `arXiv:1301.2336 [hep-ph]`.

[47] **CMS** Collaboration, S. Chatrchyan *et al.*, "Search for top squarks in R-parity-violating supersymmetry using three or more leptons and b-tagged jets," *Phys. Rev. Lett.* **111** no. 22, (2013) 221801, `arXiv:1306.6643 [hep-ex]`.

[48] **CMS** Collaboration, A. Cakir, "Search for R-Parity Violating Supersymmetry at the CMS Experiment," *PoS* **EPS-HEP2013** (2013) 264, `arXiv:1310.3598 [hep-ph]`.

[49] D. Chialva, R. Iengo, and J. G. Russo, "Cross sections for production of closed superstrings at high energy colliders in brane world models," *Phys.Rev.* **D71** (2005) 106009, `arXiv:hep-ph/0503125 [hep-ph]`.

[50] T. Kaluza, "On the Problem of Unity in Physics," *Sitzungsber. Preuss. Akad. Wiss. Berlin (Math. Phys.)* **1921** (1921) 966–972.

[51] O. Klein, "Quantum Theory and Five-Dimensional Theory of Relativity. (In German and English)," *Z. Phys.* **37** (1926) 895–906. [Surveys High Energ. Phys.5,241(1986)].

[52] J. Gao, M. Guzzi, J. Huston, H.-L. Lai, Z. Li, P. Nadolsky, J. Pumplin, D. Stump, and C. P. Yuan, "CT10 next-to-next-to-leading order global analysis of QCD," *Phys. Rev.* **D89** no. 3, (2014) 033009, `arXiv:1302.6246 [hep-ph]`.

[53] **ATLAS Collaboration** Collaboration, G. Aad *et al.*, "Measurement of the Inelastic Proton-Proton Cross-Section at $\sqrt{s} = 7$ TeV with the ATLAS Detector," *Nature Commun.* **2** (2011) 463, `arXiv:1104.0326 [hep-ex]`.

[54] A. Martin and T. Spearman, *Elementary Particle Theory*. North-Holland, 1970.

[55] **TOTEM** Collaboration, J. Kapar, "TOTEM Results on Elastic Scattering and Total Cross-Section," in *Proceedings, 15th conference on Elastic and Diffractive scattering (EDS Blois 2013)*. 2013. `arXiv:1310.3178 [physics.ins-det]`.

[56] P. Auger, P. Ehrenfest, R. Maze, J. Daudin, and A. F. Robley, "Extensive cosmic ray showers," *Rev. Mod. Phys.* **11** (1939) 288–291.

[57] **Pierre Auger** Collaboration, A. Aab *et al.*, "Depth of maximum of air-shower profiles at the Pierre Auger Observatory. I. Measurements at energies above $10^{17.8}$eV," *Phys. Rev.* **D90** no. 12, (2014) 122005, `arXiv:1409.4809 [astro-ph.HE]`.

[58] R. U. Abbasi *et al.*, "Study of Ultra-High Energy Cosmic Ray composition using Telescope Arrays Middle Drum detector and surface array in hybrid mode," *Astropart. Phys.* **64** (2015) 49–62, `arXiv:1408.1726 [astro-ph.HE]`.

[59] M. S. Pshirkov, P. G. Tinyakov, P. P. Kronberg, and K. J. Newton-McGee, "Deriving global structure of the Galactic Magnetic Field from Faraday Rotation Measures of extragalactic sources," *Astrophys. J.* **738** (2011) 192, `arXiv:1103.0814 [astro-ph.GA]`.

[60] R. Jansson and G. R. Farrar, "A New Model of the Galactic Magnetic Field," *Astrophys. J.* **757** (2012) 14, `arXiv:1204.3662 [astro-ph.GA]`.

[61] T. Kahniashvili, A. G. Tevzadze, S. K. Sethi, K. Pandey, and B. Ratra, "Primordial magnetic field limits from cosmological data," *Phys. Rev.* **D82** (2010) 083005, `arXiv:1009.2094 [astro-ph.CO]`.

[62] J. E. Gunn and J. P. Ostriker, "Acceleration of high-energy cosmic rays by pulsars," *Phys. Rev. Lett.* **22** (1969) 728–731.

[63] J. Pruet, S. Guiles, and G. M. Fuller, "Light element synthesis in high entropy relativistic flows associated with gamma-ray bursts," *Astrophys. J.* **580** (2002) 368–373, `arXiv:astro-ph/0205056 [astro-ph]`.

[64] M. Lemoine, "Nucleosynthesis in gamma-ray bursts outflows," *Astron. Astrophys.* **390** (2002) L31, `arXiv:astro-ph/0205093 [astro-ph]`.

[65] B. Groves, T. Heckman, and G. Kauffmann, "Emission-line Diagnostics of Low Metallicity AGN," *Mon. Not. Roy. Astron. Soc.* **371** (2006) 1559–1569, `arXiv:astro-ph/0607311 [astro-ph]`.

[66] S. Mathur and D. Fields, "Metallicity measurements in AGNs," *AIP Conf. Proc.* **1135** (2009) 209–214, `arXiv:0901.1323 [astro-ph.GA]`.

[67] K. Fang, K. Kotera, and A. V. Olinto, "Newly-born pulsars as sources of ultrahigh energy cosmic rays," *Astrophys. J.* **750** (2012) 118, `arXiv:1201.5197 [astro-ph.HE]`.

[68] **Pierre Auger** Collaboration, J. Abraham *et al.*, "Correlation of the highest-energy cosmic rays with the positions of nearby active galactic nuclei," *Astropart. Phys.* **29** (2008) 188–204, `arXiv:0712.2843 [astro-ph]`. [Erratum: Astropart. Phys.30,45(2008)].

[69] **Pierre Auger** Collaboration, A. Aab *et al.*, "Searches for Anisotropies in the Arrival Directions of the Highest Energy Cosmic Rays Detected by the Pierre Auger Observatory," *Astrophys. J.* **804** no. 1, (2015) 15, `arXiv:1411.6111 [astro-ph.HE]`.

[70] **Telescope Array** Collaboration, R. U. Abbasi *et al.*, "Indications of Intermediate-Scale Anisotropy of Cosmic Rays with Energy Greater Than 57 EeV in the Northern Sky Measured with the Surface Detector of the Telescope Array Experiment," *Astrophys. J.* **790** (2014) L21, `arXiv:1404.5890 [astro-ph.HE]`.

[71] M. M. Winn, J. Ulrichs, L. S. Peak, C. B. A. McCusker, and L. Horton, "The cosmic-ray energy spectrum above 10 17 ev," *Journal of Physics G: Nuclear Physics* **12** no. 7, (1986) 653. `http://stacks.iop.org/0305-4616/12/i=7/a=015`.

[72] **AGASA** Collaboration, H. Ohoka, S. Yoshida, M. Takeda, *et al.*, "Further development of data acquisition system of AGASA," *Nucl.Instrum.Meth.* **A385** (1997) 268–276.

[73] L. A. Anchordoqui, C. Hojvat, T. P. McCauley, T. C. Paul, S. Reucroft, *et al.*, "Full - sky search for ultrahigh-energy cosmic ray anisotropies," *Phys.Rev.* **D68** (2003) 083004, `arXiv:astro-ph/0305158 [astro-ph]`.

[74] **Pierre Auger Collaboration** Collaboration, P. Abreu *et al.*, "Search for First Harmonic Modulation in the Right Ascension Distribution of Cosmic Rays Detected at the Pierre Auger Observatory," *Astropart.Phys.* **34** (2011) 627–639, `arXiv:1103.2721 [astro-ph.HE]`.

[75] **Pierre Auger Collaboration** Collaboration, P. Abreu *et al.*, "Large scale distribution of arrival directions of cosmic rays detected above 10^{18} eV at the Pierre Auger Observatory," *Astrophys.J.Suppl.* **203** (2012) 34, `arXiv:1210.3736 [astro-ph.HE]`.

[76] L. A. Anchordoqui, H. Goldberg, and T. J. Weiler, "Update on tests of the Cen A neutron-emission model of highest energy cosmic rays," *Phys.Rev.* **D84** (2011) 067301, `arXiv:1103.0536 [astro-ph.HE]`.

[77] **Pierre Auger Collaboration** Collaboration, P. Abreu *et al.*, "Constraints on the origin of cosmic rays above 10^{18} eV from large scale anisotropy searches in data of the Pierre Auger Observatory," *Astrophys.J.* **762** (2012) L13, `arXiv:1212.3083 [astro-ph.HE]`.

[78] **Pierre Auger** Collaboration, A. Aab *et al.*, "Large Scale Distribution of Ultra High Energy Cosmic Rays Detected at the Pierre Auger Observatory With Zenith Angles up to 80," *Astrophys.J.* **802** no. 2, (2015) 111, `arXiv:1411.6953 [astro-ph.HE]`.

[79] L. Anchordoqui, T. C. Paul, S. Reucroft, and J. Swain, "Ultrahigh-energy cosmic rays: The State of the art before the Auger Observatory," *Int. J. Mod. Phys.* **A18** (2003) 2229–2366, `arXiv:hep-ph/0206072 [hep-ph]`.

[80] **Pierre Auger** Collaboration, I. Allekotte *et al.*, "The Surface Detector System of the Pierre Auger Observatory," *Nucl. Instrum. Meth.* **A586** (2008) 409–420, `arXiv:0712.2832 [astro-ph]`.

[81] **Pierre Auger** Collaboration, J. Abraham *et al.*, "The Fluorescence Detector of the Pierre Auger Observatory," *Nucl. Instrum. Meth.* **A620** (2010) 227–251, `arXiv:0907.4282 [astro-ph.IM]`.

[82] K. Greisen, "End to the cosmic ray spectrum?," *Phys. Rev. Lett.* **16** (1966) 748–750.

[83] G. T. Zatsepin and V. A. Kuzmin, "Upper limit of the spectrum of cosmic rays," *JETP Lett.* **4** (1966) 78–80. [Pisma Zh. Eksp. Teor. Fiz.4,114(1966)].

[84] **Pierre Auger** Collaboration, J. Abraham *et al.*, "Observation of the suppression of the flux of cosmic rays above 4×10^{19}eV," *Phys. Rev. Lett.* **101** (2008) 061101, `arXiv:0806.4302 [astro-ph]`.

[85] H. Tokuno *et al.*, "New air fluorescence detectors employed in the Telescope Array experiment," *Nucl. Instrum. Meth.* **A676** (2012) 54–65, `arXiv:1201.0002 [astro-ph.IM]`.

[86] **Telescope Array** Collaboration, T. Abu-Zayyad *et al.*, "The surface detector array of the Telescope Array experiment," *Nucl. Instrum. Meth.* **A689** (2013) 87–97, `arXiv:1201.4964 [astro-ph.IM]`.

[87] P. Sommers, "Cosmic ray anisotropy analysis with a full-sky observatory," *Astropart.Phys.* **14** (2001) 271–286, `arXiv:astro-ph/0004016 [astro-ph]`.

[88] **Pierre Auger Collaboration** Collaboration, O. Deligny, "Large-Scale Distribution of Arrival Directions of Cosmic Rays Detected at the Pierre Auger Observatory Above 10 PeV," *J.Phys.Conf.Ser.* **531** (2014) 012002, `arXiv:1403.6314 [astro-ph.HE]`.

[89] G. B. Thomson, "Results from the Telescope Array Experiment," *PoS* **ICHEP2010** (2010) 448, `arXiv:1010.5528 [astro-ph.HE]`.

[90] **JEM-EUSO** Collaboration, J. H. Adams, Jr. *et al.*, "The JEM-EUSO Mission: Contributions to the ICRC 2013," 2013. `arXiv:1307.7071 [astro-ph.IM]`.

[91] **OWL** Collaboration, J. F. Krizmanic, J. W. Mitchell, and R. E. Streitmatter, "Optimization of the Orbiting Wide-angle Light Collectors (OWL) Mission for Charged-Particle and Neutrino Astronomy," in *Proceedings, 33rd International Cosmic Ray Conference (ICRC2013): Rio de Janeiro, Brazil, July 2-9, 2013*, p. 1085. 2013. `arXiv:1307.3907 [astro-ph.IM]`.

[92] **Pierre Auger** Collaboration, A. Aab *et al.*, "The Pierre Auger Observatory: Contributions to the 33rd International Cosmic Ray Conference (ICRC 2013)," in *Proceedings, 33rd International Cosmic Ray Conference (ICRC2013)*. 2013. `arXiv:1307.5059 [astro-ph.HE]`. `http://lss.fnal.gov/archive/2013/conf/fermilab-conf-13-285-ad-ae-cd-td.pdf`.

[93] See the figures at `http://en.wikipedia.org/wiki/Spherical_harmonics` for useful visualizations.

[94] See e.g. Arfken, G.B. and Weber, H.J., *Mathematical Methods for Physicists*. Academic Press, 6th ed., 2005.

[95] O. E. Kalashev, B. Khrenov, P. Klimov, S. Sharakin, and S. V. Troitsky, "Global anisotropy of arrival directions of ultrahigh-energy cosmic rays: capabilities of space-based detectors," *JCAP* **0803** (2008) 003, `arXiv:0710.1382 [astro-ph]`.

[96] S. Mollerach and E. Roulet, "A New method to search for a cosmic ray dipole anisotropy," *JCAP* **0508** (2005) 004, `arXiv:astro-ph/0504630 [astro-ph]`.

[97] P. Billoir and O. Deligny, "Estimates of multipolar coefficients to search for cosmic ray anisotropies with non-uniform or partial sky coverage," *JCAP* **0802** (2008) 009, `arXiv:0710.2290 [astro-ph]`.

[98] J. Aublin and E. Parizot, "Generalized 3D-reconstruction method of a dipole anisotropy in cosmic-ray distributions," *Astron. Astrophys.* **441** (2005) 407, `arXiv:astro-ph/0504575 [astro-ph]`.

[99] J. Linsley, "Fluctuation effects on directional data," *Phys. Rev. Lett.* **34** (1975) 1530–1533.